Laser-Driven Electron Accelerators as a Broadband Radiation Source - from Infrared to X-Rays

by

Amina E. Hussein

A dissertation submitted in partial fulfillment
of the requirements for the degree of
Doctor of Philosophy
(Applied Physics)
in The University of Michigan
2019

Doctoral Committee:

Professor Karl M. Krushelnick, Co-Chair
Assistant Professor Louise Willingale, Co-Chair
Research Scientist Anatoly Maksimchuk
Research Scientist John A. Nees
Associate Professor Alexander G.R. Thomas
Professor Herbert G. Winful

Amina E. Hussein

aehuss@umich.edu

ORCID iD: 0000-0001-9676-4862

This dissertation is in honor of my grandparents,
Mohammad and Wazir Naqi, and Mahmoud Hussein and Amina Abdul-Ghaffar.

ACKNOWLEDGEMENTS

First and foremost, I would like to thank my advisors, Prof. Karl Krushelnick and Prof. Louise Willingale for their guidance throughout my studies. Karl was endlessly patient, introduced me to new and challenging topics, and gave me numerous opportunities to travel the world. Thank you to Louise for generously supporting my research, for always having an open door, and sharing valuable advice, professionally and personally (and for teaching me the "C is for cookie" song!). I am extremely grateful to Prof. Alec Thomas for encouraging me to pursue a diversity of projects and always being available for physics discussions (even when it required writing on napkins or the back of fliers). And thank you to Prof. Alexey Arefiev for teaching me to use EPOCH, encouraging my pursuit of simulation work, and creating opportunities for me to travel and present my research. I have been truly lucky to have such wonderful academic advisors who have nurtured my interests.

I have also had the great fortune to work with Research Scientists Anatoly Maksimchuk and John Nees in the HERCULES lab. Without them, much of this work would not have been possible. Tolya and John, from you both I have learned so much. I am grateful for your patience while I learned to design experiments, the kindness you expressed when I struggled, and the sense of confidence you inspired when I succeeded. Once, I told Tolya that he was the best when he helped me recover my beam under vacuum, and he replied "no, you are the best". This may have been the highlight of my graduate career. John always fostered my interests

in and outside of the lab, sending me "squirrels to chase" and posing challenging thought experiments to keep me sharp. It was a pleasure to go the lab every day when I worked with these mentors. Through them I learned discipline, endurance, and continuous curiosity.

It has also been a pleasure to work with Yong Ma, who was generous with his time and his knowledge, and is really good at using IR viewers! Thank you to Keegan Behm for showing me the ropes on HERCULES and answering my continued questions after his graduation. Hanging out with Thomas Batson was the highlight of the Trident experiment at Los Alamos National Lab. One day we will have celebratory steaks again! Peter Kordell made the office friendly and welcoming, with supportive discussions over lunch or coffee. And thank you to Paul Campbell for helping me tighten or lift things in the lab and always being down for a coffee break. Jinpu Lin, Brandon Russel and Jesus Hinojosa - your keen senses of humor and willingness to help in the lab or when I locked myself out of the office are so appreciated. I'm also very grateful for the scientists and staff at the University of Rochester Laboratory for Laser Energetics, in particular Dave Canning for his encouragement and infectious enthusiasm, and to the excellent team on experiments at the Rutherford Appleton Laboratory, particularly Dan Symes, Matthew Streeter, Brendan Kettle, Jason Cole, Stephen Dann, and Elias Gerstmayr.

I would also like to acknowledge Dr. Kirk Flippo and Dr. Sandrine Gaillard. Kirk enabled me to pursue a PhD in plasma physics and invited me to collaborate at LANL, an experience that altered the course of my graduate studies for the better. Moreover, Kirk and Sandrine were always available for advice and guidance, for which I am forever grateful. I would also like to thank Dr. Carolyn Kuranz for her guidance and inspiration. To Isabel Luce, Erin Ferraris and Raspberry Simpson,

you guys kept me sane and made me feel loved through it all. Isabel, thank you for always being only a text away. Erin, thank you for making sure I never lost my sense of adventure. Raspberry, thank you for your perspective, and baguettes and cheese.

And to my family, thank you to each and every one of you for being the inspiration and motivation to strive for success. To my dad, Esam Hussein: look I ended up following in your footsteps! You inspired me with your love of learning and teaching. To my mom, Shabana Hussein, thank you for your endless love and support, and for teaching me courage and reminding me to be patient with myself. My brother, Mahmoud Hussein, has been the greatest role model for me in pursuing my passions, going on adventures, and aligning myself with good people. My aunt, Rukhsana Bukhari kept me well fed and supported, and my uncle Shahid Naqi made sure I always on the level and having fun. And I am grateful to my grandparents, on both sides, who inspired me with their legacies.

Thank you to Wylie Stroberg, who was next to me the entire way. Thank you for your love, understanding, enthusiasm and grilled cheeses. I'm so grateful to have shared this time with you and can't wait for what comes next.

And to Roz, who kept me company while I wrote. She would have helped write the whole thing, but she fell asleep.

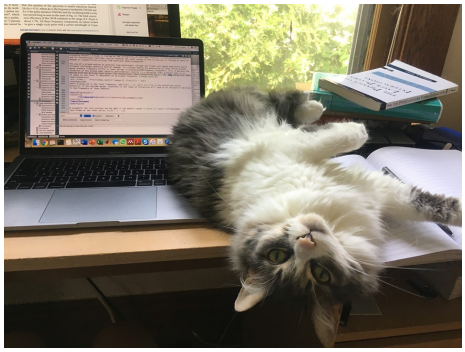

TABLE OF CONTENTS

LIST OF FIGURES

Figure

LIST OF TABLES

Table

ABSTRACT

This dissertation explores the acceleration of electrons and associated production of radiation through the interaction of intense laser pulses with underdense plasma. For femtosecond duration pulses, where the pulse duration is shorter than the plasma period, the dominant electron acceleration mechanism is Laser Wakefield Acceleration (LWFA), wherein electrons gain energy by "surfing" electron plasma waves. For high-intensity picosecond pulses the transverse laser field becomes the dominant acceleration mechanism, giving electrons longitudinal momentum *via* the v × B force. This is known as Direct Laser Acceleration (DLA).

Experiments on the OMEGA EP laser facility demonstrated the existence of an optimal density for acceleration of electrons up to 600 MeV *via* DLA using a high-energy, picosecond duration pulse. Two-dimensional particle-in-cell (PIC) simulations conducted using the EPOCH code confirm DLA as the dominant acceleration mechanism and elucidate that dynamic role of quasi-static channel fields on electron energy enhancement. Electron beams generated by this scheme could be used to obtain brilliant, spatially coherent X-rays with the capability to be accurately synchronized to short pulse laser-initiated events.

During LWFA, the formation of a plasma bubble results in a co-moving refractive index gradient that produces time dependent frequency shifts in the driving laser pulse, generating wavelengths extending into the mid-infrared. High-resolution spectral measurements of this radiation and its dependence on laser and plasma pa-

rameters were investigated using the HERCULES laser system. The use of a tailored plasma density was shown to produce wavelengths extending to 2.5 μm, and containing up to 15 mJ of energy. Further experimental studies on HERCULES yielded the first measurements of backward Stimulated Raman Scattering (BSRS) in the strongly coupled regime of LWFA, which were found to be highly modulated and broadened in cases where electrons were accelerated. Simulations and experiments indicate that measurement of BSRS may be used as a diagnostic of bubble formation and trapped electron charge within the bubble. Finally, X-ray imaging results of an Al-Si alloy obtained using betatron radiation from a LWFA indicate that these sources can be competitive with conventional synchrotron radiation.

CHAPTER I

Introduction

1.1 Historical perspective

In the early 1920s, Ernest Rutherford desired a source of multi MeV particles for continuing his research on atomic structure. However, at this time, voltages required for sufficient particle acceleration had not yet been achieved. The prediction of quantum tunneling by George Gamow at the same time as Ronald Gurney and Edward Condon, whereby an electron can penetrate a potential barrier, led to the development of the first particle accelerator by John Cockcroft and Ernest Walton in 1932 [1]. Their device, known as the *Cockcroft-Walton generator*, accelerated protons from ionized hydrogen through a steady electric field in an accelerating column to produce the first artificially accelerated high energy particles. The realization of this device led to the first controlled splitting of the atom, for which they were awarded the Nobel prize in 1951. However, their device was limited by the breakdown of air, which occurs at energy gradients over a few MeV/meter. Thus, enhanced particle acceleration by this device was limited.

An alternative approach by Gustav Ising in 1924, based on time-varying electric fields, led to the development of the linear accelerator [2, 3]. Ising proposed a method of particle acceleration that employed alternating radiofrequency (RF) fields. The design consisted of a linear series of conducting tubes connected to an RF generator. In this configuration, following Faraday's law, the periodic rise and fall of the magnetic field concentrated at the wall of each tube induces an electric field along the axis of the cavity that is synchronized with the motion of an electron. A time-varying field is the basis of modern particle accelerators.

The further development of acceleration mechanisms capable of producing higher energy beams required focusing in the transverse and longitudinal directions. This issue was addressed by McMillan and Veksler independently in 1944 and led to the invention of the *synchrotron*. The major advancement of the synchrotron was bunching together particles at variable energies by injecting them at specific phases in the RF cycle.

By 1952, 3 GeV protons were accelerated using the Cosmotron synchrotron at Brookhaven National Laboratory. However, particle acceleration with this technology was still limited by focusing in the transverse plane. In the 1950s, particle accelerators were again revolutionized with the development of alternating-gradient focusing, which reduced accelerator size. This advancement enabled CERN to achieve acceleration of 25 GeV/c [3].

Advances in accelerator technology has led to the generation of high energy particle beams and associated X-ray radiation, culminating in the acceleration of electrons and positrons up to 50 GeV using the Stanford Linear Accelerator (SLAC). SLAC, an RF linear accelerator, is also capable of producing X-rays with ultra-short (femtosecond) pulse duration with energies on the order of (0.25 - 9.5) keV. These particle

Figure 1.1: Aerial view of the Stanford Linear Accelerator, spanning 3.2 km.

beams and X-rays with ultra-short duration can be used for a variety of applications in fundamental science and industry, including probing electron motion on the atomic scale, elucidating the behavior of materials under extreme conditions, and exploring the dynamics of physiological processes.

However, conventional accelerators suffer several limitations in their further advancement. Of significant note is the limited accelerating gradients in an RF cavity due to electric breakdown of the cavity. Additionally, despite advances in minimizing the size of conventional accelerators, these devices remain massive and expensive; electron acceleration up to 50 GeV at SLAC (Fig. 1.1) is achieved over a distance of 3.2 km, and cost billions of dollars in construction. Achieving higher energy particle beams would require even larger accelerators, which becomes prohibitively expensive. Therefore, a novel acceleration mechanism with reduced in size and construction costs is required.

Modern laser technology and the realization of high-intensity, ultra-short pulse laser systems using Chirped Pulse Amplification [4], the technique for which Donna Strickland and Gerard Mourou were awarded the Nobel Prize in 2018, has led to the development of novel states of matter and accelerating schemes. The focusing of short-pulse lasers with petawatt peak power can be used to generate intensities reaching 10^{22} W/cm^2 [5], and the force generated by these pulses in a plasma medium can produce acceleration gradients three orders of magnitude greater than achieved

in conventional accelerators. These new-generation particle accelerators, known as *laser-driven plasma accelerators* or *laser plasma accelerators*, were first proposed by Tajima and Dawson in 1979 [6] and their development and optimization has since become a world-wide research effort.

The acceleration gradients in LPA can be in excess of 100 GV/m [6, 7], enabling the continuous acceleration of plasma electrons to GeV energies over a few centimeters of plasmas[6, 8, 9, 10], where comparable acceleration would require 10s of meters in a conventional linear accelerator. Additionally, by virtue of the ionized accelerating medium, laser-based accelerators do not fall prey to the breakdown limit of conventional accelerators. Thus, advanced laser systems provide a unique alternative for the acceleration of particles to high energies and the generation of bright, ultra-short radiation bursts, at a fraction of the cost of conventional facilities and with significantly smaller spatial requirements.

1.2 Laser plasma acceleration

As an intense laser pulse travels through underdense plasma the ponderomotive pressure of the beam will expel electrons along its path. The displacement of plasma electrons results in regions of positive and negative charge, creating electrostatic plasma waves. These plasma waves, with phase velocities approaching the speed of light, can trap and accelerate electrons. For sustained laser-plasma interactions, achieved using longer duration pulses, the laser can expel all of the electrons along its path, producing a plasma channel devoid of electrons and with strong electrostatic fields. Electrons that become trapped in this channel can also become accelerated.

Laser-wakefield acceleration (LWFA) is a method for producing high-energy electron beams using the accelerating field structure produced in the wake of a high-

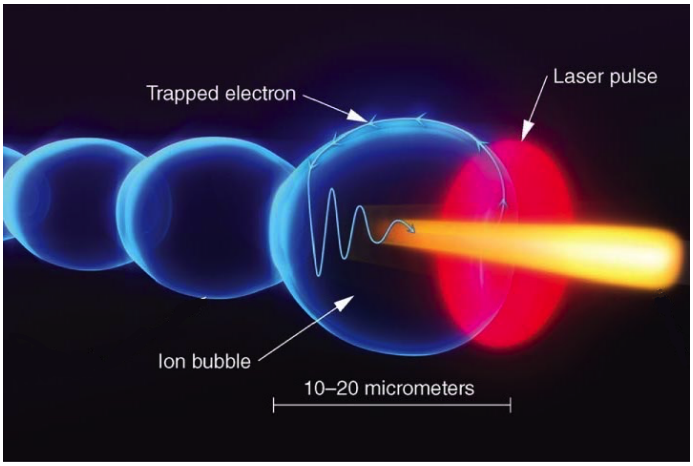

Figure 1.2: Laser wakefield acceleration (LWFA) produces plasma waves with relativistic velocities that can trap and accelerate electrons to many GeV energies. Figure reproduced with permission from Ref. [11].

power, ultrashort pulsed laser propagating through low density plasma. During wakefield acceleration, an electron bunch "surfs" on the electric wave generated by the light pressure of an intense laser pulse [6]. A schematic of this process is shown in Figure 1.2. This wave induces a strong longitudinal electric field that remains in phase with the laser driver, enabling relativistic electrons to gain significant energy from the accelerating field over long distances.

The demonstration of high-quality monoenergetic electron beams *via* LWFA was achieved by three groups simultaneously in 2004 [12, 13, 14]. Electrons beams with GeV energies were first demonstrated by Leemans et al. in 2006 [8]. The current record for electron acceleration *via* LWFA is 7.8 GeV, achieved using relativistcally guided laser pulses through a capillary discharge waveguide[10]. Additionally, in the highly nonlinear regime of LWFA, electrons undergo betatron oscillations in the strong focusing fields of the wakefield, emitting a bright source of X-rays with a source size as small as one micrometer. [15, 16, 17]. Betatron X-ray beams produced *via* LWFA have been shown to produce stable, bright X-ray beams capable of high-resolution tomographic imaging [16, 18, 19, 20, 21, 22]. The resultant beams have

a low divergence (on the order of a few milliradians [23]) and ultrashort duration (less than 100 fs [24]), making them useful for a large range of applications across engineering, medicine, homeland security and science [16, 19, 20, 17, 21, 22].

Using picosecond duration pulses, electron acceleration can occur in the Self-Modulated regime of LWFA (SM-LWFA). This occurs whem the driving laser undergoes Stimulated Raman Scattering (SRS), or the related self-modulated instability, and becomes modulated at the plasma frequency (Fig. 1.3) [25, 26, 27]. SM-LWFA is associated with large-amplitude plasma waves in the forward direction that trap and accelerate electrons to MeV energies [28, 29, 30, 31]. Electron motion during SM-LWFA has been showed to hard X-ray sources [27, 32].

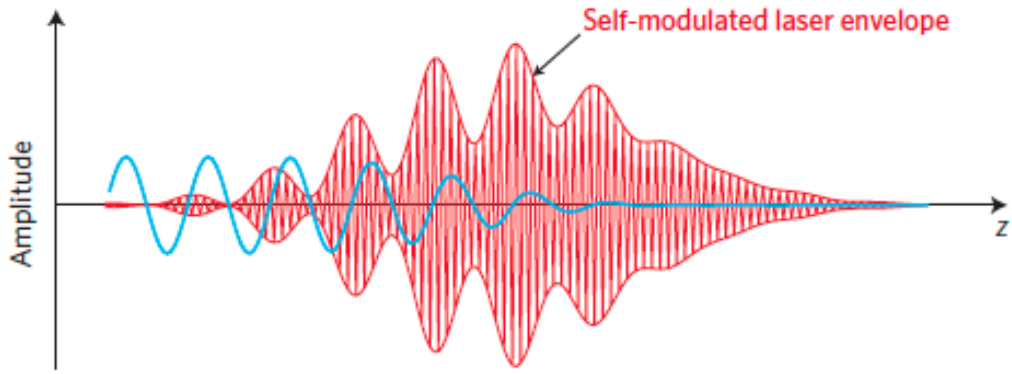

Figure 1.3: Self-modulation of a long laser pulse at the plasma frequency. The laser field is shown in red and the plasma wakefield is shown in blue. Figure reproduced with permission from Ref. [33].

SM-LWFA occurs in the regime where the pulse length is long compared to the plasma wavelength ($L > \lambda_p$), and the laser power exceeds the critical power for relativistic self-focusing ($P > P_c$), but is in the weakly relativistic regime ($a_0 \leq 1$). This is typically achieved by operating at a relatively high density. In general, it is easier to achieve the conditions necessary for SM-LWFA than LWFA, since matching conditions of pulse duration to laser wavelength or density tailoring are not required. However, SM-LWFA suffers disadvantages due to the higher plasma

density required, which reduces maximum achievable electron energies due to electron dephasing from the plasma wakefield, as well as the production of electron beams with broad energy spread produced due to continual electron trapping along the laser propagation distance. Given that SM-LWFA is driven by an instability, it is also subject to large fluctuations in beam quality.

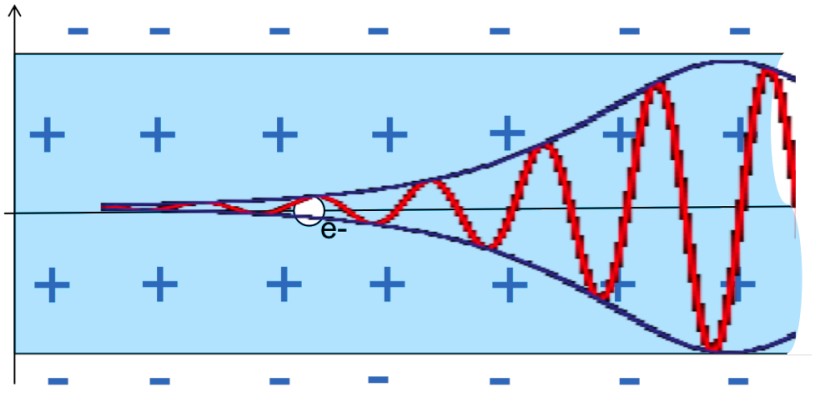

Figure 1.4: Irradiation of an underdense plasma with a picosecond, high intensity laser pulse will ponderomotively expel electrons in the focal volume of the laser, creating a plasma channel. Electrons injected into this channel can then be accelerated by DLA. The laser electric field (red) and pulse envelope (blue) are shown.

As the intensity of picosecond laser pulses is increased the Direct Laser Acceleration (DLA) mechanism becomes dominant. A high-intensity, picosecond duration laser pulse will ponderomotively expel nearly all of the electrons within its focal volume in the plasma, creating a positively charged channel (Fig. 1.4). This channel evolves on the ion timescale and is therefore considered quasi-static relative to the timescale of electron motion. Electrons are accelerated directly by the laser field and gain forward momentum due to the $v \times B$ force in the Lorentz force equation [34, 35, 36]. DLA can be used to produce high charge electron beams [29, 37, 38]) and may also produce higher amplitude betatron oscillations than achieved in the wakefield regime, enabling X-ray sources with much higher energies [39].

The generation of energetic electrons is an essential feature of laser-plasma interaction, thus its study is of fundmental interest in diagnosing and understanding plasma phenomena. Potential uses of high-charge, high-average energy electron beams include positron production through the interaction of energetic electrons with a high-intensity laser pulse [40, 41], experimental verification of the two-photon Breit-Wheeler process [42], and the generation of bright, directional X-ray beams, which can be used for high-resolution X-ray probing [16, 19, 20, 22, 43]. Laser-generated X-ray sources with ultrashort duration have the unique capability to be accurately synchronized to short pulse laser-initiated events, and could be used to probe the dynamics of dense plasmas relevant to inertial confinement fusion [27] and for characterization of high energy density physics experiments [44, 21]. These beams could also be used to produce novel radiation sources, including MeV level X-rays through inverse-Compton scattering [45], and infrared radiation and single-cycle pulses through self-phase modulation [46, 47].

1.3 Dissertation outline

This dissertation presents experimental measurements of electron acceleration and radiation production from laser-driven electron accelerators. High-intensity picosecond and femtosecond laser systems were used to generate high energy electron beams by Direct Laser Acceleration and Laser Wakefield Acceleration, respectively. This work demonstrates the utility of picosecond duration lasers for electron acceleration, as we all as the potential of these systems for producing hard X-ray sources which could be used for advanced radiography of dense materials. Studies using femtosecond duration pulses demonstrate the generation broadband radiation sources in the infrared regime, role of plasma instabilities on electron trapping during LWFA,

and the application of betatron X-ray sources for advanced imaging of complex microstructures.

A theoretical background on the interaction of intense laser pulses with underdense plasma is given in Chapter II. A description of the high intensity laser systems used in this work, primary diagnostics and experimental methods used in this dissertation is given in Chapter III. Chapter IV focuses on the acceleration of electrons to many hundreds of MeV *via* DLA using high-energy picosecond duration lasers. In Chapter V, the generation of optical radiation with wavelengths extending into the mid infrared range during LWFA acceleration using tailored-density plasma targets is demonstrated. Chapter VI investigates the role of backward Stimulated Raman Scattering on electron trapping during LWFA. Chapter VII presents high-resolution X-ray imaging of complex microstructures in metallic alloys using betatron X-rays. Finally, conclusions and discussions on future work are given in Chapter VIII.

CHAPTER II

Theoretical background

During laser-matter interaction, plasma electrons perturbed by the laser pulse will oscillate with a characteristic frequency known as the electron plasma frequency:

$$\omega_{pe} = \sqrt{\frac{n_e e^2}{m_e \epsilon_0}} \tag{2.1}$$

where n_e is the plasma density, e is the electron charge, m_e is the electron mass and ϵ_0 is the electric constant.

In underdense plasma, $\omega_{pe} < \omega_L$, where ω_L is the laser frequency, the laser field can propagate into the plasma. The critical density, $n_c = \epsilon_0 m_e \omega_0^2 / e^2$, is defined as the density at which $\omega_{pe} = \omega_L$, resulting in reflection of the laser field. The laser-plasma interactions discussed in this dissertation are generated through the interaction of an intense laser pulses with underdense plasma.

For laser intensities exceeding 10^{18} W/cm^2 , defined as *relativistic intensities*, plasma electrons begin to oscillate at velocities approaching the speed of light, resulting in a nonlinear response to the laser field due to an effective boost of the

electron mass by the relativistic Lorentz factor, $\gamma = \sqrt{1 - v^2/c^2}$, where v is the electron velocity and c is the speed of light. An important parameter in the discussion of high-intensity laser-matter interactions is the normalized vector potential, a_0, which is defined as:

$$a_0 = \frac{p_0}{m_0 c} = \frac{eE}{m_0 \omega c} = 0.85 \times 10^{-9} \lambda[\mu m](I[W/cm^2])^{1/2} \tag{2.2}$$

in which p_0 is the electron quiver momentum, I is the laser intensity in W/cm^2 and λ is the laser wavelength in μm. For $a_0 \geq 1$, occurring at intensities $\geq 1 \times 10^{18}$ W/cm^2 for $\lambda = 1\mu$m, the electron mass, m_e, begins to increase above the electron rest mass, m_0 (0.511 MeV). When $a_0 \gg 1$, the electron motion is relativistic, and the interaction becomes nonlinear. At these intensities, the plasma frequency, ω_{pe}, is modified by relativistic boosting of the electron mass to γm_e.

The intensity of the laser pulse, I, is given by the magnitude of the Poynting vector, S, averaged over the laser period:

$$I = \langle |S| \rangle = \frac{1}{\mu_0} \langle |E \times B| \rangle = \frac{\epsilon_0 c}{2} E_0^2 \tag{2.3}$$

where μ_0 is the vacuum permeability constant. The laser intensity is related to the normalized vector potential by:

$$I\lambda^2 = a_0^2 \times 1.39 \times 10^{18} W/cm^2 \mu m^2 \tag{2.4}$$

2.1 Single particle motion in an electromagnetic field

The equation of motion of an electron subject to a laser field is given by the Lorentz equation:

$$\bar{F} = \frac{d(\gamma \bar{p})}{dt} = e(\bar{E} + \frac{\bar{v}}{c} \times \bar{B}) \tag{2.5}$$

where $\bar{E}$ and $\bar{B}$ are the electric and magnetic fields, $\bar{p} = m_0 \bar{v}$ is the electron momentum, $\bar{v}$ is the electron velocity.

Defining a vector potential, $\bar{A}(x)$, such that

$$\bar{B}(x) = \nabla \times \bar{A}(x) \tag{2.6}$$

where $\nabla \cdot \bar{B} = 0$, the electric and magnetic fields are related to this vetor potential by:

$$\bar{E} = -\nabla\Phi - \delta\bar{A}/\delta(ct) \tag{2.7}$$

$$\bar{B} = \nabla \times \bar{A} \tag{2.8}$$

In two-dimensions, (x, y), where the x-axis is along the direction of plane wave propagation, the propagation of a plane wave can be described using the normalized vector potential,

$$\bar{a}(x,t) = a(\xi) \times [\bar{e}_x \cos\theta + \bar{e}_y \sin\theta] \tag{2.9}$$

where $\bar{e_x}$ and $\bar{e_y}$ denote a unit vector in the y-direction and ξ is a dimensionless phase variable, defined by:

$$\xi \equiv 2\pi(ct - x)/\lambda \tag{2.10}$$

where λ is the laser wavelength and t is the time in the laboratory frame.

The electric and magnetic fields of the wave in terms of the normalized, non-dimensional vector potential are given by:

$$\bar{E} = -\frac{m_e c}{|e|}\frac{\partial\bar{a}}{\partial t} \tag{2.11}$$

$$\bar{B} = \frac{m_e c^2}{|e|}\nabla \times \bar{a} \tag{2.12}$$

In the case where a plane wave propagates along the x-axis, with the electric field in the y-axis and the magnetic field in the z-axis, the equation of motion in terms of the normalized momentum, $\bar{p} = \bar{p}/m_e c$, is:

$$\frac{d}{dt}\left(\frac{\bar{p}}{m_e c}\right) = \frac{-|e|}{m_e c}\left[\bar{E} + \frac{\bar{p}}{\gamma m_e c} \times \bar{B}\right] \tag{2.13}$$

which yields the following equations of motion in the (x, y)-plane for an electron initially at rest:

$$\frac{d}{dt}\left(\frac{p_x}{m_e c}\right) = -\frac{|e|E_y}{m_e c} \tag{2.14}$$

$$\frac{d}{dt}\left(\frac{p_y}{m_e c}\right) = -\frac{|e|B}{\gamma m_e c}\frac{p_x}{m_e c} \tag{2.15}$$

where the velocities in terms of the non-dimensional momentum are:

$$\frac{dx}{dt} = \frac{c}{\gamma}\frac{p_x}{m_e c} \tag{2.16}$$

$$\frac{dy}{dt} = \frac{c}{\gamma}\frac{p_y}{m_e c} \tag{2.17}$$

and the relativistic factor depends on the longitudinal and transverse momentum, p_x and p_y by:

$$\gamma = \sqrt{1 + (p_x/m_e c)^2 + (p_y/m_e c)^2} \tag{2.18}$$

At sub-relativistic intensities, the electron velocity is much lower than the speed of light, and thus the effect of the magnetic field in the Lorentz force equation (Eq. 2.5) is negligible. Electron motion in this limit is linear and characterized by oscillation at the laser frequency in a straight line parallel to the polarization of the laser field.

In the relativistic limit ($a_0 \gg 1$), the $v \times B$ term in the Lorentz force equation becomes proportional to the contribution from E, resulting in longitudinal motion

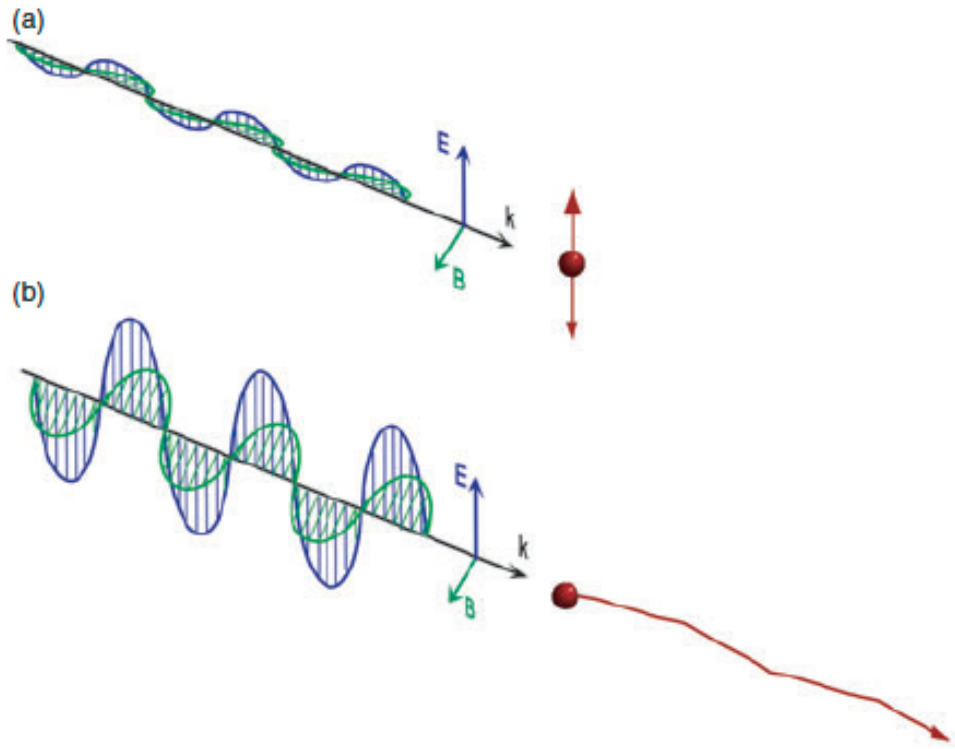

Figure 2.1: Electron motion in the linear and relativistic regimes. **a)** At sub-relativistic intensities, electrons oscillate in the direction of the laser field and do not gain longitudinal momentum. **b)** At relativistic intensities, electrons gain a drift velocity in the longitudinal direction under the combined action of the electric and magnetic field in the Lorentz force equation. Figure reproduced with permission from Ref. [48]

of electrons due to a drift velocity in the direction of the laser propagation. This will produce a figure eight motion of electrons in the plane of the laser polarization and laser propagation. At very high intensities, $a_0^2 >> 1$, drift in the longitudinal direction begins to dominate transverse motion, giving the electron longitudinal momentum. An illustration of electron motion in linear and relativistic regimes is given in Figure 2.1.

2.2 Laser propagation in an underdense plasma

In laser-plasma experiments, an intense laser beam focusing into a plasma has spatial and temporal intensity gradients. During laser propagation in a plasma,

electrons will be expelled from regions of high intensity to regions of lower intensity, creating a density perturbation. This force is known as the *ponderomotive force*, and is proportional to the gradient of the pressure due to the time-averaged quiver velocity of the electron; it can be considered to be analogous to thermal pressure.

The ponderomotive force during LWFA can be understood by considering an electron subject to an intense laser field that will cause it to move to a region of low intensity during the first half of the laser period. Once this electron resides in a region of lower intensity it will be subject to a weaker electric return force, and will not move back to its original position during the second half of the laser period. This displacement imbalance results in a net force and energy gain of electrons over several oscillations of the laser field, producing an electron depletion in regions of high intensity. In response to the expulsion of plasma electrons, electrostatic restoring forces cause the plasma electrons to oscillate at ω_{pe}. Through this process, laser energy can be converted into an electrostatic plasma wave (EPW). The growth rate of these plasma waves is dependent on the laser pulse duration compared to the oscillation frequency of the plasma.

Assuming no electrostatic fields, the relativistic pondermotive force on a single electron in vacuum is given by:

$$F_p = -\left\langle \frac{c}{\gamma}\frac{\nabla a^2}{2} \right\rangle = -mc^2/nabla(\gamma - 1) \tag{2.19}$$

which is obtained from the time average, denoted $\langle\rangle$ of slowly varying components in the electron equation of motion (Eq. 2.13). The associated ponderomotive potential, which dictates the energy gain of an electron under the field of the laser, is given by:

$$U_p = m_e c^2(\langle\gamma\rangle - 1) \tag{2.20}$$

where $\langle\gamma\rangle = (1 + \langle a^2\rangle)^{1/2}$, where $\langle a^2\rangle = a_0^2/2$ for linearly polarized light.

For sub-picosecond laser pulses, the ion response time is longer than the laser pulse duration, and therefore ions remain stationary during the interaction. However, for picosecond duration laser pulses, where the laser pulse duration exceeds the ion response time, ions will also begin to move from the cavity and electron acceleration in the direction of laser propagation has been found to be uncorrelated with plasma wave production [37].

2.3 Nonlinear phenomena and instabilities

The charge separation due to the laser fields in a plasma also support collective phenomena, such as plasma waves, which are associated with strong electrostatic fields. At relativistic intensities, the increase in the electron mass alters the plasma frequency to $\omega_{pe}\gamma^{1/2}$. At these intensities, the refractive index seen by the laser is:

$$\eta \simeq 1 - \frac{\omega_{pe}}{2\omega_0} \tag{2.21}$$

where ω_{pe} is the plasma frequency, ω_0 is the laser frequency.

The group (v_g) and phase (v_ϕ) velocities of the laser pulse propagating through plasma are given by:

$$v_g = \frac{\partial \omega_0}{\partial k_L} = \eta c \tag{2.22}$$

$$v_\phi = \frac{\omega_0}{k_L} = c/\eta \tag{2.23}$$

In underdense plasma, where $n_e < n_c$, the index of refraction, $\eta < 1$, therefore $v_g < c$ and $v_\phi > c$.

2.3.1 Self-focusing

At the point of maximum intensity of the laser beam, typically on axis for a Gaussian laser pulse, the electron quiver motion peaks, resulting in a maximum

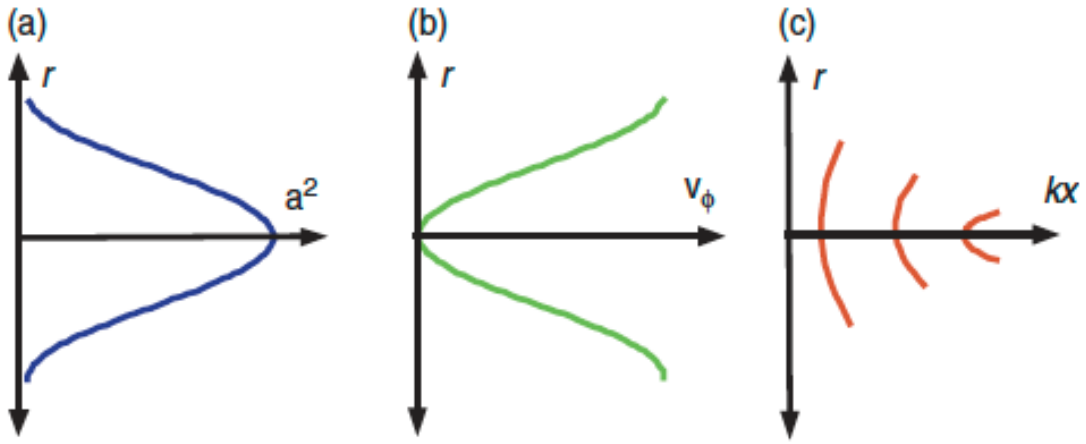

Figure 2.2: **a)** The peak laser intensity (a^2) for a Gaussian laser pulse will occur on axis. **b)** The phase velocity, v_ϕ, is inversely proportional to the laser intensity due to the refractive index change. **c)** Curvature of the wavefront, resulting in focusing. Figure reproduced with permission from Ref [48].

index of refraction at the same place and causing curving of the laser wavefront (Fig. 2.2). This process is known as *relativistic self-focusing*, and causes location variation in the phase velocity, $v_\phi = c/\eta$, which will modify the spatial and temporal profile of the laser intensity. The critical power is defined as the power at which relativistic self-focusing is balanced with diffraction of the laser pulse in the plasma, and is dependent on the incident laser frequency, ω, and the plasma frequency, ω_{pe} by [49]:

$$P_c[GW] = 2c\left(\frac{mc^2}{e^2}\right)\left(\frac{\omega}{\omega_{pe}}\right) \tag{2.24}$$

Temporal variations in the Lorentz factor, γ, can also result in time varying modifications to the index of refraction, known as *self-phase modulation* (SPM). SPM is associated with modulation and broadening of the spectrum of transmitted laser light. At regions of high intensity, the refractive index increases, resulting in self-focusing and self-phase modulation [48].

2.3.2 Filamentation

As plasma density increases, the pulse will not propagate through the entire plasma due to the filamentation instability and the transverse break-up of the laser pulse. Filamentation can also occur for laser powers greatly exceeding P_c, where propagation dynamics are dominated by the formation of higher-order transverse modes [50]. Therefore, the filamentation instability can be triggered by both ponderomotive and relativistic effects, and reduces the efficiency of coupling of laser energy to electrons by reducing the intensity of a driving laser pulse.

2.3.3 Photon acceleration and deceleration

Plasma waves have been demonstrated to produce an an upshift (or downshift) of the driving laser frequency due to a time-varying refractive index, resulting in photon acceleration (or deceleration) [51, 47, 52]. In order of this to occur, the laser frequency needs to exceed the plasma frequency, such that the spatial and temporal scales of plasma perturbations are greater than the wavelength and period of laser photons [53, 52].

Laser light interacting with a co-moving increase in plasma density will result in blueshifting of the laser spectrum (decrease in wavelength). Such increases in plasma density are caused by an ionization front associated with pulse propagation, and thus this phenomena is known as *ionization blueshift* [54, 53]. During LWFA, the transfer of laser energy to the plasma will result in red-shifting of the driving laser pulse (photon deceleration). However, plasma waves formed during LWFA will result in asymmetric shifting the laser pulses, due to the existence of regions of increasing and decreasing plasma density. Therefore, depending on the position of photons within the wakefield bubble they will experience either photon acceleration (blue-shifting)

or deceleration (red-shifting). This results in non-linear dispersion of the laser pulse, and the measurement of this spectrum has been suggested as a diagnostic of wakefield dynamics [55].

As an illustration of this process, a plasma wave can be assumed to have a sinusoidal density perturbation, $\delta n = -\delta n_0 \sin(k_p \zeta)$, in the moving frame where $\zeta = z - ct$. Considering a witness laser pulse centered at $\zeta = 0$ within the plasma wave and with a length $L \ll \lambda_p$ will experience higher plasma density at the front of the pulse ($\zeta = L/2$) than it will at the rear of the pulse ($\zeta = -L/2$). Given that the phase velocity of the laser pulse depends on the plasma density, the laser pulse will experience different phase velocities, such that $v_{ph}(L/2) < v_{ph}(-L/2)$, resulting in phase peaks at the back of the pulse moving faster than those at the front [7]. In this way, the wavelength of the laser pulse will decrease, and the pulse frequency will increase. Measurements of even small frequency shifts can be used to diagnose wake formation and dynamics (See Ref. [7] and references within).

2.3.4 Stimulated Raman Scattering

Stimulated Raman Scattering (SRS) is an instability occurring at densities much less than $n_c/4$ that involves the coupling of a large amplitude of a light wave ω_0 into a scattered wave, ω_s and an electron plasma wave ω_e. SRS satisfies the wave matching condition:

$$\omega_0 = \omega_s + \omega_e \tag{2.25}$$

$$k_0 = k_s + k_e \tag{2.26}$$

Both Stokes ($\omega_0 - \omega_{pe}, k_0 - k_e$) and anti-Stokes ($\omega_0 + \omega_{pe}, k_0 + k_e$) scattered light waves can be produced. The growth rate of plasma waves is $\omega_e = \omega_{pe} + i\gamma$, where γ is the

growth rate of the Raman instability. The Raman instability is seeded by density fluctuations. At densities approaching $n_c/4$, the group velocity of the scattered wave will decrease to zero [49].

Forward Stimulated Raman Scattering

Forward scattered Raman waves will typically travel nearly parallel to the pump wave, producing plasma waves with a phase velocity $v_p \simeq c$. Therefore, the plasma waves produced through SRS can accelerate electrons to high energy, and serves the basis for SMLWA.

Backward Stimulated Raman Scattering

Backward Simulated Raman Scattering (BSRS) typically has the fastest growth rate of the SRS instabilities. BSRS is characterized by the formation of a backward traveling scattered wave, $(\omega_0 - \omega_{pe}, k_0 - k_e)$, where $\omega_e \simeq \omega_{pe}$ and $k_e \simeq 2k_0$. At low laser intensities, measurements of backward scattered light can be used as a diagnostic of the plasma density through $\omega_0 - \omega_{pe}$.

For high amplitude BSRS waves significant plasma heating can occur by the trapping and acceleration of background plasma electrons. Plasma waves associated with BSRS will have a phase velocity $v_p = \omega_e/k_e = \omega_{pe}/2k_0$, and for a phase velocity much slower than the speed of light, this plasma wave will trap background thermal electrons and accelerate them to high energies, as has been experimentally observed (Ref. [7] and references therein).

The standard temporal growth rate of SRS can be considered in two regimes. In the weakly coupled regime, where $a_0^2 \ll \omega_{pe}/\omega_0 \ll 1$, the growth rate is given by:

$$\gamma_{SRS} = \frac{a_0}{2}\sqrt{\omega_{pe}\omega_0} \tag{2.27}$$

As the intensity of the pump laser increases, the system is said to be in the strongly

coupled regime. In this regime, the growth rate of the SRS instability becomes large, such that $\omega \simeq \gamma \gg \omega_{pe}$ and is associated with pronounced spectra broadening [56]. Extreme broadening of backscattered spectra may indicate scattering from many unstable plasma modes in the strongly coupled regime due to loss of coherence of plasma waves during wavebreaking [57, 56, 58]. Broadening may also be due to spatiotemporal localization (bursting) of the Raman scattered light within the laser pulse from a rapid saturation of the SRS instability [58, 59].

2.4 Laser-driven electron acceleration

In laser-plasma physics, the mechanisms for energetic electron production are highly dependent on laser pulse duration. For femtosecond (fs) duration laser pulses, where the pulse duration is comparable to the plasma period ($\tau_L \simeq 1/\omega_{pe}$ where $\omega_{pe} = n_e e^2/\epsilon_0 m_e$ is the plasma frequency) the dominant acceleration mechanism is Laser Wakefield Acceleration (LWFA). Electrons that become trapped in the plasma waves during LWFA will be subject to a longitudinal force, accelerating them to relativistic velocities.

When the laser pulse duration is much greater than the plasma period, as achieved with picosecond (ps) duration pulses, the laser will undergo Stimulated Raman Scattering, or the related self-modulated instability, and the laser pulse amplitude becomes modulated at the plasma frequency [25, 26, 27]. Electrons in this regime are accelerated in multiple "buckets" by plasma waves with spacings at the plasma frequency, as well as longitudinal momentum from the laser field where it overlaps with energetic electrons through the $v \times B$ force.

As the intensity of picosecond laser pulses is increased a third acceleration mechanism known as Direct Laser Acceleration (DLA) becomes dominant. At these ultra-

relativistic intensities, the laser pulse will expel nearly all of the electrons within the focal volume by ponderomotive pressure, creating charge separation and ultimately a quasi-static channel. Electrons that become trapped in the ion channel will gain longitudinal momentum from the laser field through the $v \times B$ force in the Lorentz force equation [35, 36, 34].

2.4.1 Limits on energy gain

An electron accelerated in the laser-propagation axis, by a linear electrostatic plasma wave will experience an increase in velocity approaching the speed of light. If the phase velocity of the plasma wave is constant with $v_{ph} < c$, electrons will eventually outrun the plasma wave and move into a decelerating phase region of the plasma wave. The effect of the electron outrunning the accelerating region of the plasma wave will limit its energy gain, and this limiting effect is commonly referred to as *electron dephasing*.

The electron dephasing length, denoted L_d, is defined as the length the electron travels before it slips by one-half of a period with respect to the plasma wave. For a relativistic electron with $v_z \simeq c$, the dephasing length in linear plasma waves is:

$$L_d = (1 - v_{ph}/c)\, L_d = \lambda_p/2 \tag{2.28}$$

The maximum energy gain of an electron after it has traveled one dephasing length is:

$$W_{max} \simeq eE_{max}L_d \simeq 2\pi\gamma^2(E_{max}/E_0)m_ec^2 \tag{2.29}$$

in the case where the maximum amplitude of the plasma wave E_{max} is less than the laser electric field, E_0.

2.4.2 Laser-driven plasma waves

The velocity of a laser-driven plasma wave is important for determining the maximum amplitude of the plasma wave and the maximum energy gain. The phase velocity of a plasma wave can be considered to be equal to the group velocity of the laser when evolution of the drive beam is neglected.

In the linear regime, the group velocity of a laser pulse in plasma is determined from the 1D dispersion relationship, $\omega_0^2 = c^2k^2 + \omega_{pe}^2$, from which $v_g = c(1 - \omega_{pe}^2/\omega_0^2)^{1/2}$ and $\gamma = \omega_0/\omega_{pe}$ [7].

The group velocity of the laser is reduced in the 3D case by diffraction. The evolution of a Gaussian laser pulse will result in a deflection of photons with respect to the laser propagation axis at a diffraction angle of $\theta_d = r_0/Z_R$, where r_0 is the focal spot size and $Z_R = \pi\omega_0^2/2$ is the Rayleigh length. Therefore, the group velocity will be reduced by this deflection.

2.4.3 Laser Wakefield Acceleration

Wakefield generation is most efficient when the pulse length is on the order of the plasma period, generating large amplitude plasma waves (wakefields) with phase velocities approaching the group velocity of the driving laser pulse. For a Gaussian laser profile, the maximum wakefield amplitude is achieved when $L_{rms} \simeq \lambda_p/(2\pi)$. The precise length scale for maximized plasma waves depends on the regime of acceleration (linear or nonlinear), and the shape of the driving pulse.

The wakefield amplitude driven by a linearly polarized square pulse is maximized when the pulse length, L, is approximately equal to the plasma wavelength, $\lambda_p/2$, yielding:

$$E_{max}/E_0 = a_0^2/2\left(1 + a_0^2/2\right)^{-1/2} \tag{2.30}$$

where $a_0^2 = 2.6 \times 10^{19}\ \lambda^2\ (\mu\text{m})\ I_0\ \text{W/cm}^2$. Given that $E_{max} \propto \lambda_p \sim (1/L)$, wakefield amplitude can be increased by operating at higher densities or shorter pulse durations. However, as the plasma density is increased energy gain can be limited by dephasing, as discussed in Section 2.4.1. For the HERCULES laser system, wakefield acceleration is driven in the nonlinear regime with a linearly polarized Gaussian pulse. The maximum wake amplitude for other pulse shapes can be found in Reference [7].

As LWFAs are driven with femtosecond duration laser pulses, the resultant electron bunches have similar duration [60, 61, 62]. These electron bunches and associated radiation sources are intrinsically synchronized to the laser drive, making LWFAs powerful sources for synchronized pump-probe experiments.

Regimes of LWFA

The linear 3D regime occurs in the limit where $a_0 \ll 1$ and is examined using the cold fluid equations: the Poisson equation, the continuity equation and the fluid momentum equation [7]. In the linear regime, the plasma wave is a simple sinusoidal oscillation with a frequency of ω_{pe}, and the associated electric field of the wave has the form:

$$E_z = E_0 sin\left(\omega_{pe}(z/v_{ph} - t)\right) \tag{2.31}$$

where z is the direction of laser propagation, v_{ph} is the phase velocity and E_0 is the peak field amplitude, estimated from the Poisson equation, $\nabla \cdot \bar{E} = 4\pi e(n_0 - n_e)$.

The bubble or blowout regime of LWFA is the most effective method for accelerating electrons. This regime is achieved when the laser pulse is less than half the plasma wavelength, which is achieved using sub-100 fs, high intensity laser pulses. In this regime, the ponderomotive force of the laser will expel all of the electrons in its focal volume, creating a spherical "bubble"-like plasma wave (Fig. 2.3). The

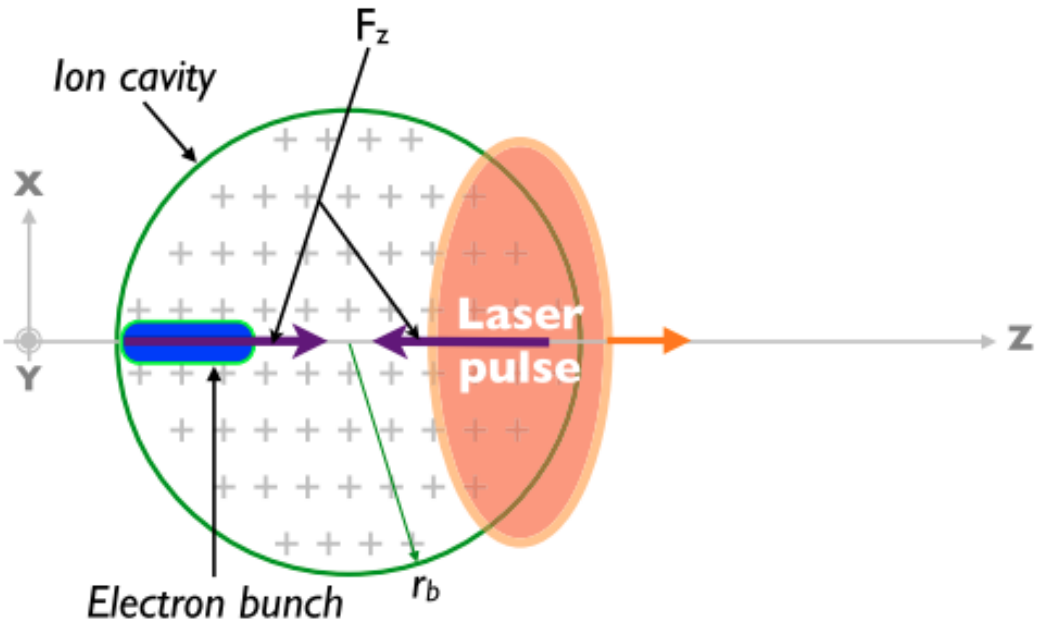

Figure 2.3: Electron acceleration in the bubble regime, where the ion cavity is approximated by a spherical wave with radius r_b. F_z is the longitudinal accelerating force. Figure reproduced with permission from Ref. [63]

electric field in the direction of propagation in the blowout regime can be defined by assuming an ionic cavity:

$$E_z = (m_e \omega_{pe}^2 \zeta)/2e \tag{2.32}$$

where $\zeta = z - v_g t$ in which v_g is the group velocity of the pulse. The maximum electric field is achieved at the edge of the plasma "bubble", which has a radius $r_b = 2\sqrt{a_0}c/\omega_{pe}$, and is zero at the center of the bubble [44].

Trapping

Electron trapping can be studied by considering the trajectory of electrons injected into a plasma wave. An electron with an initial velocity $v_z < v_{ph}$ will slip backward with respect to the plasma wave, and if the velocity is too low, it will never gain sufficient energy to remain in phase with the accelerating field. This electron will be untrapped and continue to move backward through the accelerating structure.

However, if the electron has a sufficiently high initial velocity, $v_z > v_{ph}$, the electron will become trapped, and will begin to orbit within the plasma wave [64, 65, 7].

Wave-breaking

Large amplitude electrostatic waves with phase velocities approaching the speed of light can be supported in a plasma. The wave breaking limit is defined as the maximum amplitude of an electrostatic wave within a fluid model (See [7] and citations therein).

The maximum amplitude of the electric field of a plasma wave can be made by assuming that all plasma electrons oscillate at ω_{pe}. Using the Poisson equation, the cold non-relativistic wave breaking field in the linear regime is given by:

$$E_0 = cm_e\omega_{pe}/e \tag{2.33}$$

For nonlinear plasma wave, it is possible for the maximum amplitude of the plasma wave to exceed E_0. In this case, the cold, relativistic wave-breaking field is defined by:

$$E_{WB} = \sqrt{2}\,(\gamma - 1)^{1/2}\,E_0 \tag{2.34}$$

where γ is the relativistic Lorentz factor associated with the phase velocity of the plasma wave. In the 1D, low-intensity limit $\gamma \simeq \omega_0/\omega_{pe}$.

In a warm plasma, thermal effects will reduce the maximum plasma wave amplitude by the thermal velocity spread of plasma electrons, $c\beta_{th} = (k_B T_0/m_e)^{1/2}$ where T_0 is the initial electron plasma temperature and k_B is the Boltzmann constant. Under these conditions, the wave breaking field becomes [7]:

$$E_{WB} \simeq E_0/\beta_{th}^{1/2} \tag{2.35}$$

2.4.4 Direct Laser Acceleration

DLA refers to the regime in which electrons gain energy directly from the laser field. Using pulse durations exceeding the plasma frequency and ultra-relativistic intensities ($a_0 \gg 1$), the laser pulse will expel nearly all of the electrons within the focal volume by a sustained ponderomotive pressure, creating charge separation and ultimately a quasi-static channel. Electrons that become trapped in the ion channel can be accelerated *via* DLA. DLA can occur concurrently with LWFA and SM-LWFA [17, 66].

The plasma channel created by an ultra-relativistc picosecond duration laser pulse evolves and has its own quasi-static transverse and electric fields [67, 68, 69]. Therefore, DLA is very complex due to the interplay of electrostatic fields in the evolving plasma channel with the oscillating electric fields of the driving laser pulse [38, 70, 71, 35]. There are several mechanisms that can contribute to electron acceleration in this interaction. Previous computational studies have highlighted the role of transverse oscillations on electron oscillation, leading to a resonance between the electron oscillations and the driving laser pulse and thereby enhancing electron energy gain [35, 70, 71]. Betatron oscillations due to the magnetic field of moving electrons may also enable reduced dephasing between high energy electrons and the laser field *via* DLA [35]. Amplification of electron oscillations across the plasma channel has also been found to significantly increase electron energy, and a longitudinal electric field directed in opposition to the laser electric field can decrease the electron dephasing rate [72, 73, 68, 67]. Additionally, even a small difference between the phase velocity of the wave and the speed of light can alter electron dynamics during DLA with sufficiently intense laser pulses, reducing the maximum achievable electron energy [74]. Electrons may also gain energy stochastically through perturbations to

the electron trajectory [37, 75].

2.4.5 Betatron Radiation

Electrons that become trapped in plasma waves or plasma channels will undergo oscillations, emitting a bright source of X-rays with a source size as small as one micrometer. [15, 16, 17]. This motion is known as *betatron oscillations*, and is associated with the generation of EM radiation as observed from an undulator in a conventional accelerator. Betatron X-ray beams produced *via* LWFA have been shown to produce stable, bright X-ray beams capable of high-resolution tomographic imaging [16, 18, 19, 20, 21, 22, 43]. The resultant beams have a low divergence (on the order of a few milliradians [23]) and ultrashort duration (less than 100 fs [24]), making them useful for a large range of applications across engineering, medicine, homeland security and science [16, 19, 20, 17, 21, 22].

Following the description of LWFA in the bubble regime as an ionic cavity, as discussed in Section 2.4.3, the equation of motion of an electron undergoing betatron oscillations within the plasma bubble due to the transverse field of the plasma wave, which acts as a restoring force toward the laser propagation axis. Under these conditions, the equation of motion on an electron in a plasma bubble can be written as [44]

$$\frac{d\bar{p}}{dt} = -\frac{1}{2} m_e \omega_{pe}^2 \bar{s} \tag{2.36}$$

where $\bar{s}$ represents the coordinates the in frame of the bubble, which is moving at the group velocity of the laser pulse, v_g. Under the assumption that the longitudinal momentum is slowly varying, the transverse momentum can be considered as a slowly varying oscillator with at betatron frequency, $\omega_\beta = \omega_{pe}/\sqrt{2p_z}$. By applying the WKB approximation the equation of motion can be solved for the p_x, and using the

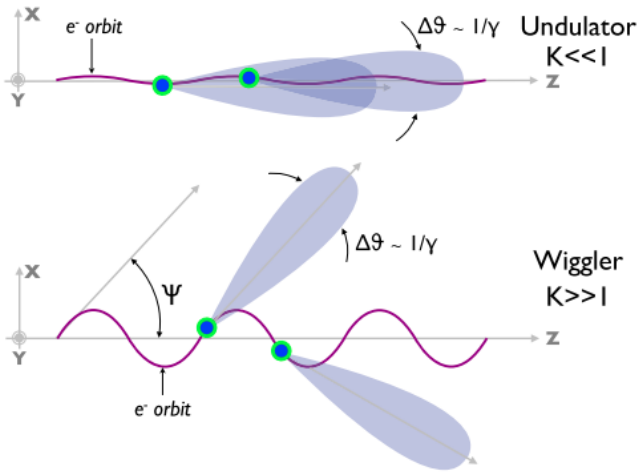

Figure 2.4: Illustration of betatron radiation in the "undulator" and "wiggler" limits, where the instantaneous direction of radiation emission is represented by lobes. Figure reproduced with permission from Ref [63].

position and momentum of the electron the intensity of radiation emitted by the moving particle per unit frequency is given by [76]:

$$\frac{d^2I}{d\Omega d\omega} = \frac{e^2\omega^2}{2\pi c}\left|\int_{-\infty}^{\infty} \bar{n}\times(\bar{n}\times\bar{v}/c)e^{i\omega(t-\frac{\bar{n}\cdot\bar{r}}{c})}dt\right|^2 \tag{2.37}$$

where Ω is the solid angle and $\bar{n}$ is the vector in the direction of observation.

Depending on the oscillating strength, electrons will oscillate in two regimes: the "wiggler" and "undulator" regimes (Fig. 2.4). In the undulator regime, the electron will radiate in the same direction over its trajectory This occurs when the maximum angle between electron velocity and the propagation axis, ψ, is smaller than the radiation cone $\Delta\theta = 1/\gamma$, where θ is the angle from the plane in which the particle oscillates. Conversely, in the wiggler regime, radiation will emit in different directions along the electron trajectory. The transition between these regimes is defined by the ratio between oscillating amplitude and wavelength, defined by the dimensionless parameter $K = \gamma\psi$ [63].

In the wiggler configuration, emitted radiation is most synchrotron-like, with the electrons undergoing very strong oscillations. This can be described by the asymp-

totic limit of Equation 2.37, as a function of θ [44]:

$$\frac{d^2I}{d\Omega d\omega} \propto \frac{\gamma^2\zeta^3}{1+\gamma^2\theta^2}\left[K_{2/3}^2(\zeta) + \frac{\gamma^2\theta^2}{1+\gamma^2\theta^2}K_{1/3}^2(\zeta)\right] \tag{2.38}$$

where $K_{2/3}^2$ and $K_{1/3}^2$ are modified Bessel functions, and $\zeta = \frac{\omega_\beta}{\omega_c}(1+\gamma^2\theta^2)^{3/2}$ is defined in terms of the critical frequency and the betatron frequency. The betatron spectrum can then be obtained by integrating this function over the solid angle, Ω:

$$\frac{dI}{d\omega} = \sqrt{3}\frac{e^2}{c}\gamma\frac{\omega}{\omega_c}\int_{\omega/\omega_c}^{\infty} K_{5/3}(x)dx \tag{2.39}$$

where $K_{5/3}^2$ is also a modified Bessel function. The critical frequency of a synchrotron spectrum is defined as [76]

$$\omega_c = \frac{3}{2}\gamma^3\frac{c}{\rho} \tag{2.40}$$

where ρ is the curvature of the electron orbit. The synchrotron-like spectrum produced by a moving electric field at a single and at various amplitudes of betatron oscillation is shown in Figure 2.5, where the amplitude of oscillation is defined by the size of the plasma bubble (c.f. Section 2.4.3).

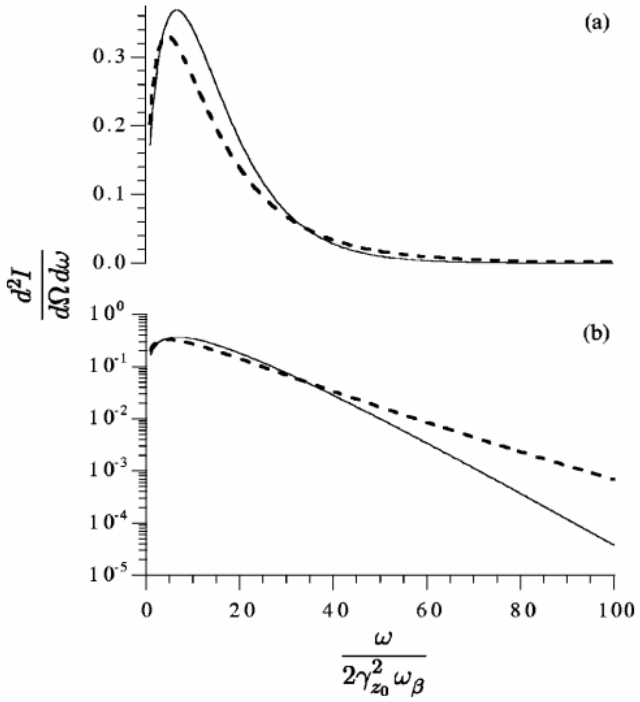

Figure 2.5: The synchrotron-like spectrum from an electron undergoing betatron oscillations at a constant amplitude on a linear (a) and logarithmic (b) scale. The variation in spectrum over a Gaussian distribution of betatron amplitudes is shown as a dotted line. Figure reproduced with permission from Ref. [77].

CHAPTER III

Methods

3.1 High power laser systems

The experiments presented in this dissertation were conducted using three high-intensity laser systems: the HERCULES laser in the Center for Ultrafast Optical Science (CUOS) at the University of Michigan in Ann Arbor, USA, the OMEGA EP Laser Facility at the University of Rochester Laboratory for Laser Energetics in Rochester, USA and the Gemini Laser System at the Central Laser Facility at the Rutherford Appleton Laboratory in Didcot, UK.

Laser systems, laser targets and diagnostics relevant to experiments on these systems are discussed in this chapter. Supporting Particle-in-Cell (PIC) simulations were performed to elucidate the underlying physics of these experiments; the PIC method is also discussed.

3.1.1 The HERCULES laser system

The HERCULES (High Energy Repetition CUOS LasEr System) laser is a Ti:Sapphire laser system capable of delivering 3 Joules of energy in 30 fs laser pulses (300 TW). HERCULES delivers pulses with a peak repetition rate of 0.1 Hz. It holds the Guinness Record for peak laser intensity, with a focused intensity of 2×10^{22} W/cm^2 [5].

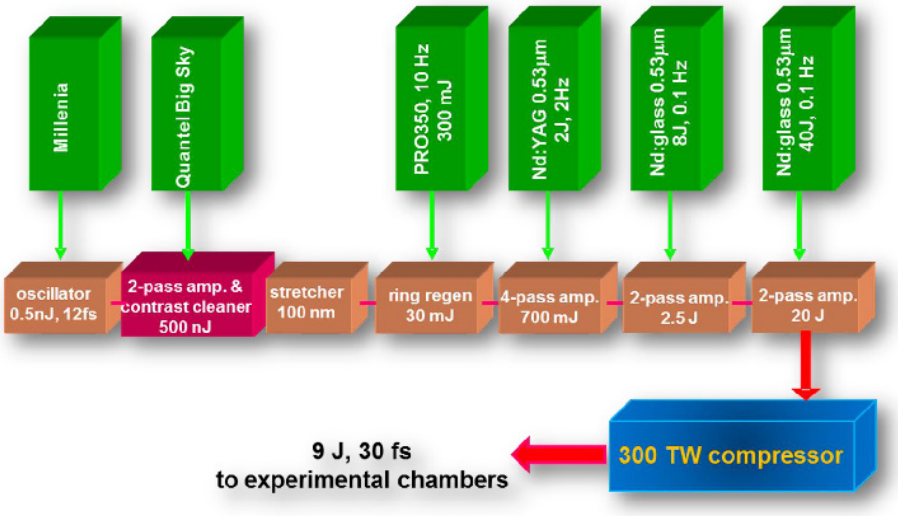

Figure 3.1: Schematic of the HERCULES system. Figure from the CUOS website.

HERCULES laser is a CPA system. A Femtolaser oscillator with 12 fs pulse width with 800 nm wavelength is initially amplified to the microjoule energy through a two-pass preamplifier system. Amplified Spontaneous Emission (ASE) noise introduced by the two-pass amplifier is then removed using cross-polarized-wave generation. The microjoule level pulse is then stretched to 0.5 ns and a regenerative amplifier and 4-pass amplifier system are used to enhance the pulse energy to the joule level. Following two sequential Ti:sapphire 4-pass amplifiers (25 mm beam diameter) and a

single 3-pass Ti:sapphire amplifier (50 mm beam diameter), the final output energy of the laser beam is 17 J. A schematic of the laser system is given in Figure 3.1.

Using a 4-grating compressor, the output laser pulse is compressed to approximately 30 fs. Achromatic lenses are used in the final relays of the beam to prevent variation in the group delay across the beam due to its large diameter in the compressor (150 mm). Following compression, the beam is down-collimated to a diameter of 100 mm and approximately 3 J of energy is delivered into one of two separate interaction chambers: the gas target chamber for LWFA experiments and the solid target chamber for ion acceleration and high-harmonic generation studies. The work presented in this dissertation was performed in the gas-target experimental chamber.

3.1.2 The OMEGA EP laser system

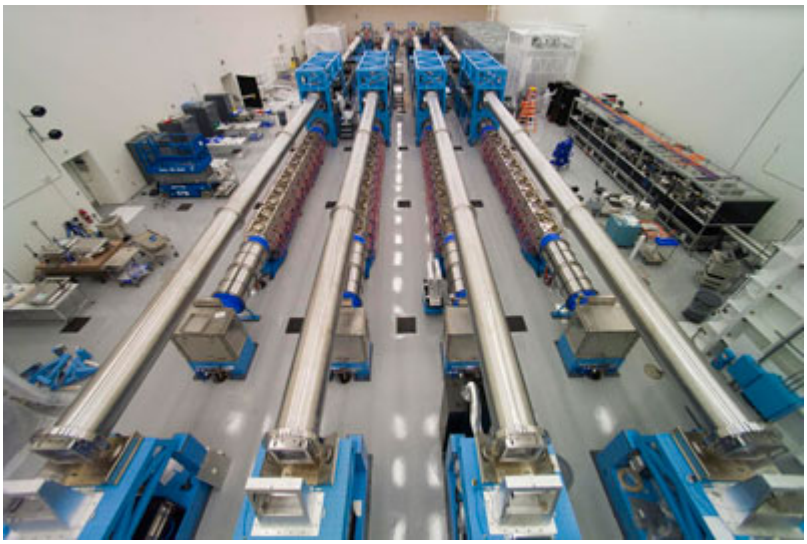

Figure 3.2: A view of the OMEGA EP beamlines. Figure from the Laboratory for Laser Energetics website.

The OMEGA Enhanced Performance (EP) laser system is part of the University of Rochester Laboratory for Laser Energetics. It has four kilojoule class independent beamlines, two of which can be compressed for picosecond duration operation with petawatt power.

The OMEGA EP short pulse beams have a wavelength of 1053 nm and can be configured to provide up to 0.5 kJ of energy at a best compression duration of 0.7 ps or 2.3 kJ in 100 ps. The peak intensity of this system is 6×10^{19} W/cm^2 . The short pulse beams can be focused to contain 80% of the laser energy into a diameter of approximately 30 μm.

Two long pulse beams are also available on OMEGA EP. These beams can be tuned to have a pulse duration of 0.1 to 10 ns at a wavelength of 351 nm and delivering energies up to 5 kJ. Distributed Phase Plates are used to produce super Gaussian focal spots ranging from 400 to 2000 μm.

3.1.3 The Gemini laser system

The Gemini laser system is part of the Central Laser Facility at the Rutherford Appleton Laboratory (RAL). The Gemini laser system is a two-beam petawatt class facility. Each beam delivers up to 15 J of energy in a pulse of 30 femtosecond duration, yielding up to 500 TW of laser power. Gemini is the final amplification stage of the "Astra-Gemini" system, which is a Ti:Sapphire CPA system pumped by frequency doubled Nd:YAG and Nd:Glass lasers. The Astra laser produces 0.75 J in 30 fs. The Gemini laser was a later addition of an extra amplifier to the existing Astra laser. A pulse picker at the Astra compressor splits the initial beam into two beamlines, which are fed into Astra and Gemini. The Gemini amplification system consists of two separate beamlines, each of which is amplified from 1.5 J to 25 J using separate 60 J Nd:Glass pump systems. Two separate compressors produce 15 J of energy in a 40 fs duration pulse, which is delivered to the Gemini target area.

3.2 Gas Targets

All of the experiments presented in this dissertation examine the interaction of an intense laser pulse with an underdense plasma. For LWFA experiments, a sustained column of low-density plasma is required to trap and accelerate electrons in plasma waves. In practice, three types of gas targets are typically used: gas jet, gas cells (capillaries), and pre-ionized capillary targets [78].

Gas jets are typically of millimeter diameter and are opened for several milliseconds prior to the laser shot to achieve "steady-state" conditions relative to the surrounding vacuum environment on the timescale of the laser pulse. Gas jets are simple, easy to align and robust for producing low density plasma targets, however they are limited by the amount of gas necessary to achieved desired densities and low shot-to-shot reproducibility of gas conditions.

In order to produce stable, high-quality electron bunches *via* LWFA it is desirable to minimize fluctuations in plasma targets. This is achieved using gas cells and capillary targets. Gas cells are able to produce uniform density profiles at lower gas pressure and with greater stability due to the containment of the gas, and have been shown to produce electron beams with enhanced stability in beam energy, charge, divergence and pointing [79]. Long, narrow capillary cells containing gas have also been pre-ionized using an electrical discharge to produce a density gradient through thermal expansion that can enable optical guiding of laser pulses [80].

Further, for LWFA experiments precise control of the gas density profile is crucial. For example, while high-density gas is beneficial for producing high charge beams through self-injection, the electron beam will rapidly dephase from the laser pulse and experience deceleration by the reversed electric field of the wake, limiting the

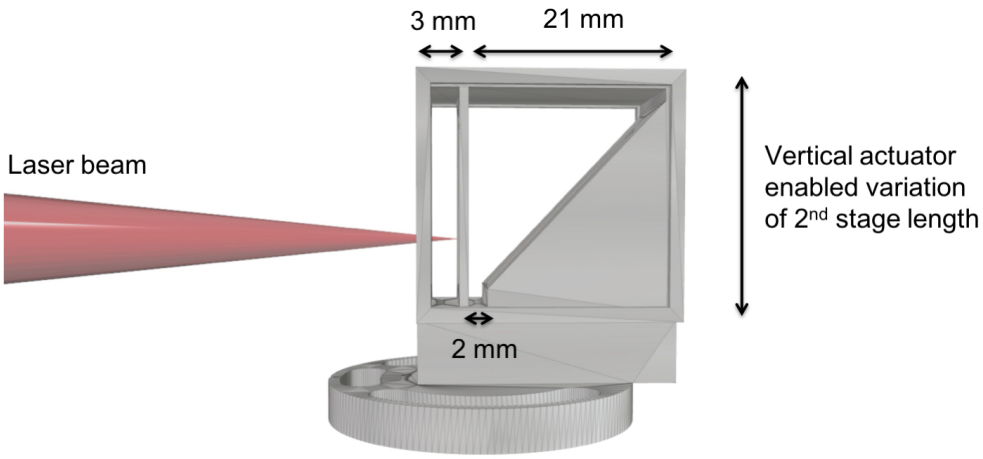

Figure 3.3: CAD model of the variable length two-stage gas cells used in LWFA experiments. A 45° wall in the second stage enabled variation of the length of the second stage (between 2 to 21 mm) using linear motor controls to vary the vertical position of the cell.

maximum energy of the resultant beam (c.f. Section 2.4.1). A separation between the injection and acceleration processes by density tailoring can enable the production of high-charge, high-energy beams. Two-stage 3D printed gas cells developed at the University of Michigan have demonstrated advancements in beam stability and reprodubility as compared to single stage cells [78]. 3D printing enables rapid protyping and decreased cost in gas cell production. Variable length cells have also been constructed using a 45° slope in the second cell and a vertical actuator, as shown in Figure 3.3. These gas cells are designed to hold glass windows such that a probe beam can travel transversely through the cell for plasma density measurements by interferometry, as will be discussed in Section 3.4.1.

Gas jet targets are employed in Chapters V and VII of this work. Gas jets were used in Chapter VI in which backward scattered radiation was measured because reflection of incident laser light from gas cells was found to interfere with the desired measurements. Two-stage 3D printed gas cells with a short, first stage injector was employed in Chapter VII to achieve high energy, high charge electron beams, and

were reversed in Chapter V to test the effect of density tailoring on long wavelength generation. Characterization of the plasma density in gas targets is achieved using interferometry and discussed in Section 3.4.1. Accelerated electron beams are measured using a magnetic spectrometer, discussed in Section 3.4.3, and a description on X-ray characterization is given in Section 3.4.4.

3.3 Laser diagnostics

Diagnostics capable of measuring the output of the laser beam are essential for monitoring the conditions for each single experiment (shot), and well as the operation of the laser system. In this system, the laser diagnostics used on the HERCULES laser system are discussed.

3.3.1 Laser power

A photodiode located behind a dielectric mirror in the HERCULES system is used to measure the laser power on a shot-to-shot basis. Although 99% of the laser energy is reflected from the front surface of a dielectric mirror and maintained in the system, the remaining 1% that leaks through the mirror is sufficient to obtain signal on the photodiode, and is read in the control room using an oscilloscope. This value is correlated with the power in the full beam using a calibrated power meter in the HERCULES beam. Therefore, assuming the laser system is operating consistently at a fixed pulse duration and the photodiode is not saturated, a measure of the total power in the HERCULES beam can be obtained on each shot.

3.3.2 Laser pointing

Proper alignment of the HERCULES beam into the experimental chamber is essential for achieving optimal experimental conditions and shot-to-shot reproducibility of measurements. Therefore, the gas target chamber of the HERCULES system is

equipped with two alignment steps following the entrance of the beam to the chamber from the compressor.

The first beam alignment in the HERCULES chamber is achieved by monitoring the beam pointing to ensure that the beam is parallel to the optics table and enters the chamber at the center of the entrance port. Consistent alignment of beam pointing is achieved by measuring the leak through of laser light from the rear of a dielectric mirror inside of the experimental chamber. The leak through light is imaged using a fixed imaging system, and the pointing of the laser beam is controlled using a mirror outside of the experimental chamber, after the compressor.

The beam is subsequently aligned to the target chamber center (TCC), where the gas target is located at the focus of the parabolic mirror. Alignment to TCC is achieved by interrupting the beam coming to focus from the parabolic mirror using two small pick off mirrors on a motorized stage. When these mirrors are moved into the path of the focusing beam it can be redirected to a stationary imaging system on which the focal spot is monitored. This imaging system is fixedya at a location corresponding to TCC so that the position and quality of the focal spot can be reproduced with each alignment.

3.3.3 Focal spot

Monitoring of the laser focal spot is essential for ensuring optimal laser performance. On HERCULES the focal spot at best focus from the parabolic mirror is measured during alignment at TCC using an imaging camera, as previously discussed. This imaging system consists of an 8-bit charge-coupled device (CCD) camera and an objective lens with ten $\times$ magnification.

In the HERCULES chamber, an f/20 parabolic mirror is used to focus the beam, where f/20 refers to the f-number $N = f/D$, where f is the focal length and D is

the effective aperture size. Using a perfect lens, the diffraction limited spot size of focused light can be described as an Airy disk, and the concentric rings around the Airy disk are an Airy pattern. The diffraction limited spot can be approximated as the diameter of the first null in an Airy disk:

$$x = 1.22\lambda N \tag{3.1}$$

where λ is the wavelength and N is the f-number of the imaging optic. Therefore, the diffraction limited spot on HERCULES using an f/20 parabolic mirror is about 20 μm.

In many experiments, a deformable mirror may be used to optimize the wavefront of the laser beam and obtain diffraction limited spot sizes. However, LWFA experiments can also be successfully performed without corrections to the wavefront through careful alignment of the optical system and utilizing high-quality focusing off-axis parabolic mirrors.

The best focus of the laser should be checked not only for high quality at focus, but also to minimize the formation of astigmatic qualities of the beam. In practice, utilizing a translation mount enables scanning through best-focus to investigate beam quality.

3.3.4 Pulse duration

The characteristics of electron acceleration, and regime of operation of LWFA, is highly dependent on the duration of the driving laser pulse. For this reason, it is important to monitor the pulse duration experimentally. On the HERCULES system, the pulse duration can be measured by sending light from the low-power regenerative amplifier into a second-order autocorrelator.

Given the ultra-short duration of HERCULES pulses these sub-picosecond pulses

can only be measuring using the pulse itself. This is what is achieved with the second-order autocorrelator, which works by splitting an ultra-short pulse into two halves using a beam splitter and sending one of these pulses into a delay stage. Both pulses are then combined into a non-linear second harmonic generation (SHG) crystal, which emits second harmonic light as a result of its interaction with these beams. By charging the delay of one beam relative to another the second order emission can be calibrated. As the overlap in the SHG crystal differs due to varying temporal delays, the spatial distribution of the emitted light will also change [81]. The spatial distribution of second harmonic light is proportional to the duration of the input pulse, and assuming a certain pulse shape the duration of the laser pulse can be measured. For HERCULES beams the shortest pulse duration is 33 fs (Fig. 3.4).

As well as knowing the pulse duration, it is also important to determine the shape of the pulse and the existence of any features, such as pre or post pulses. From second-order autocorrelation measurements information about the pulse shape cannot be determined. Additionally, information about the leading or trailing edge of the pulse is lost in the second-order autocorrelator because it is symmetric. However, information about pre- and post-pulse structure can be resolved if the symmetry of the system is broken, as achieved with a third-order autocorrelator.

3.4 Interaction diagnostics

Single-shot diagnostics of laser-plasma interaction and resultant electron and radiation are essential for laser-plasma acceleration studies. General methods for characterizing plasma density and beam properties are discussed in this section.

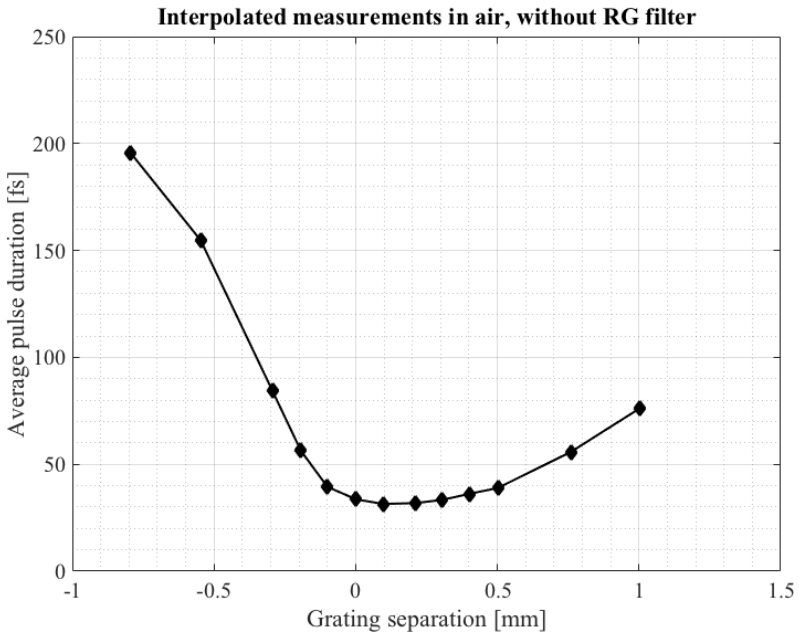

Figure 3.4: Measurement scan of the HERCULES pulse duration made by changing the separation of compressor gratings.

3.4.1 Interferometry

Optical interferometry is used to measure the electron plasma density in laser-plasma experiments. Interferometry is a powerful technique for determining plasma density from interference fringes. Interferometric imaging also enables imaging of plasma channel formation and structure.

On the HERCULES laser system, plasma density is measured using a shearing Michelson interferometer. A Michelson interferometer uses a beam splitter to split a light source into two arms which are later recombined to obtain interference fringes. In the HERCULES gas target chamber, light for the interferometer is picked off from the main interaction beam using a nitrocellulose pellicle of 2 μm thickness, which reflects 4% of the incident light along a separate optics line. The optics in the probe line path are 50.8 mm in diameter, and the length of the probe line is adjusted using a delay stage so that the probe pulse traverses the plasma about a picosecond after

the main pulse. The single, 2-inch diameter probe beam travels transversely through the gas target producing the reference region and interaction region in a single beam. Light that exits the gas cell travels to the Michelson interferometer.

The interferometry probe beam will pass through the region of laser-plasma interaction as well as a vacuum or unperturbed region, and is later split to separate these conditions. The Michelson interferometer on HERCULES consists of a beam splitter, a roof prism, a mirror and a CCD camera. The two-inch beam entering the interferometer is split into two arms using the beam splitter, and one arm travels to a mirror on a translation stage, and the other to a roof prism. The roof prism flips the incoming image of the interference and reference images and reflects this image back to the beam splitter. The initial image and the flipped image are interfered on the CCD camera. Using the mirror translation stage, the delay between the two arms can be adjusted to obtain interference fringes, from which the plasma density can be calculated from the relative phase shift.

By interfering the laser-plasma interaction region with an unperturbed region, the plasma density can be obtained by measuring the relative phase accumulation gained by light passing through a plasma structure:

$$\Delta\phi = \frac{2\pi L}{\lambda_0}\Delta\eta \tag{3.2}$$

where λ_0 is the wavelength of the probe beam, L is the thickness of the medium and $\eta = \Delta\left(1-\omega_{pe}^2/\omega^2\right)^{1/2}$ is the refractive index. The plasma density, n_e, can be extracted from the plasma frequency, $\omega_{pe} = n_e e^2/\epsilon_0 m_e$.

The plasma density can be extracted from interference fringes to using the Fourier-transform method to determine the two-dimensional phase shift:

$$\Delta\phi(x,r) = \frac{2\pi}{\lambda}\left(\sqrt{1-\frac{n_e(x,r)}{n_c}}-1\right) \simeq \frac{\pi}{\lambda}\frac{n_e(x,r)}{n_c}dl \tag{3.3}$$

where $n_c = m_e\omega_0^2\epsilon_0/e^2$ is the critical plasma density, and $n_c \simeq 2\times\ 10^{21}$ cm^{-3} for $\lambda_0 = 800$ nm. Small asymmetries in the plasma channel are accounted for using a numerically computed Abel inversion. This analysis is performed using a routine written in MATLAB.

Density values obtained from interferometric images have shot-to-shot variations on the order of 10%, and the quoted values refer to the peak electron density on the laser axis. The uncertainty in these measurements typically arises from non-uniformity of gas within the gas cell or above the gas nozzle.

3.4.2 Stimulated Raman Scattering

The measurement of Stimulated Raman Side Scattering is another method for determining the plasma density in laser-plasma experiments. This method was employed in experiments performed on the Gemini laser system (Chapter VII). Light propagating through a plasma will be modulated by the Raman instability, producing a spectrum with satellites corresponding to integer n shifts of the fundamental frequency:

$$\omega_s = \omega_0 \pm n\omega_{pe} \tag{3.4}$$

Measurements of Stimulated Raman Side Scatter were obtained using an absolutely calibrated imaging spectrometer. The plasma density can be determined by recovering ω_{pe} from the position of these satellites using $n_e = m_e\omega_{pe}^2\epsilon_0/e^2$ [82].

3.4.3 Electron spectrometer

The characteristics of accelerated electron beams are determined using an electron spectrometer. The electron spectrometers used in LWFA studies presented in this work consisted of a dipole magnet which deflects the electron beams according to their momenta onto a LANEX scintillating screen.

On HERCULES, the electron beam exiting the plasma target will enter a 0.8 Tesla dipole magnet of length 15 mm and with a separation of 2 cm between the plates. The magnetic field is oriented such that the magnetic field lines are vertically normal to the direction of propagation, sweeping electrons in a plane parallel to the ground. To minimize detrimental effects from the magnetic fringe fields, the distance between the plates is optimized such that the radii of deflection of electrons within the desired energy rate are larger than the separation between the plates.

To understand the principle of an electron spectrometer, consider an electron traveling along the laser axis (z), with energy γ and velocity $\bar{v} = (v_x, v_y, v_z)$. This electron enters a uniform magnetic field, $\bar{B} = (B, 0, 0)$, with length L_z and width W_y, and be subject to the $v \times B$ force from the Lorentz force equation, yielding:

$$\frac{dv_x}{dt} = 0 \tag{3.5}$$

$$\frac{dv_y}{dt} = -\frac{Bqe}{\gamma m_e} v_z \tag{3.6}$$

$$\frac{dv_z}{dt} = \frac{Bqe}{\gamma m_e} v_y \tag{3.7}$$

By differentiating Equation 3.6 and plugging in Equation 3.7, and vice versa, it is found that the electron is undergoing simple harmonic motion at the cyclotron frequency, $\omega_B = Bq_e/\gamma m_e$. Integrating these equations it is found that the electron is moving in the (y, z) plane along a circle of radius $R_B = v/\omega_B$. Therefore, over the width W_y, the exit angle of the electron from the magnet is given by $\sin\theta = L_z/R_B$ with respect to the z-axis, and the perpendicular deflection of the electron is given by $\nabla y = R_b(1 - \cos\theta)$. The electron exiting the magnet will will be dispersed according to its initial energy and will intersect with a LANEX scintillating screen. The LANEX screen will fluoresce at a wavelength of approximately 545 nm and with

an intensity proportional to the number of electrons striking it [83]. In this way, the energy, energy spread, and divergence of the electron beam can be determined from images taken with a CCD. The electron spectrometer is calibrated by mapping the magnitude of the magnetic field inside the dipole, and tracking the trajectories of particles onto the scintillating screen.

3.4.4 Radiation characterization

X-ray CCDs

CCD cameras will respond to incident photon by the photoelectric effect, and the number of photoelectrons produces from a single photon depends on the fraction of energy that is deposited on the chip. This is known as the quantum efficiency of the sensor. The quantum efficiency of CCD cameras are highly dependent on photon energy, therefore X-ray and optical CCD cameras differ by the amount of signal generated by an incident photon on the sensor chip. The photon energy of X-rays is much higher than photons in the optical range, and will produce a high signal per pixel on the sensor. Therefore, in X-ray CCDs, sensors capable of high photon absorption are used.

For X-ray characterization studies in Chapter VII, an Andor iKon-L camera was used to image X-ray transmission through a filter pack (Fig. 3.5a). The sensitivity of this Andor camera is highest for photons in the range of 1 - 10 keV, but can be used to detect photos up to 20 keV (Fig. 3.5b). The analogue-to-digital conversion of this camera, also known as the gain, is 7 photoelectrons per count (25.55 eV/count). The CCD chip of this camera is 2048 $\times$ 2048 pixels of 13.5 $\times$ 13.5 μm^2, with a dynamic range of 16 bit. A 250 μm beryllium filter is typically used in front of an X-ray CCD camera to filter out background radiation.

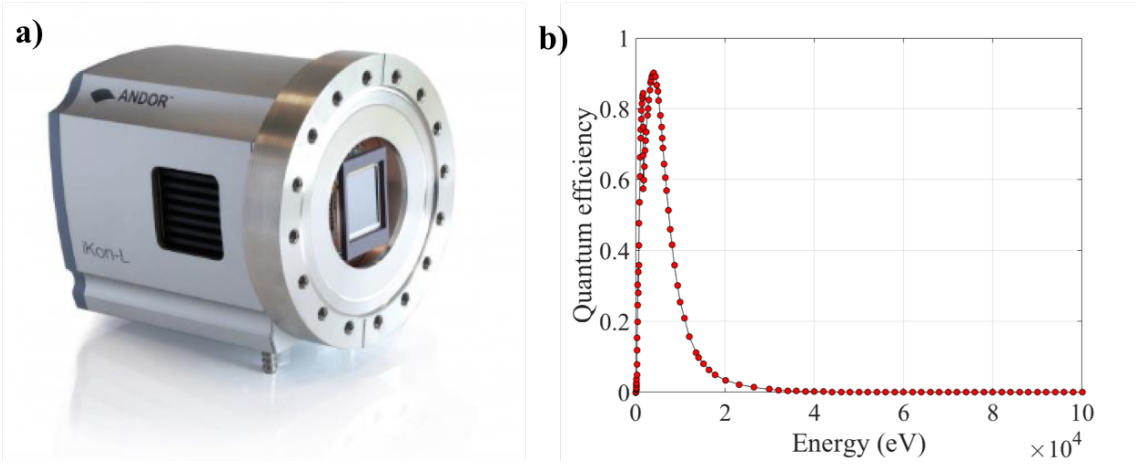

Figure 3.5: **a)** Andor-iKon-L camera used to image X-ray transmission. **b)** Quantum efficiency of the Andor camera.

Filter arrays

The spectrum of betatron radiation is important for X-ray imaging applications, as discussed in Chapter VII. To characterize the betatron spectrum a 9-element filter array composed of various materials with different K-edges was placed to characterize the X-ray spectral distribution. To capture the spatial profile of the X-ray beam the filters were placed in a cross pattern, with the series of nine elements repeating 5 times, as shown in Figure 3.6a. The transmission of X-ray photons through each material used in the filter is highly dependent on the energy of the incident photon, therefore using a variety of filters the broadband betatron spectrum can be obtained. The thickness of each filter element can be found in Table 3.1. The raw X-ray image with labeled filters and associated transmission are shown in Figure 3.6.

The signal of the X-ray spectrum on the camera is assumed to be synchrotron-like and can be estimated as [84]:

$$N_i = \eta \int_{E_{min}}^{E_{max}} S(E, E_{crit}) Q(E) T_i(E) dE \tag{3.8}$$

where η is a constant coefficient, $S(E, E_{crit}) \sim (E/2E_{crit})^2 K_{2/3}^2(E/2E_{crit})$ is the

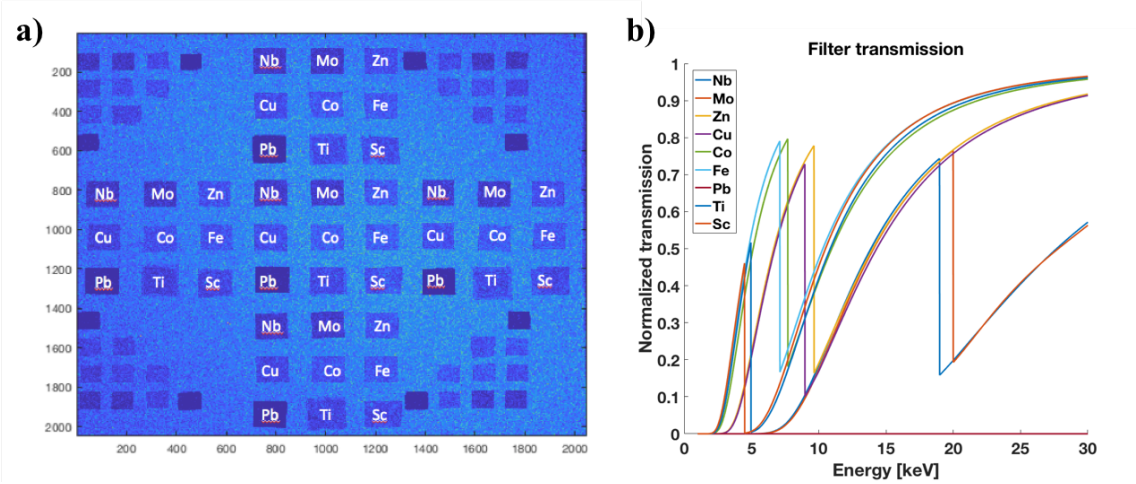

Figure 3.6: **a)** Cross pattern of repeating 9-element filter array. **b)** X-ray transmission of each element.

on-axis synchrotron spectrum with a critical energy of E_{crit}, $Q(E)$ is the quantum efficiency of the camera (discussed above), T_i is the overall transmission of the filter i with the consideration of attenuation of other materials in the beam path. Fitting equation (3.8) with the measured signal counts on the camera for all the filters gives a best fitted E_{crit}. The number of photons in the X-ray beam can be determined by integrating the assumed synchrotron spectrum, accounting for the quantum efficiency of the detector.

Material:	Nb	Mo	Cu	Zn	Fe	Co	Sc	Ti	Pb
Thickness (μm):	24.5	20.0	9.2	10.0	5.6	5.4	26.7	17.3	503.8

Table 3.1: Thickness of filter array elements.

Radiochromic Film

Radiochromic Film (RCF) is a thin plastic film with an active layer containing dye that is sensitive to ionizing radiation from electrons, ions and X-rays. It has high spatial resolution, and is an excellent diagnostic for laser-plasma experiments as it is insensitive to optical radiation. The photo-sensitive component in RCF which undergoes a photo-chemical reaction when exposed to ionizing radiation, producing

a color change in the otherwise transparent film. The intensity of the radiation will translate into the depth of the color on the film, therefore the dose of incident radiation can be inferred from the optical density of the film.

RCF was utilized in experiments conducted on the OMEGA EP laser facility to diagnose the beam pointing and divergence of laser-accelerated electron beams. The type of film used in these experiments was HDV2, which has a dynamic dose range of 10 to 1000 Gy and develops in real time without post-exposure treatment. The spectral response of this film ranges from 100 keV to MeVs, and can be used to resolve features smaller than 5 μm.

3.4.5 Infrared detectors

Near infrared spectrometer

A NIRQuest512-2.5 spectrometer was used in Chapter V to measure the spectrum of radiation produced between 1 and 2.5 μm during LWFA. The NIRQuest512 is a Symmetrical Crossed Czerny Turner, with 8 gratings and a 25 μm slit width. The detector in this spectrum was a Hamamatsu G9208-512 W (Indium Gallium Arsenide), with 25 $\times$ 250 μm pixel size, providing measurements between from 900-2500 nm wavelength range. Spectral measurements were corrected for the grating efficiency and photosensitivity of the detector (Fig. 3.7).

Pyrometer

When exposed to a radiation source, a pyroelectric thermal detector produces a current output that is proportional to the rate of change of temperature. The output current from these devices is governed by:

$$I = p(T)A\frac{dT}{dt} \tag{3.9}$$

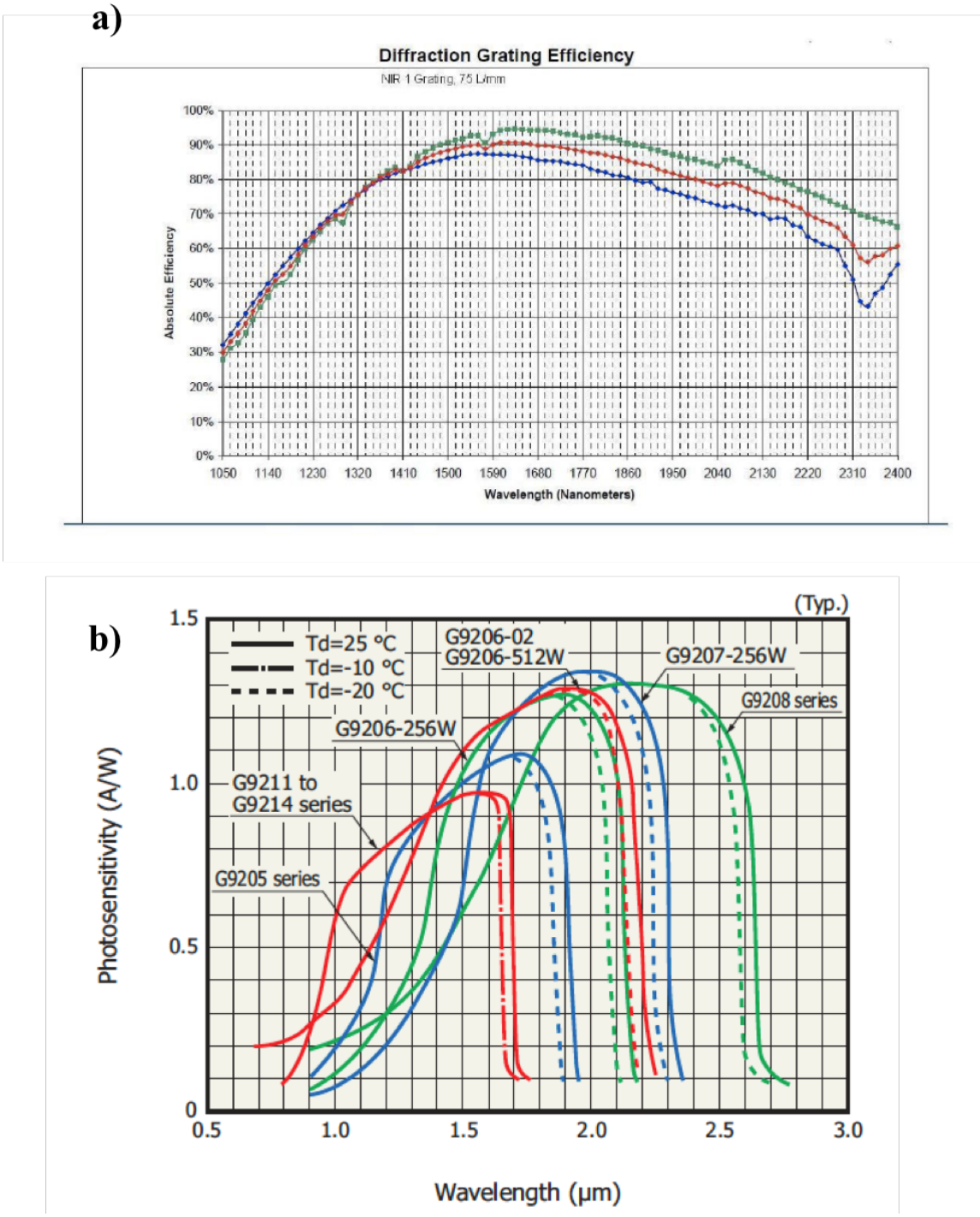

Figure 3.7: **a)** Grating efficiency of the NIRQuest512-2.5 spectrometer, from Ocean Optics. **b)** Photosensitivity of the Hamamatsu G9208 Indium Gallium Arsenide detetor, obtained from the manufacturer.

where p(T) is the pyro-electric coefficient, A is the area of the detector, and dT/dt is the rate of temperature change of the pyroelectric crystal, which will generate electricity when it is heated. Pyroelectric detectors can operate at room temperature, have a broad spectral response, and operate with sub-nanosecond response times. In this work, a Gentec-EO QS3-IL pyrometeric detector was employed to measure the total energy in light extending from 1 μm during LWFA (Chapter V). This detector was calibrated as 3.35×10^5 V/J ($\pm$ 3.5 %) using a 7.25 μJ source and measurements of the signal of the detector were made using an oscilliscope.

3.5 Particle-in-Cell simulations

Particle-in-cell (PIC) codes are widely used in plasma physics for simulating collisionless plasma kinetics. The core of a PIC code consists of two coupled solvers: the particle pusher and the field solver. The particle pusher moves electrons under the influence of electromagnetic fields and calculates resultant currents, while the field solver solves Maxwell's equations on a fixed spatial grid subject to the currents from the particle pusher. In this way, the dynamics of a collisionless, kinetic plasma can be simulated.

The PIC method groups individual particles together to form macro particles with preserved charge-to-mass ratios such that the equations of motions and macroscopic fields are unchanged. The motion of these macroparticles is then tracked on a grid (Fig. 3.8a), subject to self-consistent electric fields. With each step, the phase space of macroparticles is updated according to the equations of motion, the particles are distributed using a weighted distribution, and Maxwell's equations are solved with the updated current and charge densities at each point (Fig. 3.8b).

The accuracy and speed of PIC simulations are determined by the number of

particles, as well as the grid-size and time-step of the simulation. The maximum time-step for a given grid-size is determined through the Courant criterion. The Courant criterion dictates the time-step for a numerically stable scheme ($\nabla tc \leq \Delta x$), and is typically chosen to be its maximal allowable value to reduce dispersion of the wave due to the grid size. For lasers of relativistic intensity interacting with plasmas below the critical density it is not necessary to resolve the Debye length of the plasma ($\lambda_D \simeq \sqrt{\epsilon/4\pi ne^2}$). This is because numerical heating, caused when the grid size exceeds the Debye length, is negligible because for low densities the wave propagation in an underdense plasma is similar to that in vacuum [85].

In this dissertation, three PIC codes were used. Studies of DLA in Chapter IV were conducted using the EPOCH code [86], OSIRIS 4.0 [87, 88] was used to study long wavelength generation during LWFA in Chapter V and SCPIC [89] was used to investigate backward SRS in Chapter VI. Although there are differences between each of these PIC codes, the utilization of different codes is based more on accessibility of the code to the user rather than virtue of the code or solver; EPOCH simulations were performed by the author, while OSIRIS and SCPIC simulations were run by collaborators at the University of Alberta.

LWFA simulations in Chapters VI and V were conducted using a moving box reference frame that was co-propagating with the laser pulse. Moving box simulations provide the highest efficiency in resolving pulse propagating and the response of surrounding plasma over long propagation distances. In this frame of reference ions are treated as stationary, which is a reasonable assumption for the pulse duration used in these studies. For simulations of picosecond laser-plasma interaction, required in Chapter IV, a millimeter scale plasma was simulated using a stationary box and ions were considered mobile to investigate the effect of ion motion on channel formation

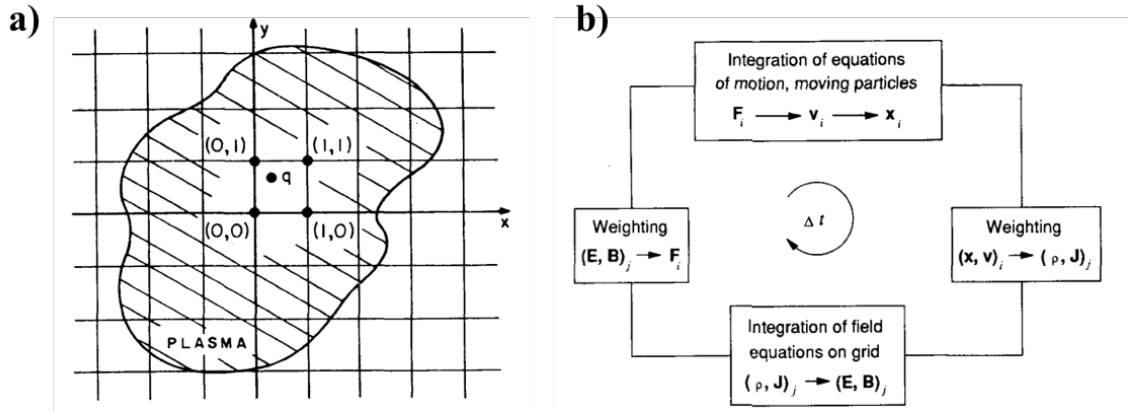

Figure 3.8: **a)** Illustration of the mathematical grid set into the plasma. A charged particle q on the grid will be counted as a current density on nearby grid points. **b** Typical computing sequence of the PIC Method. Figure from Ref. [90], © 1991 IEEE

and electron acceleration *via* DLA.

CHAPTER IV

Optimizing direct laser acceleration

4.1 Introduction

For high-intensity, sustained laser-plasma interactions the laser pulse will ponderomotively expel nearly all of the electrons within its focal volume in the plasma creating a positively charged channel. This channel evolves on the ion timescale and therefore is considered quasi-static relative to the timescale of electron motion. Electrons that become trapped in the ion channel can gain longitudinal momentum from the laser field through the $v \times B$ force in the Lorentz force equation [34, 35, 36]. This is known as Direct Laser Acceleration (DLA). DLA can be used to produce high charge electron beams ($\sim$ 100s of nanocoulomb [29, 37, 38]), relevant to a variety of applications, including the generation of hard X-ray beams for probing dense plasmas [44] and the production of electron-positron beams [40].

DLA is very complex due to the interplay of electrostatic fields in the evolving plasma channel and the oscillating electric fields of the driving laser pulse [35, 70, 38, 71]. There are several mechanisms that can contribute to electron energy gain

during DLA. For example, transverse electron oscillations may lead to a resonance between electrons and the driving laser pulse, enhancing electron energy gain [35, 70, 71]. Betatron oscillations due to the magnetic field of moving electrons may also reduce the dephasing rate between the laser field and accelerated electrons [35]. A longitudinal electric field directed in opposition to the laser field can slow down electrons with superluminal velocities, keeping them in phase with the laser pulse for longer periods [67, 68, 73, 72], and even a small difference between the phase velocity of the wave and the speed of light can alter electron dynamics during DLA [74]. Electrons may also gain energy stochastically through perturbations to the electron trajectory [37, 75].

Previous experimental and computational work has investigated DLA using pulse durations exceeding the plasma period. Experiments by Gahn et al. [36] produced multi-MeV electron beams using 200 fs pulses in high-density plasma channels [36]. In this work, longitudinal plasma waves were found to decelerate electrons, confirming DLA as the dominant mechanism. In later experiments by Mangles et al., [37], electron beams in excess of 300 MeV were produced independently of plasma wave generation, indicating that high energy electron beams can be accelerated directly by the laser field through interaction with the nonlinear focusing force of the plasma channel. Experiments by Willingale et al. [38] investigated the effects of laser power and pulse duration on DLA, and observed the formation of surface waves on the walls of the plasma channel that may be linked to electron injection and generation of high-charge electron beams *via* DLA. Recently, DLA in solids has been shown by Ma et al. [91] to produce highly collimated electron beams with 100 nanocoulomb (nC) charge. DLA can also play a significant role in LWFA, as shown by Shaw et al. [66].

Previous work highlights the capability of high-intensity ps pulses for the generation of high-energy, high-charge electron beams *via* DLA. Fits to numerical models have suggested scaling of electron energy with laser intensity, channel length and interaction time [35, 75], and threshold channel densities have been postulated from numerical simulations [71], however a theoretical interpretation of the scaling of the DLA electron energy as a function of plasma density has not yet been developed. Elucidating the dynamics of electron heating and acceleration as a function of plasma density for specific conditions would enable optimized production of high-quality electron beams.

In this chapter, experiments on electron acceleration *via* DLA using the OMEGA EP laser system are presented. These results demonstrate the existence of an optimal plasma density for electron acceleration by DLA, producing electron beams with energies up to 600 MeV and 10s of nanocoulomb charge. Two-dimensional PIC simulations matching the experimental conditions confirm DLA as the dominant acceleration mechanism. Simulations also demonstrate the importance of quasi-static channel fields in enhanced electron acceleration and give insight into the role of relativistic self-focusing and growth of the filamentation instability on channel formation and optimized acceleration. Increased pulse duration in PIC simulations was also found to enhance the charge of DLA electron beams.

4.2 Experimental setup

Experiments were performed at the OMEGA EP laser system at the University of Rochester Laboratory for Laser Energetics. A schematic of the setup is given in Figure 4.1. A single long-pulse UV heater beam (2.5 ns, 1214.6 $\pm$ 15.6 J, 351 μm) with a 100 μm spot size and super-Gaussian spatial profile was used to create

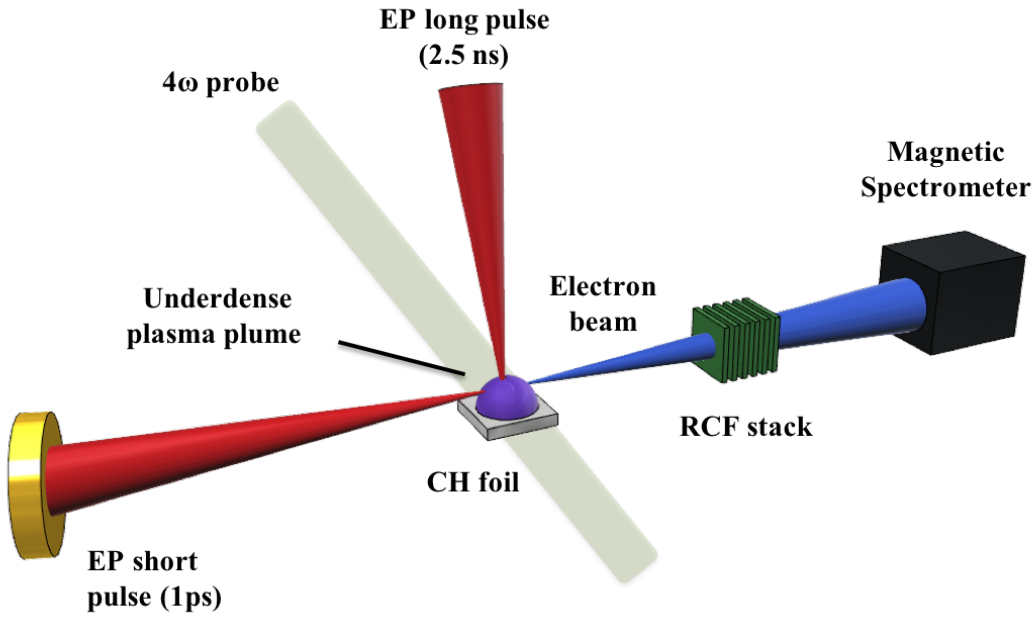

Figure 4.1: Schematic of the experimental configuration showing the generation of an underdense plasma plume using a long pulse heater beam, a 1 ps beam for electron acceleration, a 263 nm optical probe beam and the location of beam diagnostics.

an underdense plasma target through the ionization of a flat CH foil. The main interaction pulse ($\lambda = 1.053$ μm) had a full-width half-maximum (FWHM) pulse duration of 1 ps and an average energy of (414.6 ± 6.9) J. The 1 ps pulse was focused using an $f/2$ off-axis paraboloid, yielding a peak normalized intensity of $a_0 \simeq 5.5$. A stack of Radiochromic Film (RCF) for analysis of electron beam pointing and divergence was positioned on the axis of the 1 ps laser pulse at a distance of 8 cm from the main interaction. A hole in the center of the RCF stack allowed a direct line of sight of the electron beam on an absolutely calibrated magnetic spectrometer for measurements of the electron spectrum along the axis of the main interaction beam.

The plasma density was varied by changing the interaction height of the 1 ps laser pulse above the CH plame plume, within a range of 1.5 to 2 mm, or by changing the

timing between the ns pulse UV beam and the 1 ps interaction beams between (1.5 - 3.5) ns. The plasma density was measured by Angular Filter Refractrometry (AFR) [92]. In this way, the plasma density profile can be approximated as a Gaussian function in two dimensions. In these experiments, peak plasma densities ranging between $0.0095n_c$ – $0.11n_c$ were investigated, where $n_c = m_e\omega_0^2\epsilon_0/e^2$ is the critical plasma density. The experimentally determined plasma density profiles were in good agreement with results from the two-dimensional hydrodynamic code SAGE [93].

4.3 Particle-in-cell simulations

Two-dimensional Particle-in-Cell (PIC) simulations using the EPOCH code [94] were performed to examine a laser pulse at relativistic intensity interacting with a plasma of sub-critical density. The simulations were designed to match the conditions of the OMEGA EP laser system. A 1.053 μm wavelength Gaussian laser pulse with 1 ps FWHM duration was simulated using two co-incident focal spots to approximate the experimental energy distribution in the focal plane (spot sizes of 3.4 μm and 17 μm, corresponding to a normalized vector potential a_0 of 1.5 and 5.5 respectively). The plasma density profile was defined by the Gaussian profile from AFR measurements and was varied between $n_0 = 3.1 \times 10^{25}$ m^{-3} (0.005 n_c) and 6.5×10^{21} cm^{-3} (0.1 n_c). The quoted electron density for all simulations refers to the peak density encountered by the laser pulse along this trajectory.

The simulation box was (2200 $\times$ 200) μm, and simulations were performed with a resolution of 30 cells per λ in the longitudinal direction (x), and 6 cells per λ in the transverse direction (y). The laser was linearly polarized in y, propagated in x and entered the box at a height of $y = 1000$ μm. Fully ionized carbon ions were treated as mobile and open boundary conditions were employed. Channel formation and

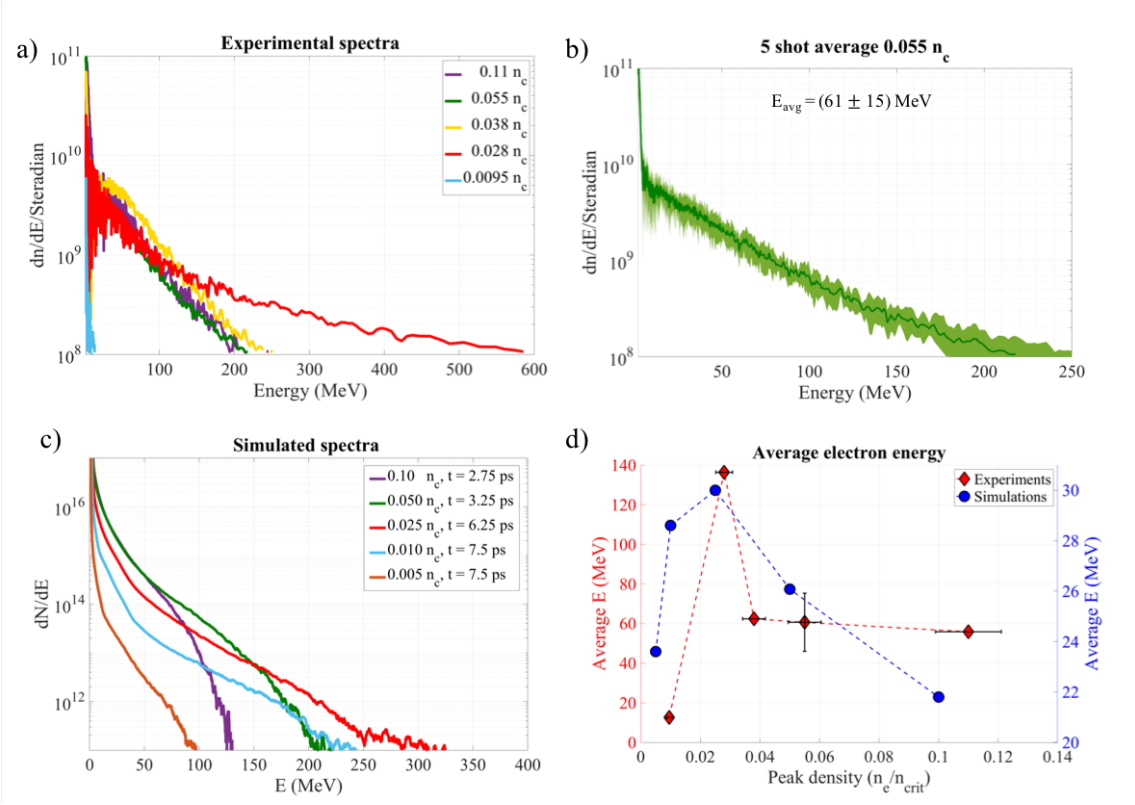

Figure 4.2: **a)** Experimental spectra of escaped electrons for different peak plasma densities, shown at the time at which electron energies were the highest. **b)** Shot-to-shot variation in measured electron spectrum over five shots obtained at an estimated peak plasma density of 0.055 n_c. **c)** Simulated electron spectra for different peak plasma densities. **d)** Comparison between experimental and simulated average electron temperatures showing good qualitative agreement (the left axis corresponds to experimental data).

electron distribution functions were investigated by simulating the interaction for 8 to 10 ps, with outputs every 250 fs. Subsequently, particle tracking was conducted for time intervals up to 4 ps, with outputs every 25 fs

4.4 Results and Analysis

4.4.1 Electron acceleration

Experimentally measured electron energy spectra from five different plasma densities are shown in Figure 4.2a). Acceleration of an electron beam with a Maxwellian distribution extending to 600 MeV is observed at a plasma density of 0.028 n_c, in-

dicating the existence of an optimal density for the generation of energetic electron beams. The shot-to-shot variation in electron spectra over five shots at identical experimental conditions and a plasma density of 0.055 n_c is plotted in as a shaded region Figure 4.2b), showing reasonably high reproducibility of the interaction.

2D PIC simulations also reproduced the existence of an optimal density at $0.025n_c$ for electron acceleration by a 1 ps FWHM pulse. Simulated spectra for densities between 0.005 n_c and 0.1 n_c are given in Figure 4.2c), where each spectrum is taken at the time when the highest energy electrons were present.

The average electron energy between 10 and 600 MeV is plotted for both simulations and experiments in Figure 4.2d. Experiments produced electron beams with a maximum average energy of 136 MeV at 0.028 n_c. For 0.055 n_c, the electron spectrum is averaged over data from five repeated shots, yielding an average energy of (61 ± 15) MeV, where the quoted error reflects the variation in the average electron energy. Good qualitative agreement is found between experiments and simulations, however in all cases the simulated electron energies are significantly lower. This is because the experimental spectra measure only the escaped electrons, while simulation include low energy bulk electrons, as can be observed from the low-energy tails in the simulated spectra in Figure 4.2c). The discrepancy in maximum electron energy between experiments and simulations is likely due to the failure to capture out-of-plane electron oscillations in 2D simulations, as will be further discussed.

4.4.2 Beam divergence, pointing and total charge

The stack of RCF along the axis of the ps pulse provides information about the beam pointing and divergence. In Figure 4.3a) the magnetic spectrometer is aligned to the laser axis behind the central hole in the RCF stack. At all densities, the electron beam is found to deflect upward, due to the refraction of the laser pulse in

the plasma gradient towards regions of lower density. At low density, the formation of multiple beams is observed. The simulated angular divergence of electron beams is plotted for three densities in Figure 4.3b). Simulations indicate that the highest energy electrons are collimated along the axis of the laser pulse at the optimal electron density, and breakup at low density is reproduced. The forking structure observed at low density has been correlated with a transverse modulation of the electron beam by DLA [95].

The presence of multiple beams at low density is due to the filamentation instability and ion motion which can seed hosing-type instabilities [96]. Refraction of the laser beam may be responsible for the apparent offset of the electron beam from the laser axis on RCF stack, indicating that the highest energy electrons may not be measured on the magnetic spectrometer. The upward refraction of the laser beam may be mitigated by using plasma targets with shallower density gradients, such as those generated using gas jets.

Gaussian fits to the electron beam profile on the RCF stack were used to determine the beam divergence as a function of density. The beam divergence, taken as the FWHM of a Gaussian fit in x and y, was found to decrease with decreasing plasma density, ranging from about 60 to 80 mrad, as shown in Figure 4.4a. At the lowest density, the formation of multiple beamlets are considered as a single beam for comparison. It is important to note, given the simulated angular divergence in Figure 4.3b, that the divergence of the highest energy electrons may be much smaller than the quoted divergence of the entire beam. This is supported by the angular distribution of the electron beam from simulations, as shown in Figure 4.3b.

The total charge within the electron beam is estimated by extrapolating the signal on the RCF stack to the total electron counts measured on the electron spectrometer.

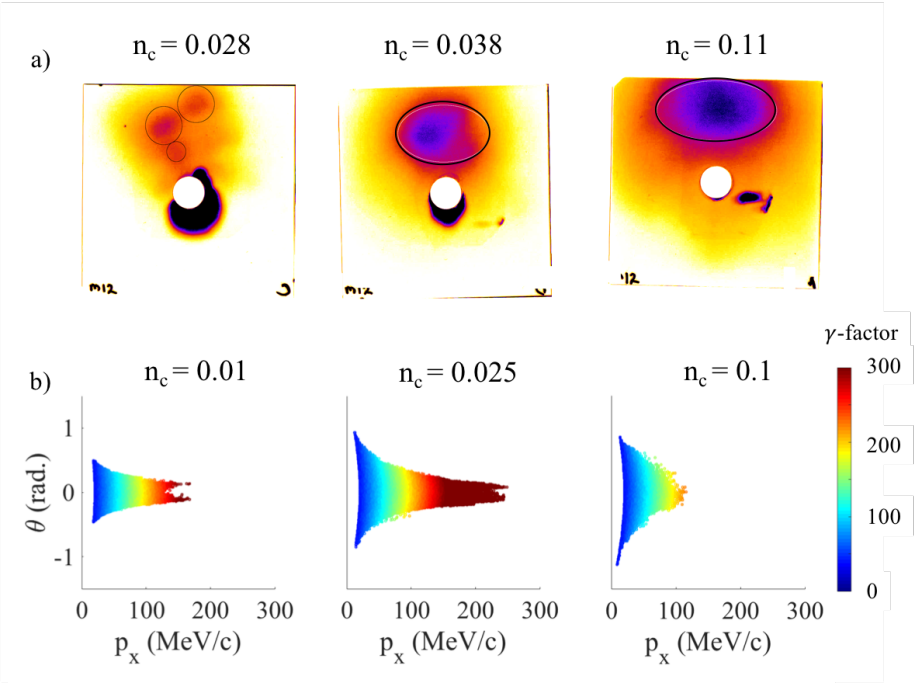

Figure 4.3: **a)** A stack of Radiochromic Film (RCF) along the axis of the laser beam serves as a diagnostic of beam pointing and divergence. The hole in the center of the RCF stack is aligned with the 1 ps main interaction beam. Raw RCF, presented on the same color scale, indicates increasing beam divergence with plasma density. At low density, the formation of multiple beamlets is observed. **b)** Angular divergence from 2D simulations at t = 5.75 ps shows similar trend in beam divergence as a function of plasma density.

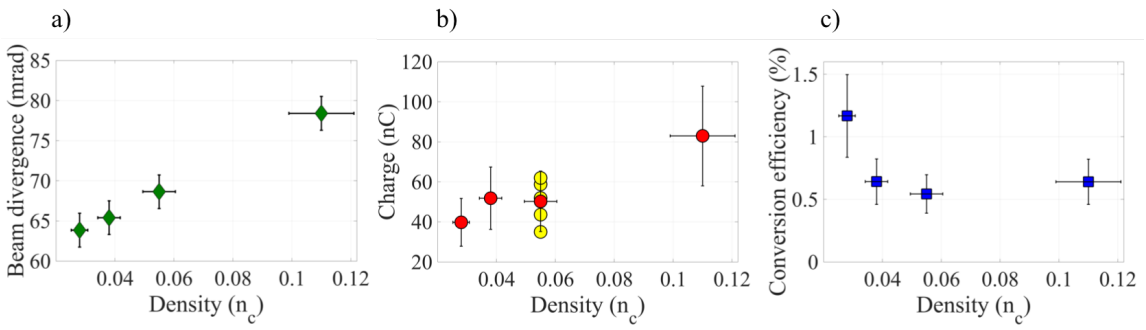

Figure 4.4: **a)** Beam divergence as a function of plasma density. **b)** Electron beam charge as a function of plasma density. Charge from five repeated shots at $n_e = 0.05 n_c$ is shown in yellow, from which error bars are determined. **c)** Conversion efficiency of laser power into electron beam energy. Estimates at the lowest density, 0.0095 n_c are not included due to insufficient signal on RCF.

At the lowest density (0.0095 n_c), there was insufficient signal on the RCF to make estimates. The approximated electron beam charge, which can be best interpreted as a lower-bound on the total beam charge due to large uncertainties in the measurement, is plotted as a function of plasma density in Figure 4.4b). Beams with charge in excess of 50 nC were obtained at the optimal plasma density, and charge increased with plasma density. The error bars on these measurements are determined by the five shot variation at 0.055 n_c.

At the highest plasma density investigated, 0.11 n_c, electron beams approaching 90 nC were accelerated, with an average electron energy of nearly 56 MeV, as shown in Figure 4.2c). The measured beam charge is lower than previous results [38], which may be due the presence of the RCF stack along the axis of the accelerated electron beam. The conversion efficiency as a function of density is also shown in Figure 4.4c), indicating highest efficiency of 1.2% at the optimal density.

4.4.3 Channel formation

The interplay between the laser field and electromagnetic fields of the quasi-static plasma channel is of central importance in the optimization of DLA. Two-dimensional

simulations elucidate laser propagation effects and the role of the quasi-static plasma channel on electron acceleration at different plasma densities. The plasma density affects the laser propagation due to a balance between laser self-focusing and instability growth. As the plasma density increases, the pulse will not propagate through the entire plasma due to the growth of the filamentation instability and the transverse beam break-up.

Snapshots of electron density are given in Figure 4.5a) at a simulation time of 5.75 ps for three different simulated densities. The channel is unstable and filamented at the highest density, 0.1 n_c. At the lowest plasma density, 0.01 n_c, a stable channel is observed, but was associated with poor electron acceleration (c.f. Figure 4.2c)). At the optimal density, 0.025 n_c, the channel extends the length of the plasma and oscillating structures along the walls of the channel are observed. These surface wave structures likely play a role in electron injection during DLA [97, 98, 38]. The laser field is superimposed in yellow to illustrate the location of the laser pulse in the plasma channel. The laser pulse is found to be significantly depleted at the highest plasma density.

The density of carbon ions, normalized to the critical density, is plotted in Figure 4.5b). Relative to the superimposed laser field in 4.5 a), ion motion lags behind the trailing edge of the laser pulse. Ion motion is most significant at the lowest density (0.01 n_c), and negligible at the highest density. At 0.025 n_c, the ion channel cavitates along two forked trajectories due to the location of highest energy electrons at the edge of the plasma channel.

The average transverse field, E_y, which captures the channel field, is normalized to the vacuum maximum amplitude of the laser field, denoted E_{max}, and shown in Figure 4.5c). The core of the channel is positively charged due to electron depletion

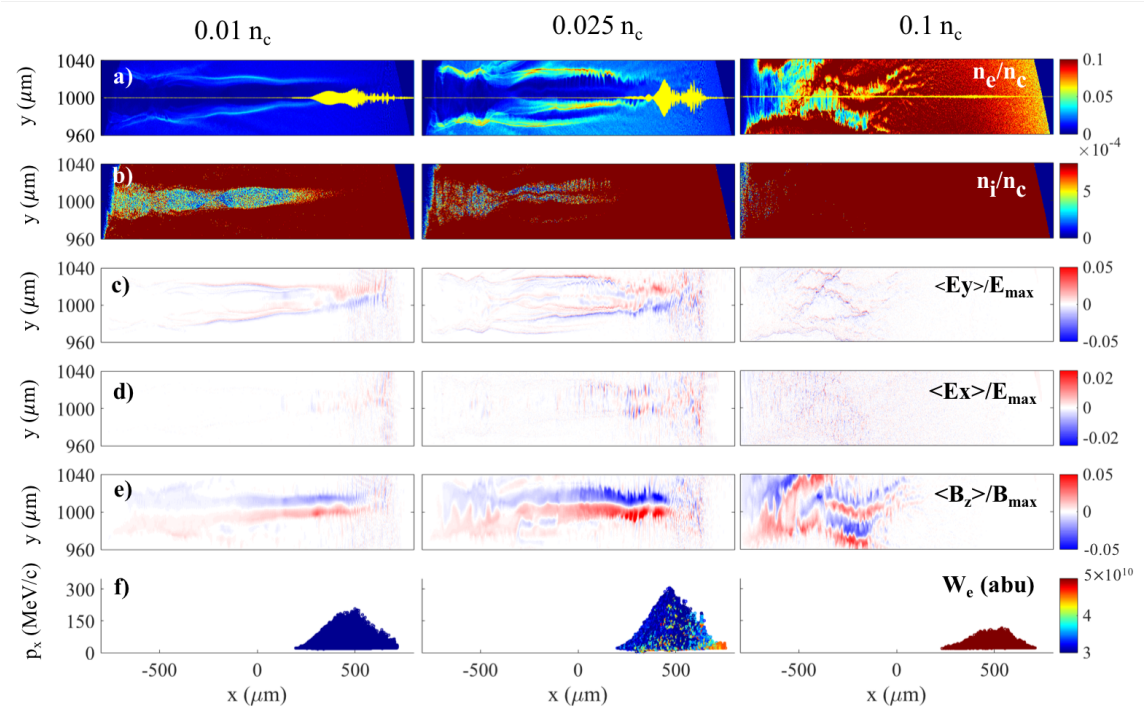

Figure 4.5: Simulations of a 1 ps FWHM laser pulse propagating into plasma of various density give insight into the role of the plasma channel on electron acceleration. All images are taken at a simulation time of 5.75 ps, and all averaging is done over 5 laser periods. The electron density, normalized to the critical plasma density, is plotted in **a)**. The laser field, E_y, normalized to the field amplitude of a laser with $a_0 = 5.5$, is overlaid in yellow in **a**, where the limits of the plot (not shown) are between -1 and 1. **b)** The carbon density normalized to the critical density, demonstrates ion mobility and channel cavitation. The average transverse electric field, E_y, longitudinal electric field E_x, and the transverse magnetic field, B_z, all normalized amplitude of the the laser field, are plotted in **c)**, **d)** and **e)**, respectively. The longitudinal momentum, p_x, for individual electron pseudoparticles with a γ-factor greater than 40 ($\sim$ 20 MeV), are plotted in **f)**, where the color-scale indicates the total number of electrons.

while the outer boundaries are negatively charged. Duplicate channel structures may indicate shock formation, and is the focus of other work [99]. At the highest density the channel is highly disrupted, indicating instabilities in laser propagation. There is also a reversal in the transverse channel fields, particularly visible for the $0.01n_c$ and $0.025n_c$ simulations, associated with the ion motion [100]. Despite the fact that these fields are relatively weak, not exceeding about a percent of the laser field, they have been shown to significantly enhance electron energy gain [73], as will be further discussed.

The longitudinal electric field, E_x, normalized to the laser field, is plotted in Figure 4.5d). The color-scale in this plot is lower than for the other fields due to the relative weakness of longitudinal channel fields. It has been previously shown that a significant negative electric field at the channel entrance can launch an electron into an energetic trajectory by decreasing its dephasing rate with the laser field [67]. E_x fields coinciding with density perturbations in Figure 4.5a) may be indicative of electron injection into the plasma channel by surface wave structures.

The time-averaged perpendicular normalized magnetic field, B_z, is plotted in Figure 4.5e). The transverse magnetic field, which is higher at 0.025 n_c than at the lowest density, might play a role in enhancing electron oscillations within the channel [68]. Strong magnetic fields are also generated by the current of energetic electrons; electron acceleration and magnetic field strength may be a positive feedback system for energy gain. Bumps and disruptions in the magnetic field can be observed at both 0.025 n_c and 0.1 n_c, corresponding with electron density perturbations in Figure 4.5a) and may be caused by the motion of energetic electrons into the plasma channel.

The location and longitudinal momentum of electrons with γ-factors exceeding

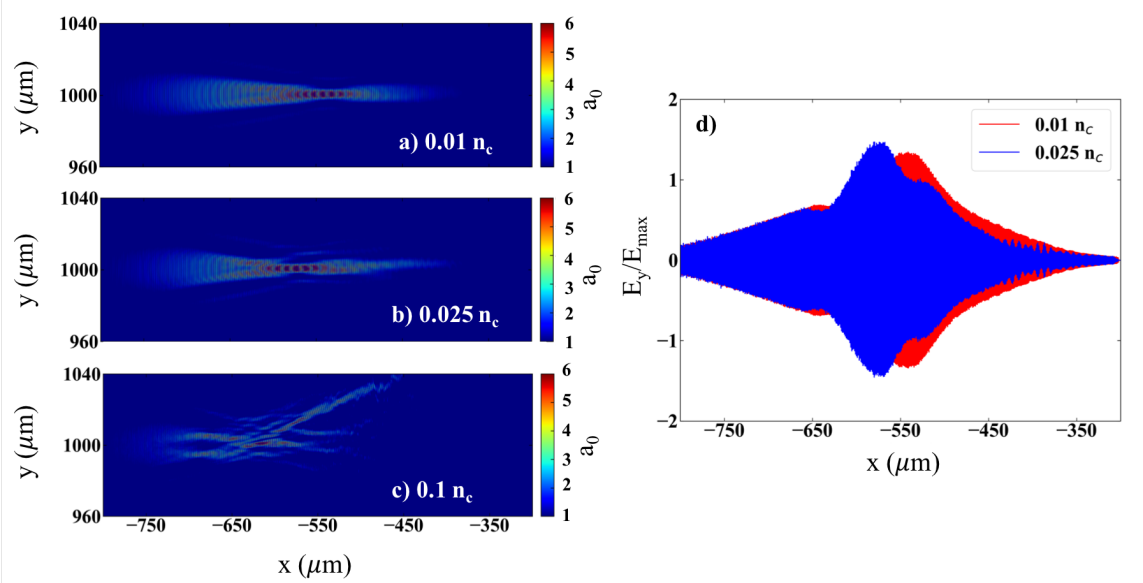

Figure 4.6: Propagation of the laser pulse with normalized vector potential $a_0 = 5.5$ into underdense plasma, plotted at 2 ps into the interaction time. **a)** At 0.01 n_c the laser self-focuses, but no filamentation is observed. **b)** at 0.025 n_c, weak disruption of the laser pulse into small filaments occurs. **c)** The laser beam is highly filamented and broken up at 0.01 n_c. **d)** The laser envelope is compared at the two lowest densities, indicating slight enhancement of the laser-field following relativistic self-focusing at 0.025 n_c.

40 ($\sim$ 20 MeV) are shown in Figure 4.5f), where $\gamma = \sqrt{1 + p^2/m_e^2c^2}$. The maximum longitudinal momentum is achieved at the optimal density, while the largest number of electrons are accelerated at the highest density. Relative to the laser pulse plotted in the overlay of Figure 4.5a), the highest energy electrons trail the leading edge of the pulse, but no electrons with energy above $\gamma = 40$ are observed behind the laser pulse. No spatial modulation or bunching of the electron beam is observed, as might be expected with SM-LWFA, where the plasma density is modulated at the plasma frequency.

Simulation results indicate that the formation of a plasma channel with sufficiently strong quasi-static fields for enhanced acceleration is a propagation effect resulting from a balance between relativistic and ponderomotive self-focusing and the filamentation instability. Self-focusing and filamentation of the laser beam are shown

at each density in Figure 4.6, plotted at 2 ps into the interaction time. The beam strongly filaments and breaks up at 0.1 n_c, while channel formation is regular and negligible modulations of the laser profile are observed 0.01 n_c. At 0.025 n_c, moderate filamentation of the laser pulse occurs with self focusing. Additionally, at this density, the amplitude of the laser pulse is slightly enhanced relative to the lowest density (Figure 4.6d)).

4.4.4 The role of quasi-static fields

To understand the role of the transverse electric field on enhanced electron acceleration in a quasi-static channel, Arefiev et al. [73] have modeled the equation of motion of an electron across the channel as a driven oscillator:

$$\frac{d^2y}{d\tau^2} + \Omega^2 y = c\frac{da}{d\tau} \tag{4.1}$$

where $\Omega = \sqrt{\gamma/2}\omega_{pe}$, a is the amplitude of the laser wave, and τ is the timescale over which the wave phase changes at the electron location (defined by $\frac{d\tau}{dt} = \frac{1}{\gamma}$).

Electron motion in the channel is subject to two characteristic frequencies: (1) the frequency of oscillations under the action of the laser field (ω_0), and (2) the natural frequency of oscillations induced by the field of the quasi-static channel (Ω). In the vacuum limit $\Omega \ll \omega_0$ and the laser frequency ω_0 dominates, therefore the maximum electron energy gain is expected to follow the ponderomotive vacuum limit (yielding $\gamma \simeq 16$ for an $a_0 = 5.5$). However, as the plasma density increases $\Omega \simeq \omega_0$ causing the amplitude of electron oscillations to grow. Enhanced transverse oscillations of the electron in the channel can allow the electron to remain in phase with the laser field over a prolonged period, drastically enhancing the net energy gain of the electron [71]. In this way, the quasi-static fields of the steady-state channel can play a significant role in in electron dynamics and acceleration.

A dimensionless parameter to define the threshold for enhancement of electron energy can be defined [70, 71, 73]:

$$G \equiv a_0 \frac{\omega_{pe}}{\omega_0} \tag{4.2}$$

yielding a sharp threshold in optimal acceleration as a function of a_0 and ω_{pe}/ω_0. Arefiev et al. [73] theorize that optimal electron acceleration should occur for $G = 1$. The work presented here is in good agreement with this theoretical estimate. From simulations, at the optimal plasma density $n_e = 0.025 n_c$ with $a_0 = 7.0$, the G value is 1.1. Experimentally, the optimal density was $n_e = 0.025 n_c$ with $a_0 = 5.5$, yielding $G = 0.92$. Discrepancies between theoretical estimates and the experimental and simulation work presented here may arise from inclusion of experimental artifacts (anomalies in the focal spot, density gradients, etc.), as well as the failure to fully capture filamentation and self-focusing phenomena in 2D. It is also important to note that experimental measurements capture the properties of electrons that exit the plasma, while the above theory captures the acceleration of an electron under fixed conditions. Later in time, electrons may lose energy following beam breakup, or as they escape the channel or dephase from the laser field by becoming superluminal [74].

4.4.5 Electron motion and acceleration mechanisms

Particle tracking elucidates the dynamics of individual electrons during the acceleration process and under the action of the laser and quasi-static channel fields. The momentum gain of individual particles between 2 - 4.25 ps is plotted in Figure 4.7a), and the trajectories typical of highest energy electrons are shown in Figure 4.7b). At the optimal density, electrons begin their trajectory at 2 ps with relatively high energy, and undergo clear periodic oscillations under the action of the laser

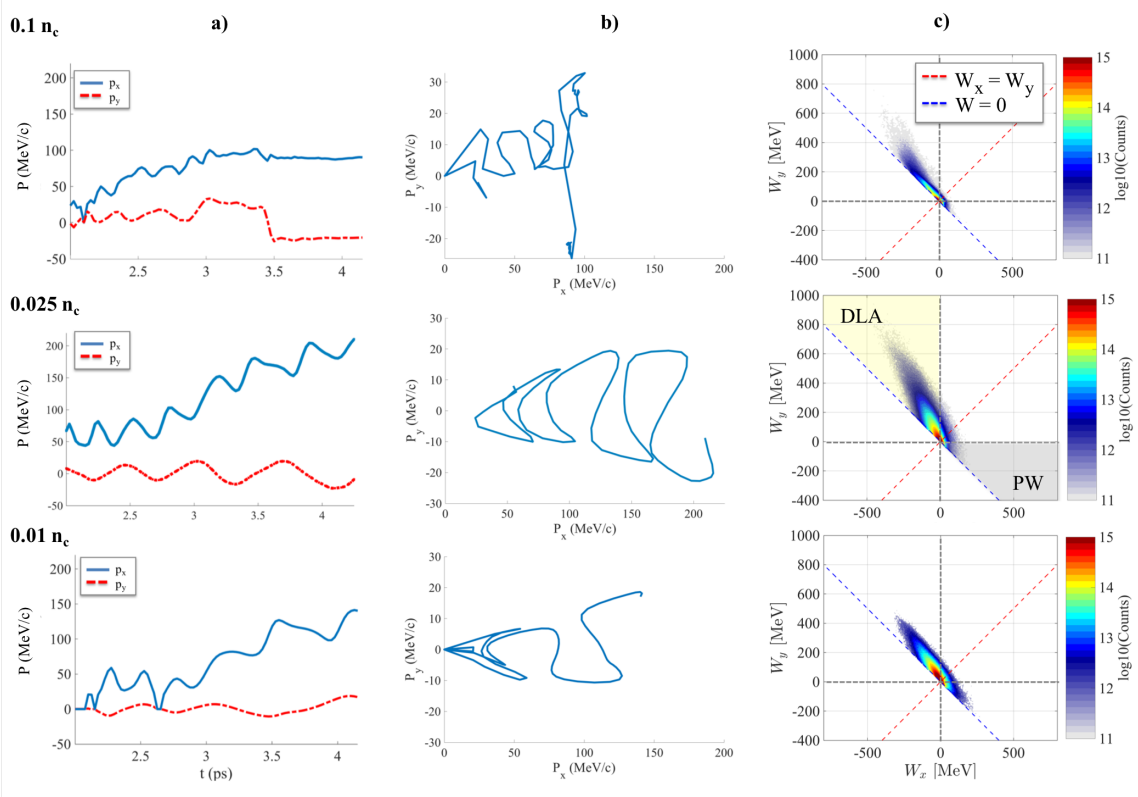

Figure 4.7: Trajectories of randomly selected electrons at the highest energies for three densities. **a)** Evolution of the longitudinal (p_x) and transverse (p_y) momenta are plotted as a function of time between 2 to 4.25 ps. **b)** The phase space p_x-p_y is plotted in the right column for the same particles over the same time period. **c)** The components of energy gain in (W_x,W_y) space at the time of optimal acceleration for each investigated density with a pulse duration of $t_p = 1$ ps. The energy gain space is shown at the time yielding highest energy electrons for each density: t = 2.75 ps for 0.1 n_c, t = 6.25 ps for 0.025 n_c, and t = 7.5 ps for 0.01 n_c. The red dashed line divides the space into two regions: DLA-dominated region in the upper left and plasma-wave (PW) dominated acceleration-dominated region in the lower right.

and quasi-static channel fields, gaining energy with each cycle. For these electrons, the longitudinal momentum is twice that of the transverse momentum, indicating electron follow the "figure-8" motion characteristic of the $v \times B$ force [91].

At high density, electrons likely gain energy by stochastic processes associated with self-focusing and growth of the filamentation instability, then dephase from the laser, limiting acceleration and resulting in chaotic electron trajectories [67, 68, 91]. Alternatively, at the lowest densities, electron receive reduced pre-acceleration from self-focusing and are subject to weaker quasi-static channel fields, resulting in poor electron energy gain.

The dominant acceleration mechanism can be determined by considering the contributions to electron energy gain from the transverse, E_y, and longitudinal, E_x electric fields, where E_x is associated with indirect acceleration of electrons due to plasma wave formation, and E_y is associated with direct acceleration by the laser field. By calculating the work done by each field the dominant acceleration mechanism can be determined. The electron distribution in energy gain space, (W_x, W_y), is plotted in Figure 4.7c) at the time yielding the highest energy electrons at each density (t = 2.75 ps for 0.1 n_c, t = 6.25 ps for 0.025 n_c, and t = 7.5 ps for 0.01 n_c). In all cases, the majority of electrons populate the region where $W_y > W_x$, indicating that DLA is the dominant acceleration mechanism.

The role of E_y in electron energy gain is most pronounced at the optimal density, 0.025 n_c, consistent with the oscillatory behavior of high energy electrons in Figure 4.7b). The considerable acceleration and deceleration of electrons indicates that this process can be an efficient X-ray source. Previous work has indicated that DLA produces higher amplitude betatron oscillations than achieved in the wakefield regime, enabling X-ray sources with much higher energies [39]. The characterization

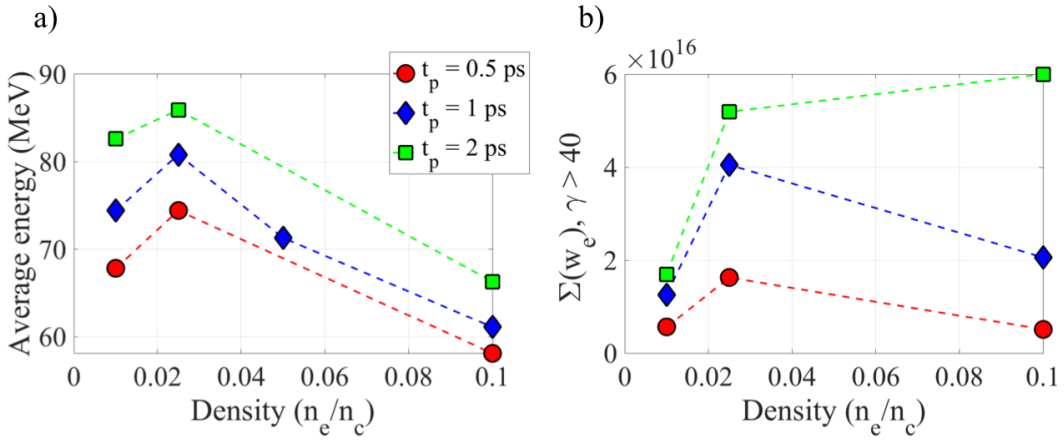

Figure 4.8: Effect of pulse duration on average electron energy in 2D PIC simulations. **a)** The optimal electron density is consistent at all pulse lengths, while the average energy increases with pulse duration. **b)** The sum of the particle weight for electrons with $\gamma > 40$.

of resultant X-ray emission is the topic of future work.

The discrepancy in average electron energies between experiments and simulations (Figure 4.2d), wherein 2D simulations under-estimate the maximum electron energy, can be attributed to the failure to capture free electron oscillations in the third dimension. It has been previously shown that electron oscillations in z can significantly enhance the natural driving frequency of electrons in the channel, leading to significant energy gain [70]. The failure to capture out-of-plane electron oscillations, and the subsequent effect on electron motion and energy gain, can explain the lower electron energies in 2D simulations.

4.4.6 Effect of pulse duration on electron acceleration

The effect of pulse duration on electron acceleration *via* DLA was explored in 2D EPOCH simulations. In this simulations, the peak a_0 was fixed, therefore the effective laser enregy was increased. The average electron energy as a function of plasma density for pulse duration of 0.5 ps, 1 ps and 2 ps are shown in Figure

4.8a). The optimal plasma density persists at each pulse duration, and a moderate enhancement of the average electron beam energy is observed.

The total charge in the electron beam can be approximated as the sum of electron weight. The total charge for all electrons with a γ-factor > 40 is given for each pulse duration and density in Figure 4.8b). The total charge in the electron beam can be considerably enhanced using a longer duration pulse. Note that the total beam charge does not increase with plasma density, as observed with experimental results (c.f. Figure 4.4b), because only particles above 20 MeV are considered from simulations.

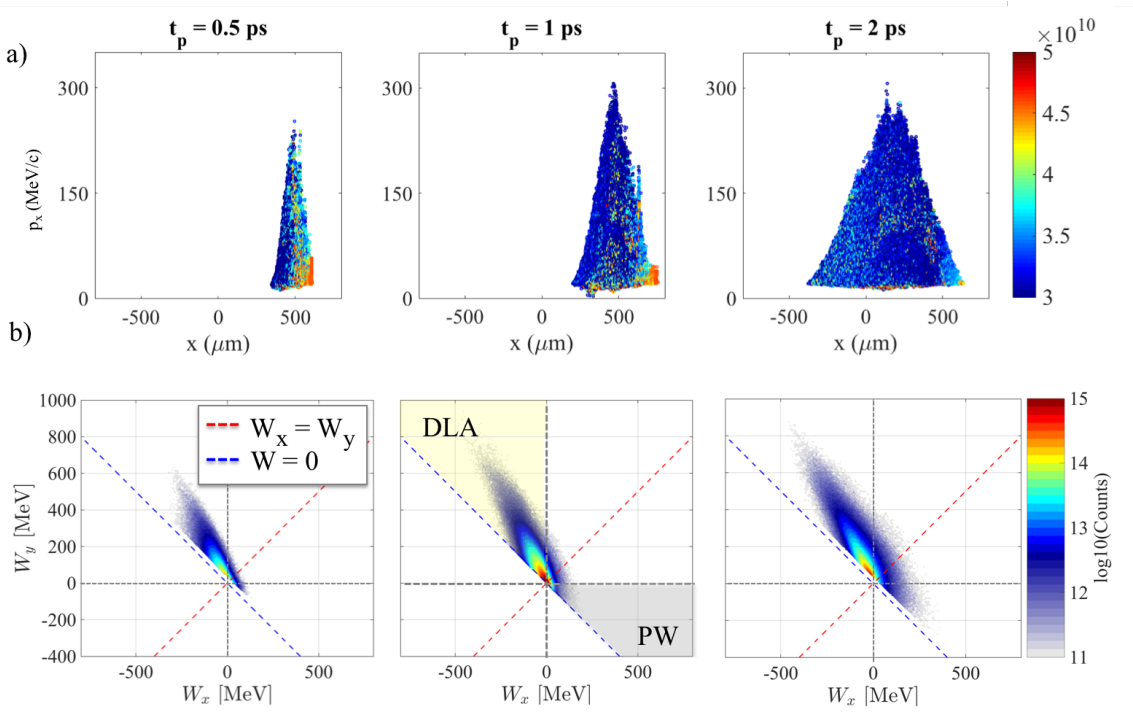

Figure 4.9: **a)** Longitudinal electron momentum as a function of location along the direction of laser propagation, with weight of the electron psuedoparticle in the colorscale (representing the total number of electrons) for electrons with a γ-factor of at least 40. High energy electrons are accelerated over the entirety of the laser pulse (150 μm for a 500 fs pulse, 300 μm for a 1 ps pulse, and 600 μm for a 2 ps pulse.) **b)** The work done by the transverse and longitudinal electric fields on high energy particles for each pulse duration indicates that DLA dominates for all pulse lengths.

The effect of pulse duration on electron beam charge can be further investigated by examining the longitudinal momentum of accelerated electrons versus the laser propagation axis, as shown for a fixed density of 0.025 n_c in Figure 4.9a). The location of energetic electrons demonstrates the enhancement of beam charge with longer pulse duration. This is because during DLA a separate bunch of electrons can be driven in each half-cycle of the laser field, and the total beam charge is proportional to the number of electron bunches within the plasma channel. For longer pulses, a greater portion of the laser field interacts with the plasma channel, and more electrons can be injected into the channel for acceleration. The energy gain of electrons in (W_x, W_y) space is given for each pulse duration in Figure 4.9b). It is clear that DLA is the dominant mechanism for all cases.

4.5 Conclusions

Experiments and 2D PIC simulations demonstrate an optimal electron density for DLA, resulting in measurements of electron beams with energies up to 600 MeV. The existence of a threshold density for a fixed a_0 was in good agreement with theoretical predictions. Simulation work reveals that stable channel formation results from a balance between self-focusing and filamentation, and that reduced surface wave formation at low densities may prevent pre-acceleration and injection of plasma electrons. The electron beam charge was measured to be on the order of 10s of nC, with electron beams approaching 90 nC with an average energy of nearly 56 MeV obtained at the highest density. Further investigations into the role of pulse duration on DLA using 2D PIC simulations indicate that the optimal density persists for pulses of 0.5 and 2 ps duration, but that the populations of energetic electrons can be significantly enhanced by using longer pulses.

This demonstration of high energy, high charge electron beams using picosecond petawatt-class laser systems could enable new applications such as positron production through the interaction of energetic electrons with a high-intensity laser pulse [41], or experimental verification of the two-photon Breit-Wheeler process [42]. Finally, investigations into the motion of energetic electrons indicate that DLA produces bright X-ray sources with ultrashort duration with the capability to be accurately synchronized to short pulse laser-initiated events. These sources could be used to probe the dynamics of dense plasmas relevant to inertial confinement fusion and the characterization of high-energy-density-physics experiments [44].

CHAPTER V

Spectral measurements of mid-infrared radiation from a laser wakefield accelerator

5.1 Introduction

The mid-infrared (mid-IR) spectral region, spanning 2 - 20 μm, contains the frequency range of molecular vibrations and therefore is of significant interest for a diversity of scientific and technological applications [101, 102]. Ultra-short mid-IR pulses with intensities exceeding 10^{14} W/cm^2 have exciting applications in new frontiers, from mode-selective photochemistry [103] to driving attosecond, phase-matched high-order harmonics in the X-ray regime [104]. Additionally, for long wavelengths the critical power for self-focusing is reduced, and the critical density reduced, making LWFA driven with long-wavelength pulses an exciting opportunity for the generation of MeV-scale electron beams at moderate laser intensity [105, 106].

The development of ultra-short duration mid-IR sources optimized for power, efficiency and spectral performance is particularly challenging [107, 108]. Nonlinear photonics, fiber lasers and frequency combs are some approaches that have yielded

mid-IR sources with sub-picosecond duration [109, 102, 107], and high-intensity, short-pulse mid-IR sources are typically produced using optical parametric amplifiers pumped by 1 μm lasers. However, the production of wavelengths extending beyond 5 μm is limited by the suitability of nonlinear crystals [108], and for conventional nonlinear optical methods the total energy of mid-IR sources is limited by material damage or instabilities arising from nonlinear beam propagation, as well as the availability of suitable materials.

The use of a plasma medium to generate long wavelengths through non-linear self-phase modulation would mitigate challenges posed by optical damage. In a plasma medium the generation of laser driven plasma waves also produces frequency shifts in laser pulses [51, 47, 52, 46]. This is because the formation of the plasma wake (density perturbation) results in a refractive index gradient that is co-moving with the driving laser pulse. For relativistic laser intensities ($a_0 > 1$), the refractive index seen by the laser is:

$$\eta \simeq 1 - \frac{\omega_{pe}}{2\omega_0} \tag{5.1}$$

where ω_{pe} is the plasma frequency, ω_0 is the laser frequency. A gradient in η due to density gradients in the plasma will lead to an increase and/or decrease of the laser photon frequency.

A schematic for this process during LWFA in the bubble regime is given in the rest-frame of the laser pulse, $\eta = z - ct$ in Figure 5.1, where the laser electric field (blue) is super imposed on the electron density profile (red). In the bubble wave, a density up-ramp at the leading edge of the plasma bubble (5.1a) creates a region of negative gradient in the refractive index, causing a frequency downshift (red-shift) of the laser pulse. Photons at the tail of the wake (5.1a) experience a positive refractive index gradient, and therefore are frequency up-shifted. In this way, the

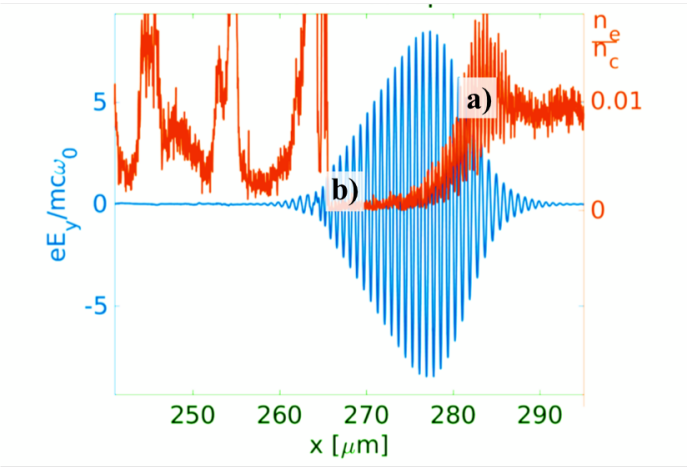

Figure 5.1: The laser field (blue) and the plasma density (red) obtained during LWFA in the bubble regime, presented in the rest frame of the laser pulse. **a)** At the leading edge of the wakefield bubble the laser will encounter a density up-ramp and a negative refractive index gradient, resulting in red-shifting of the pulse to longer wavelengths. **b)** The trailing edge of the laser pulse resides in a density down-ramp and a positive refractive index gradient.

pulse develops a positive frequency chirp, and a negative group velocity resulting in pulse compression [46]. At the center of the wake which consists of plasma ions, photons will experience negligible frequency variation. Given that the pulse duration is on the order of the plasma wavelength during LWFA, the body of the pulse will reside in a region of falling electron density, and red-shifting (photon deacceleration) will dominate the spectral evolution, producing wavelengths extending into the mid-IR. Additionally, the pulse duration will be compressed by the local reduction in group velocity associated with red-shifting of the spectrum.

Previous studies have explored the production of pulsed mid-infrared radiation due to spectral broadening during LWFA. Simulations by Zhu et al. [110] investigated the parametric dependence of mid-IR wavelength generation from a 30 fs duration intense laser pulse ($a_0 = 0.45$) traveling through under-dense plasma, finding that the efficiency of mid-IR production increased with the ponderomotive force and plateaued after complete blowout of the plasma wave was achieved. Pai et al. [107] measured

mid-IR radiation with energy up to 3.5 mJ produced using a 10 TW, 45 fs laser pulse, and found that long wavelength generation was correlated with electron acceleration by LWFA in the bubble regime. Additionally, recent computational work by Nie et al. [108] has demonstrated that tunable pulses with wavelengths extending to 14 μm may be achieved using tailored density plasma targets.

Experiments performed using the HERCULES laser system at the University of Michigan were conducted to measure the spectrum, energy and beam profile of mid-IR radiation produced during LWFA. Spectral measurements of wavelengths extending to 2.5 μm demonstrate the effect of laser power, pulse duration and chirp, plasma length and plasma density on spectral features. Two-stage tailored density targets were found to enhance the generation of long wavelengths. The spectrum of produced radiation was found to be highly dependent on laser and plasma conditions, with the highest variability in long wavelength production due to laser power and plasma length.

5.2 Experimental setup

Experiments were conducted using the HERCULES Ti:sapphire laser system at the University of Michigan. The 30 fs laser beam was focused using an f/20 parabolic mirror to a focal spot of $\simeq 10$ μm, achieving an intensities up to 4.8×10^{19} W/cm^2 ($a_0 \simeq 4.7$). Two types of gas cells were used to produce low-density plasma targets: a (5-20) mm variable length cell, and a (5-20) mm two-stage gas cell with a 1 mm rear compartment. Plasma density was controlled by altering the pressure of the gas supply, containing 98% helium and 2% nitrogen mixed gas. As an electron energy spectrometer, a 0.8 T magnet was used to disperse the electron beam onto a scintillating LANEX screen, from which the electron beam was imaged using a

CCD camera. For two-stage gas cells, each cell compartment was connected to an independent gas source. Density measurements were made using a shearing Michelson interferometer, yielding maximum plasma densities up to 1.3×10^{19} cm^{-3} in the main stage. Direct measurements of the plasma density were only made from the large chamber of the two-stage cells. The density in the second stage cell of 1 mm length was estimated by scaling interferometry measurements by the ratio of the volumes between the stages using the ideal gas equation. Taking into account the fill tube for the second stage and the variable length wall in the main stage, the rear stage density is estimated to be a factor of 4 $\times$ greater than the first stage. The maximum density in the short rear stage was estimated to be 4.4×10^{19} cm^{-3}.

Measurements of long-wavelength radiation produced by the interaction of the intense laser pulse with the plasma target were made in two experimental configurations, shown in Figure 5.2. In both setups, measurements of long wavelength radiation were made using a NIRQuest512-2.5 spectrometer with a range of 900 to 2500 nm (75 lines/mm grating and a 25 μm entrance slit). A 1 ms integration time was used for all measurements. Wavelengths below 1050 nm were filtered out near the entrance to the spectrometer using a 1 μm long pass filter (25.4 mm diameter); the filter was placed as far from the focus as possible, such that the intensity in the beam was below the damage threshold of the filter. The energy of the long wavelength pulse was measured using a pyrometric detector with a 2 mm diameter aperture.

In Setup 1, light exiting the gas cell was filtered through a 50.8 mm diameter 1050 nm long pass filter at a distance of approximately 0.5 m from the exit of the gas cell, before exiting the chamber through a 50.8 mm diameter MgF_2 window (6 mm thickness). Light traveling to the spectrometer was then reflected from a fused silica

wedge at 45°, attenuating the signal to 0.6% (for p-polarized light). The total energy in the mid-IR pulse was measured using a Gentec-EO QS3-IL pyrometric detector, interchanged with the spectrometer. For beam profile measurements, a scattering screen was placed at the exit of the chamber window, and the beam was carried to the Xenics Onca-MWIR-InSb camera using a 76.2 mm diameter gold mirror. An additional 1 μm LP filter was used on the Xenics camera.

In Setup 2, radiation exiting the gas cell was reflected from a 3 degree silica wedge at 45°. Escaping light was then collimated to a beam size of 34 mm through a 50.8 mm diameter focal length lens (f = 68 cm). The light exited the vacuum chamber through the MgF_2 window and was focused through a 50.8 mm lens (f = 50 cm) to the spectrometer entrance through a 1 μm long-pass filter. Gold mirrors were used throughout the setup.

All presented spectra were background subtracted and corrected for losses due to all optical elements in the system, as well as the grating efficiency of the NIRQuest spectrometer. Thus, measured spectra are presented between (1 - 2.4) μm, accounting for significant losses at the longest and shortest wavelengths. It is important to note that the use of fused silica elements in Setup 2 limit reliable spectral analysis to below 2.6 μm. A low pass filter with a normalized passband frequency of 0.1 π was applied to all spectra to remove high frequency noise.

The pyrometric detector was calibrated as 3.35×10^5 V/J ($\pm$ 3.5 %) using a 7.25 μJ source. The quoted energy values are background subtracted and have been corrected for the solid angle and transmission through optical elements. Background subtraction was also performed on beam profile images. Beam profiles measurements were subsequently filtered using a median noise filter to remove fluctuations and account for shot-to-shot variation in the background intensity.

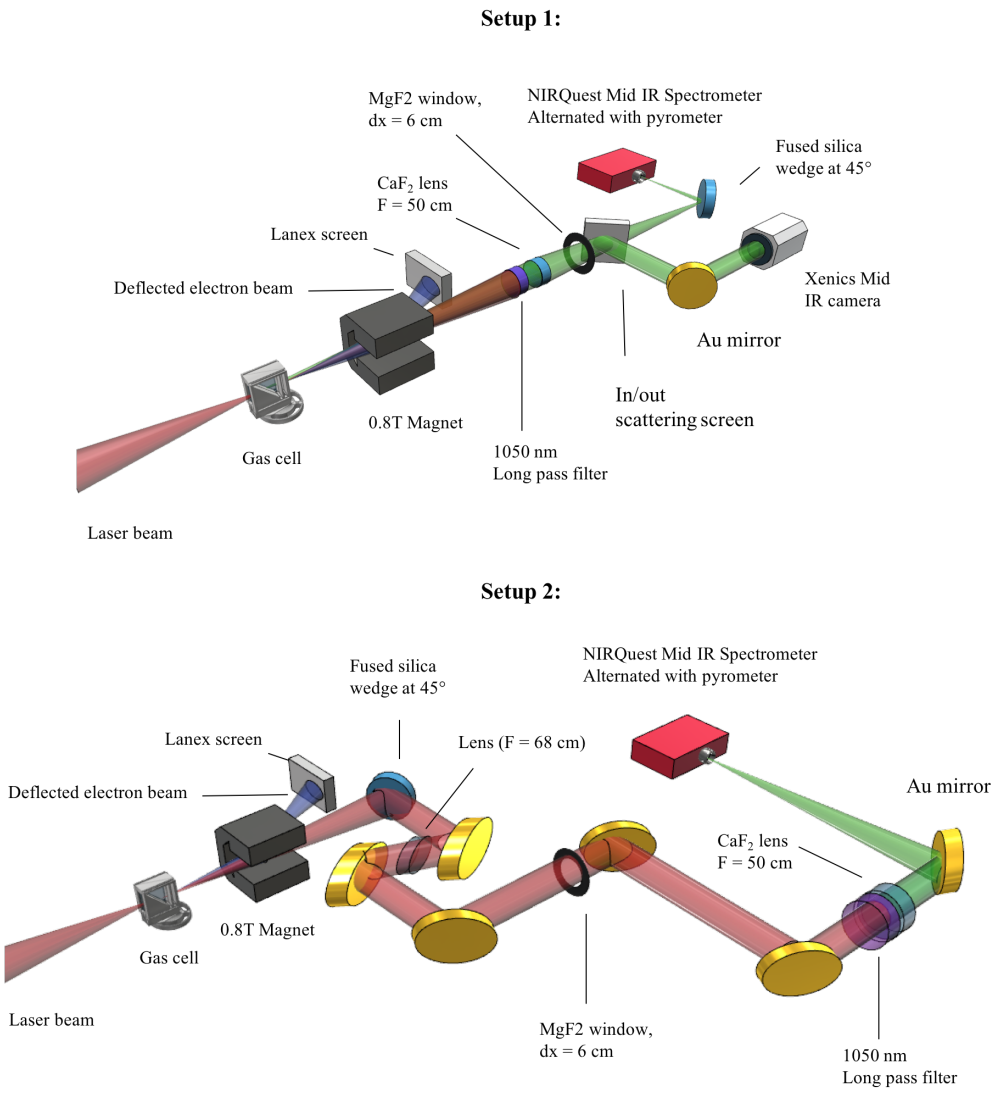

Figure 5.2: Experimental setup for measurement of transmitted mid-IR radiation during LWFA. A 30 fs laser pulse was focused into gas cell targets using an f/20 parabolic mirror. A 0.8 T magnet was used to disperse the electron beam onto a scintillating LANEX screen, from which the electron beam was imaged using a CCD camera. Density measurements were made using a shearing Michelson interferometer. Measurements of the mid-IR spectra were performed in two experimental configurations, Setup 1 and Setup 2. The energy contained in long-wavelength radiation was obtained using a pyrometric detector interchanged with the NIRQuest spectrometer. Beam profile measurements from a scattering screen were obtained using a Xenics midwave thermal infrared camera in Setup 1.

5.3 Experimental results and analysis

High resolution spectral measurements of long-wavelength radiation produced during LWFA experiments were obtained to study the variation in spectral features with plasma density, plasma length, and pulse duration and chirp. Discussion of mid-IR or long-wavelength radiation in this section refers to radiation with wavelengths extending beyond 1 μm.

5.3.1 Density tailoring

The implementation of a two-stage plasma cell with variable ratios of plasma density was found to produce longer wavelengths, extending to the detector limit (considered to be 2.4 μm after accounting for limits in the grating efficiency). The implementation of a two-stage, density step profile was motivated by recent computational work by Nie et al. [108]. In these simulations, tailored plasma profiles consisting of a long, low-density "compressor" stage, a short, high-density "converter" stage, and a rapid density down-ramp "coupler" stage were shown to produce tunable mid-IR radiation, extending to 14 μm.

In Figure 5.3, spectra are shown at varying plasma length obtained from single and two stage gas targets. The single stage was fixed at a density of 4.2×10^{18} cm^{-3}; the two stage gas cell has a density of 4.2×10^{18} cm^{-3} in the main (long) stage, while the secondary stage of 1 mm length was varied from 8.3×10^{18} cm^{-3} to 3.3×10^{19} cm^{-3}. Both spectra were obtained using Setup 2, but on different days. The average laser power for single stage experiment was (41 $\pm$ 2) TW with a plasma length of 5 mm, and two stage experiments were conducted at (49 $\pm$ 3) TW with a main stage length of 9 mm. All presented spectra are averaged from at least three shots at identical experimental conditions. The color scale shows the

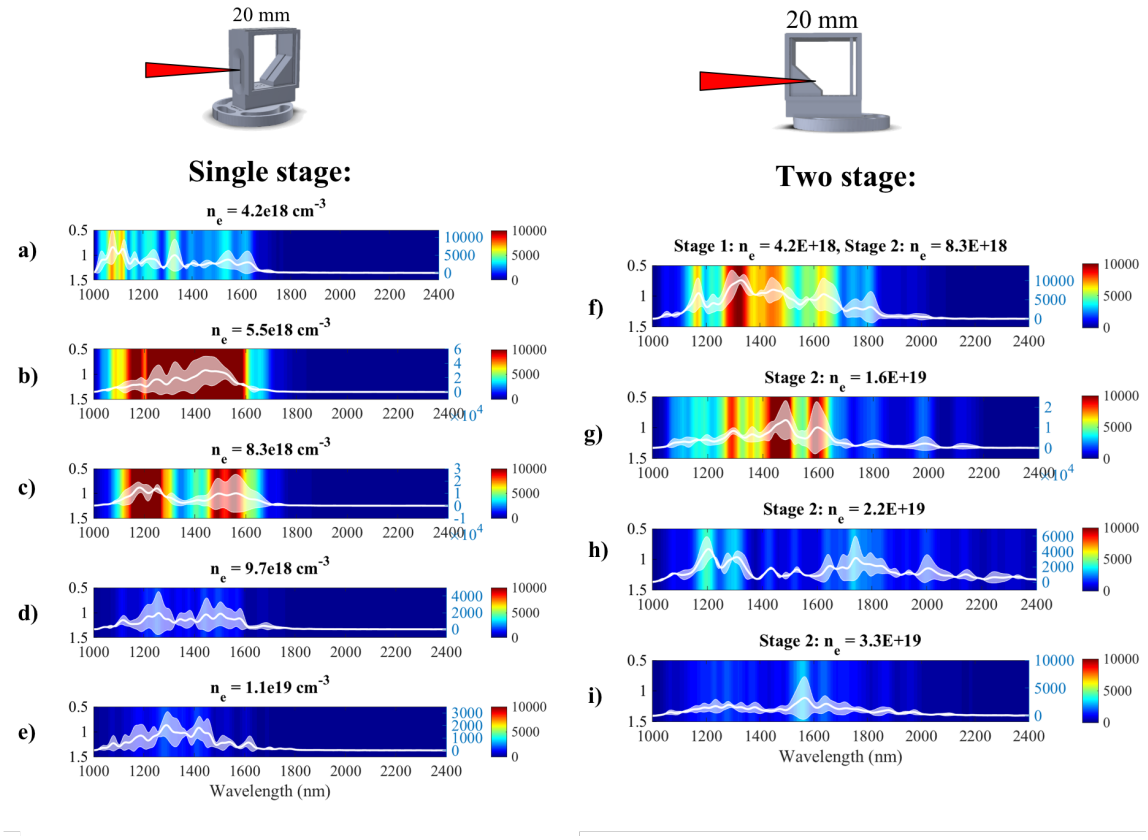

Figure 5.3: Spectral broadening obtained with varying plasma density in **a)** A single stage gas cell and **b)** A two stage gas cell, in which the main stage density was fixed, and second stage density was varied. The color scale represents signal intensity.

average spectrum over multiple shots. The color scale is consistent for all plots and was chosen to demonstrate variations in signal intensity at different conditions. The average spectrum is overlaid in white, with a shaded region demonstrating the standard deviation in spectral counts from individual shots. Note that the line-outs are not presented on the same scale (right axis).

In both cases, the laser pulse traveling through the low-density first (main) stage will create a nonlinear wake as it enters the plasma, and a time varying refractive index gradient, resulting in frequency shifting of the laser pulse. The broadened pulse will also develop a chirp and variation in pulse duration. Using a single stage gas cell spectral broadening was limited to about 2 μm. The highest signal was obtained at

6.5×10^{18} cm^{-3} (Fig. 5.3b), and reduced with increasing plasma density.

In the two stage cell, greatest spectral broadening was achieved with an increase in density in the short second cell to 2.2×10^{19} cm^{-3} (Fig. 5.3h), but decreased with increasing density. The generation of longer wavelengths using a short density up-ramp at the rear of the plasma target is consistent with simulations by Nie et al. [108], where self-focusing and further self-compression of the drive pulse and rapid changes in the refractive index, producing greater broadening. Additionally, the generation of long wavelengths decreases with plasma densities above 2.2×10^{19} cm^{-3}. This is because the front of the laser pulse must remain in a region of negative refractive index gradient to produce long wavelengths. When the plasma density is too high in the second stage the wakefield bubble may break down, no longer containing the long wavelengths. Therefore, the reduction in signal intensity at the highest densities in Figure 5.3 is due to attenuation of the pulse due to collapse of the bubble cavity in which it is contained. Attenuation of long wavelengths may be mitigated by the implementation of a rapid density down-ramp at the rear of the plasma profile (the "coupler" module in Ref. [108]), to expand the wakefield cavity quickly, relative to the mid-IR pulse, maintaining the energy and compressed characteristics of the long wavelength pulse. Unfortunately, achieving a short, rapid density down-ramp is experimentally challenging and difficult to characterize, and therefore was not attempted in these experiments.

In Figure 5.4, the average wavelength as a function of plasma density in the short stage of two-stage gas cell is plotted for four different main stage pressures. In all cases, an optimal value for second stage density for long wavelength production is obtained at an intermediate plasma density, between about (1-3) $\times 10^{19}$ cm^{-3}. The highest average wavelength of about 1550 nm is obtained with a ratio of main

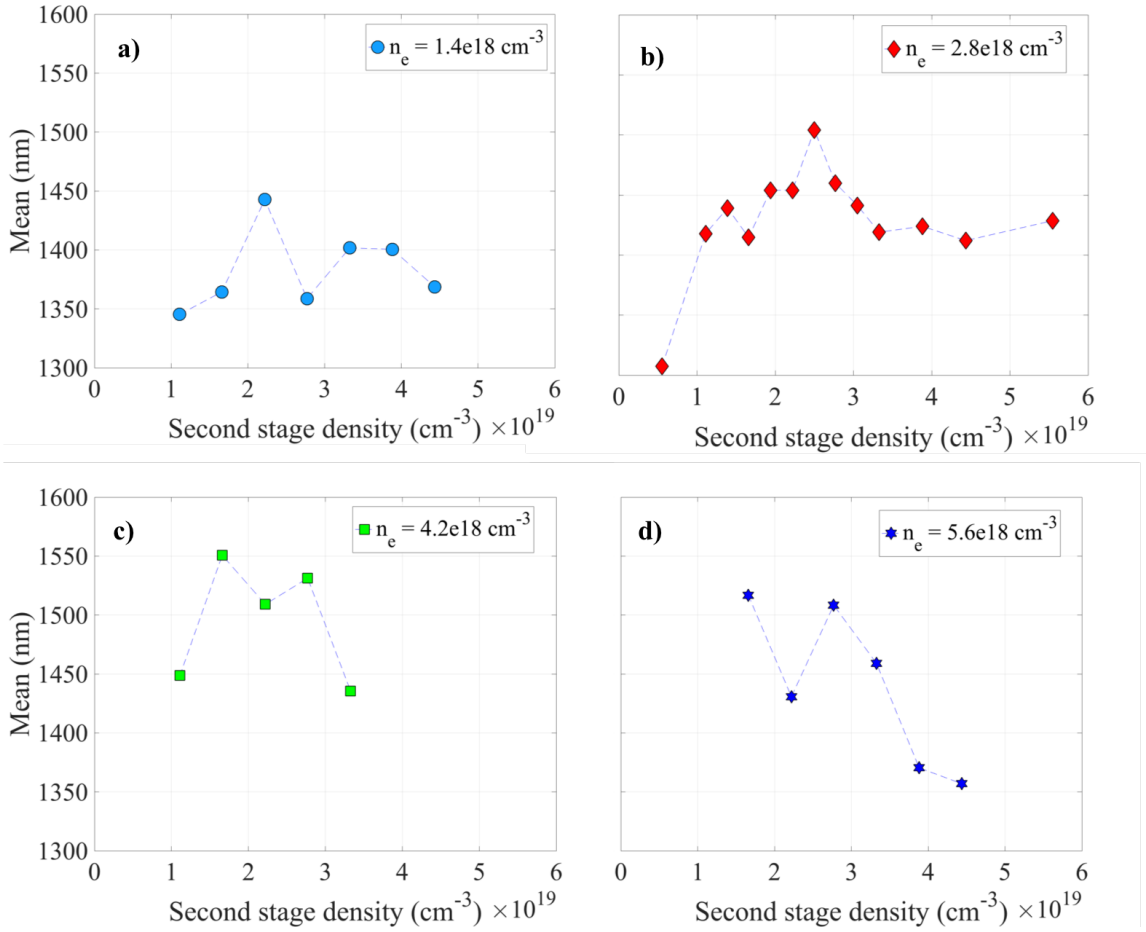

Figure 5.4: Mean wavelength as a function of density in the second stage for two-stage gas cells, presented for four different main stage densities. Each point corresponds to the mean wavelength obtained from the averaged mid-IR spectrum obtained from at least three shots.

stage density of approximately 4 between the main and second stages (n_1 = 4.2 × 10^{18} cm^{-3}, n_2 = 1.7 × 10^{19} cm^{-3}), which is in reasonably good agreement with computational studies by Nie et al. [108] in which the rear stage had three times higher density. Prior to the onset of signal attenuation due to collapse of the bubble wave, spectral broadening increases with plasma density due to the associated drop in the critical power for self-focusing which enhances the ponderomotive force, creating greater charge displacement and a steeper refractive index gradient.

5.3.2 Parametric study of long wavelength generation

The effect of plasma length and grating position (which influences both pulse duration and pulse chirp) on spectral broadening was characterized by investigating the fraction of flight produced in three wavelength regions: (1.0-1.5) μm, (1.5 - 2.0) μm, and (2.0 - 2.4) μm. These fractions were obtained by integrating the measured spectrum in k-space to determine the spectral energy. This analysis technique was chosen such that the data is normalized and the known effect of increased density on signal reduction is not included. The fraction of radiation produced in these wavelength ranges is shown for single and two-stage cells in Figure 5.5, where each point corresponds to the fraction obtained from the average spectrum (over a minimum of three shots).

The plasma density for the single stage cell was fixed at 8.3×10^{18} cm^{-3} and the average laser power was (41 $\pm$ 2) TW. A plasma length of 5 mm was used for the grating scan, where 0.1 mm yielded best compression. The two-stage cell has a density of 1.4×10^{18} cm^{-3} in the main cell and 2.2×10^{19} cm^{-3} in the short cell, and the average laser power was (64 $\pm$ 3) TW. For the two-stage cell, the quoted plasma length refers to the length of the main stage. The grating scan was performed with a plasma length of 5 mm for the grating scan, and best compression was achieved at 0.2 mm.

For single stage cells, a weak enhancement in wavelengths above 2 μm was obtained at a plasma length of 6 mm (Fig. 5.5a). No clear trend emerged with grating position (Fig. 5.5c) or for shorter wavelengths. The greatest spectral broadening obtained with a two-stage cells was achieved at a plasma length of 7 mm, producing the highest fraction of light above 2 μm (Fig. 5.5b). Wavelengths above 1.5 μm were most pronounced at a grating position of -0.4 mm ((Fig. 5.5d), where a

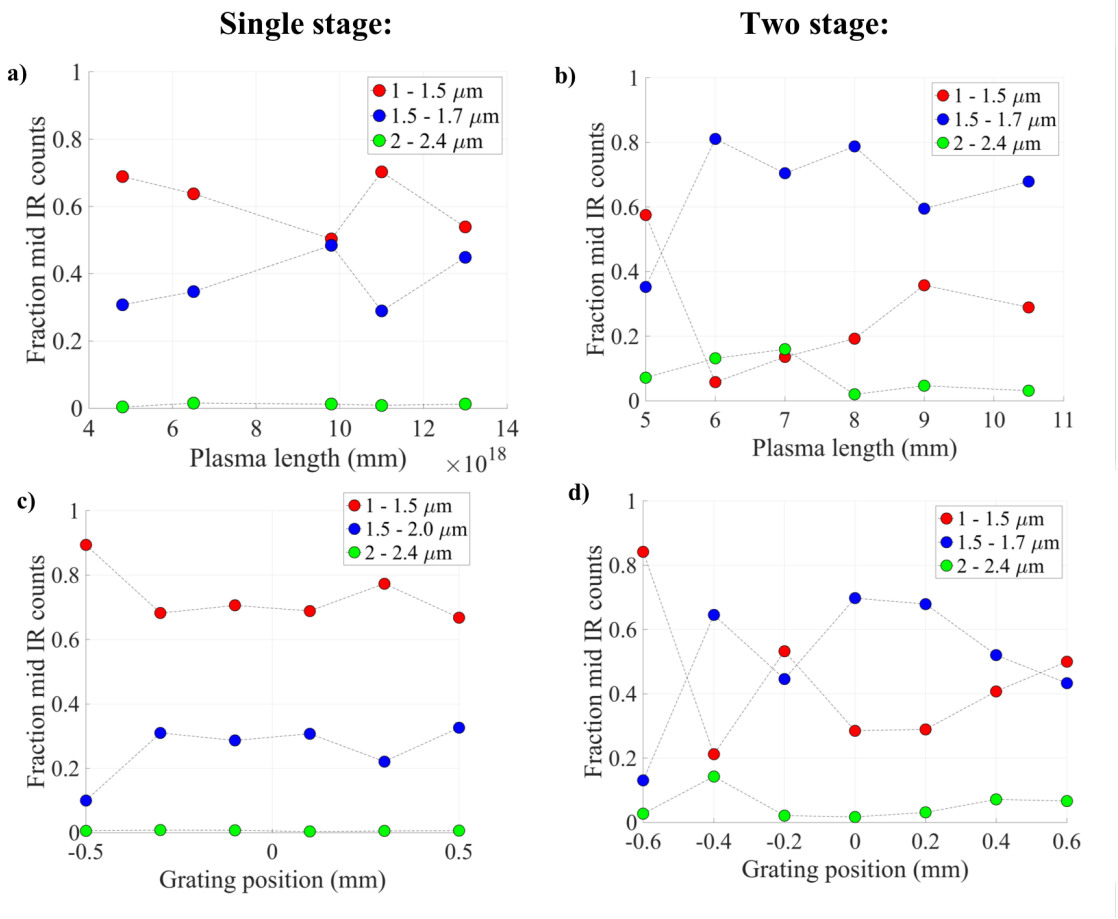

Figure 5.5: The fraction of signal in three wavelength regions plotted as a function of plasma length and grating position for single stage and two-stage gas cells. For single-stage gas cell experiments best compression of the pulse ($\simeq$ 30 fs) was obtained at 0.1 mm, while for two-stage experiments best compression occurred at 0.2 mm. Negative grating values indicate a positive chirp on the laser pulse. Each point corresponds to the fraction obtained from the averaged mid-IR spectrum obtained from at least three shots.

positive chirp has been added to the pulse. However, it is expected that with increasing pulse duration, τ, the conversion efficiency of long wavelength radiation should drop due to the decreased longitudinal ponderomotive force, given that the initial power will decrease as $P \succ 1/\tau$ [110]. A reduced ponderomotive force will reduce charge displacement, resulting in a less pronounced refractive index gradient and reduced spectral broadening. Therefore, the enhancement observed with a grating scan, which will increase the pulse duration while adding a positive or negative chirp,

is surprising and unexpected. It is likely that this anomalous enhancement is due to variation in a combination of plasma and laser parameters, which will be further discussed.

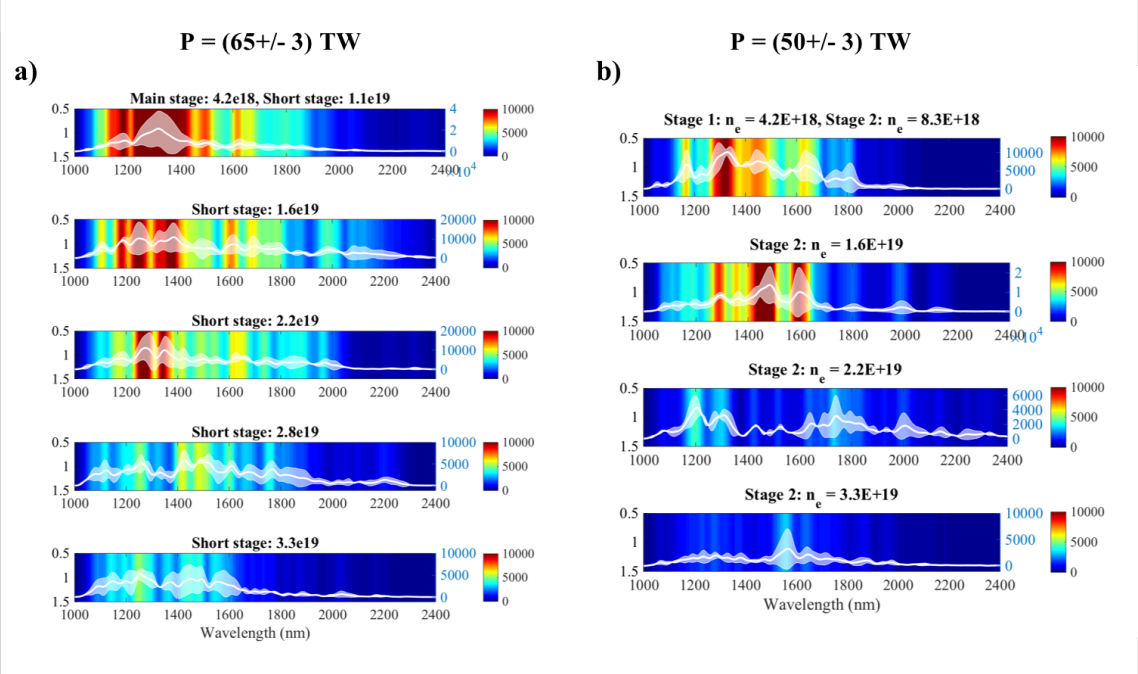

Figure 5.6: Variation in spectral intensity with increasing plasma density in the second stage is shown for two-stage gas cells at two laser powers.

The role of laser power on spectral broadening can be observed in Figure 5.6, where two experiments using two-stage cells were performed with the same plasma densities, but laser powers differing by 15 TW. These experiments were obtained on different experimental days using Setup 1 (c.f. Fig. 5.2), with plasma lengths of 8 mm and 9 mm in Figures 5.6a and 5.6b, respectively. Significant enhancement of the signal intensity is obtained at higher power (Fig. 5.6a), particularly of wavelengths below 2 μm. This is consistent with higher ponderomotive force at high power, resulting in steeper density gradients. In both cases, with increasing plasma density the signal intensity decreases, due to attenuation of the mid-IR pulse in higher density due to breakdown of the bubble cavity.

Computational studies by Zhu et al. [110] have demonstrated that the conversion efficiency of laser energy to long wavelength radiation exhibited a threshold behavior with increasing power, however this effect was not observed in our experiments. Above a threshold power value, the efficiency plateaus due to a saturation of the refractive index gradient caused by complete blow-out of the plasma wave. This is because at the highest powers the plasma wave will be cavitated, reducing the extent of the pulse that undergoes spectral broadening.

5.3.3 Source characterization

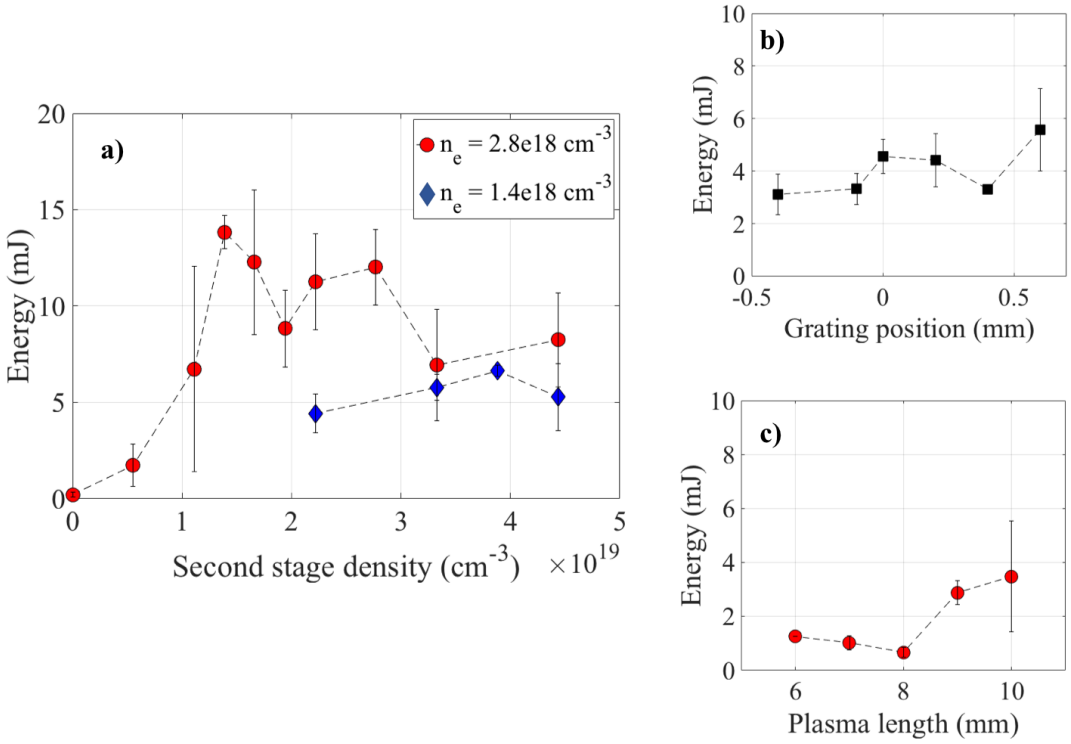

Figure 5.7: Energy in the pulse for radiation exceeding 1 μm. **a)** Variation in pulse energy is shown with increasing plasma density in the second stage for two main stage densities. **b)** Mid-IR energy as a function of grating position, and **c** plasma length.

Alongside the spectral features and broadening of long-wavelength radiation during LWFA, the energy and beam profile of the resultant mid-IR pulse is of paramount

importance for technological and scientific applications. Experimental measurements of the energy contained in wavelengths above 1 μm indicate that this method can successfully produce pulses with energies exceeding 10 mJ. The energy in mid-IR pulses is plotted as a function of plasma density, plasma length and grating position in Figure 5.7, where error bars reflect variations in the measured value over at least three repeat shots.

As shown in Figure 5.7a, mid-IR pulses with energies approaching 15 mJ were obtained using $n_e = 2.8 \times 10^{18}$ cm^{-3} in the main stage and $n_e = 1.4 \times 10^{19}$ cm^{-3} in the second stage (density ratio of 5). Variations in the output energy scale with plasma density in the same wave as long wavelengths, as discussed in previous sections, due to the requirement of steep density gradients for optimized conversion efficiency of the driving laser pulse into mid-IR radiation. Variations in pulse energy as a function of grating position (Fig. 5.7b) and plasma length (Fig. 5.7c) do not show significant enhancement of pulse energy at fixed densities of $n_e = 1.3 \times 10^{18}$ cm^{-3} in the main stage and $n_e = 2.2 \times 10^{19}$ cm^{-3} in the second stage.

The profile of mid-IR beams is also important to the utilization of these sources. Beam profiles were measured from a scattering screen using a Xenics camera. Variations in the beam profile as a function of density in the second stage are shown in Figure 5.8 at a fixed main stage density of $n_e = 1.3 \times 10^{18}$ cm^{-3}. These measurements indicate that mid-IR sources with uniform spatial intensity can be created during LWFA. The intensity of the beam increased with increasing plasma density, consistent with enhanced spectral broadening and conversion efficiency due to steepening of the density gradient. However, the beam profile intensity did not drop off steeply at the highest density, as observed in Figure 5.3, suggesting that beam profile measurements may be saturated at high density and not capturing all of the spec-

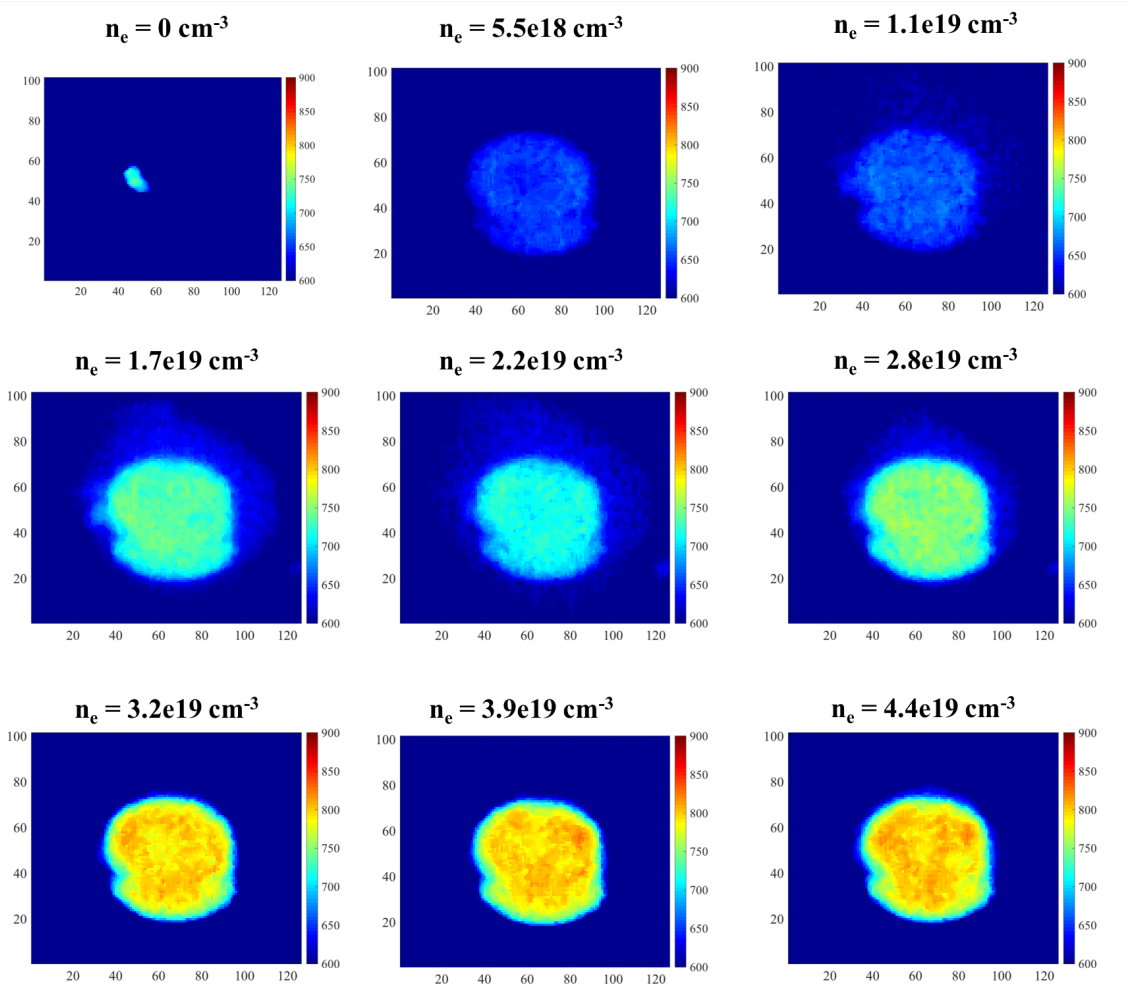

Figure 5.8: The beam profile of long-wavelength pulses obtained from two-stage gas cells with fixed main stage density and increasing second stage density.

tral information of the pulse. The mid-IR pulse was also used to successfully ablate the surface of a copper sample, indicating the viability of these sources for remote detection.

5.3.4 Sensitivity analysis

The parametric study presented in the previous section demonstrates that spectral broadening during LWFA is highly sensitive to variations in laser and plasma properties. In the majority of measured spectra (c.f. Figs. 5.3 and 5.6) it does not

appear that the location and variance of spectral features can be controlled by tuning a single parameter. However, under certain conditions, radiation localized to a specific wavelength range have been obtained. Examples of these spectra are shown in Figure 5.9, where spectra with sub-100 nm variance have been produced with central wavelengths up to nearly 1.85 μm. The spectra in Figure 5.9 present all spectra with signal above the background level obtained at fixed experimental conditions. Figures 5.9 (a, b, c) all differ by more than one parameter and are subject to shot-to-shot variations, although the overall characteristics of the spectra for a given condition are consistent.

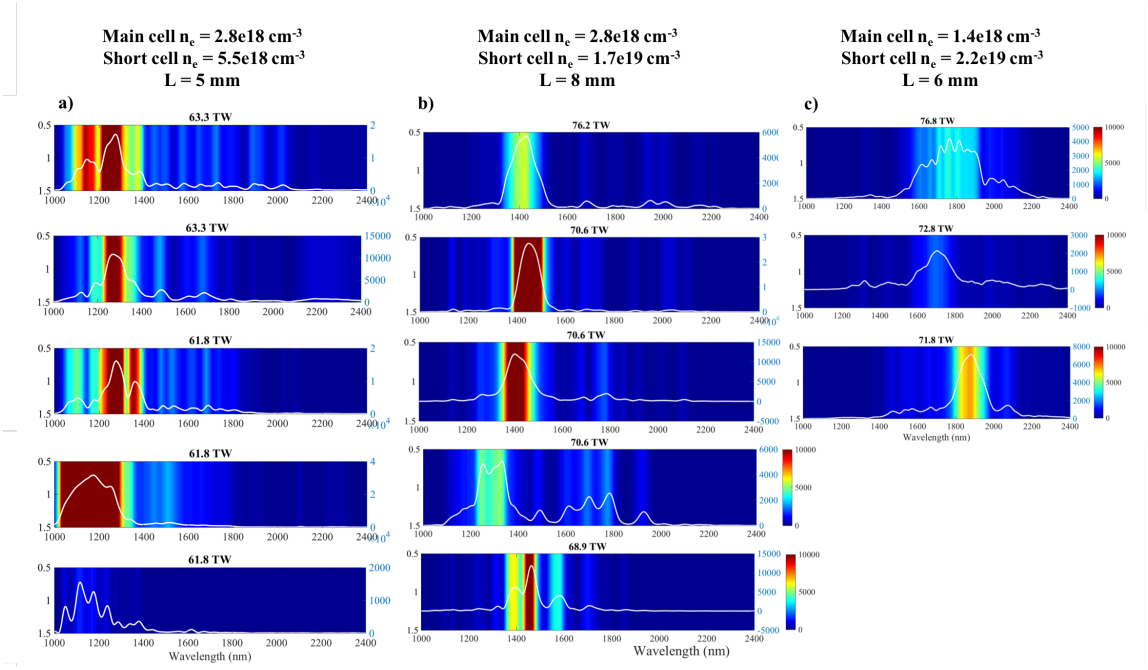

Figure 5.9: Multiple shots at three different experimental conditions demonstrate the production of low-divergence spectra and shot-to-shot reproducibility.

In order to investigate the effect of independent parameters on spectral broadening the covariance matrix was calculated using data from $n = 217$ shots obtained with the two-stage gas cell configuration. The covariance matrix enables the variance of multiple parameter to be determined with respect to each other. In this analysis, six

independent parameters (*m)* were considered: (1) Laser power, (2) Grating position, (3) Plasma length, (4) Density in the short stage, (5) Density in the main stage, (6) Density ratio. The covariance of these parameters was considered with respect to two dependent variables: (1) the fraction of radiation in 2-2.4 μm, (2) the total energy of the mid-IR pulse. This data is compiled into two matrices, each of size (m + 1) $\times$ n.

The sample covariance matrix of a matrix X is given by:

$$\Sigma(X) = \frac{1}{n} X X^T - \mu_X \mu_{X^T} \tag{5.2}$$

where $\mu_X = 1/nX$ is the mean column vector of X. The resultant matrix $\Sigma(X)$ is an (m+1) $\times$ (m+1) matrix (here, 7 $\times$ 7), where the diagonal elements are the variance (σ^2) of the covariance of a variable with itself. The covariance of each independent variable with respect to the dependent variable or interest is contained in the final row of $\Sigma(X)$, in value of zero means no covariance between variables.

Subsequently, the Pearson correlation coefficient is applied to the covariance matrix to determine the parameters which are most highly correlated with a desired output. The Pearson correlation coefficient is a measure of the linear correlation between variables, and yields output variables between + and - 1, with 1 indicating positive and negative linear correlation, respectively. A value of zero indicates no correlation. The formula for the Pearson's correlation coefficient for two variables, $\rho_{x,y}$, is:

$$\rho_{x,y} = \frac{\Sigma(x,y)}{\sigma_x \sigma_y} \tag{5.3}$$

where σ_x (σ_y) is the standard deviation of x (y). From $\Sigma(X)$, σ for each independent variable is obtained from the square root of its diagonals.

The Pearson correlation coefficient for long wavelength generation and pulse energy are given in Table 5.3.4. For the greatest production of wavelengths extending from 2 - 2.4 μm (normalized to the total signal in the pulse), plasma length and laser power were found to have the most pronounced effect, followed by the density in the second stage. The energy in the mid-IR pulse was found to be most variable with laser power and densities in the main and short cells. These results are consistent with the results in Section 5.3.3.

These results indicate that while changing a single parameter can in some instances provide low variance spectrum at desired a wavelength, determining the other laser and plasma parameters that contribute to this condition is not trivial. Therefore, optimization of mid-IR pulses from an LWFA would be best conducted using high-repetition rate laser systems, where adaptive control methods, like those applied in Ref. [106] could be applied to converge on ideal conditions.

Parameter:	**Correlation coefficient: 2 - 2.4 μm fraction**	**Correlation coefficient: Energy (mJ)**
Laser Power	0.70	0.70
Grating position	0.35	0.44
Plasma length	0.71	0.68
Density in second stage	0.63	0.76
Density in main stage	0.59	0.83
Density ratio	0.59	0.62
2 - 2.4 μm fraction	1.00	
Energy (mJ)		1.00

Table 5.1: The Pearson correlation coefficient calculated from two covariance matrices formed by independent variables (first column) with the dependent variable (first row).

5.4 Particle-in-cell simulations

2D Particle in Cell (PIC) simulations were performed by Josh Ludwig at the University of Alberta using the OSIRIS code [87, 88]. The simulation box size was 200 $\times$ 200 μm, with resolution 10000 $\times$ 10000 cells (50 cells/μ m), and 20 electron particles per cell with stationary ions.

An 800 nm, 30fs, f/20, Gaussian laser pulse with (30 - 60) TW power was simulated. The pulse was linearly polarized in the z-direction (transverse to the simulation domain). Density profiles used in simulations for single and two-stage cells are shown in Figure 5.10a and b, respectively. Plasma profile were simulated with varying electron densities in the main stage (n_1, with $x_1 = 10$ mm) and second stage (n_2, with 1 mm length), where present. In all simulations, the electron temperature was initialized to Te = 10 eV.

5.5 Simulation results and analysis

To explore the effect of density tailoring on long wavelength radiation, 2D PIC simulations were conducted with single stage and two-stage density profiles. 1D Fourier transforms of the laser field (E_z) were taken in space along a line-out of the laser axis (y=$L_y/2$=100 μmm) at 200 times during the laser propagation to resolve the laser spectrum as a function of time, as shown in wave-number and wavelength for two stage density profiles in Figure 5.11(a,b). Simulation results show bursts of long wavelength (up to 50 μm) light originating from the laser pulse. The frequency downshifting results from the density gradient at the leading edge of the laser pulse.

Simulations were conducted using single and two-stage density profiles, as shown in Figure 5.10. Lineouts of the Fourier transformed laser field (y=$L_y/2$=100 μmm) after the light has exited the plasma (t = 45 ps) found that long wavelength radiation was enhanced using density tailored targets, in good qualitative agreement with experimental measurements (cf. Figure 5.12a,b).

Simulations indicate that the evolution dynamics of long-wavelength light during LWFA were affected by the interaction with the relativistic electron beam. As the red-shifted light lags further behind the driving pulse a portion of it interacts with

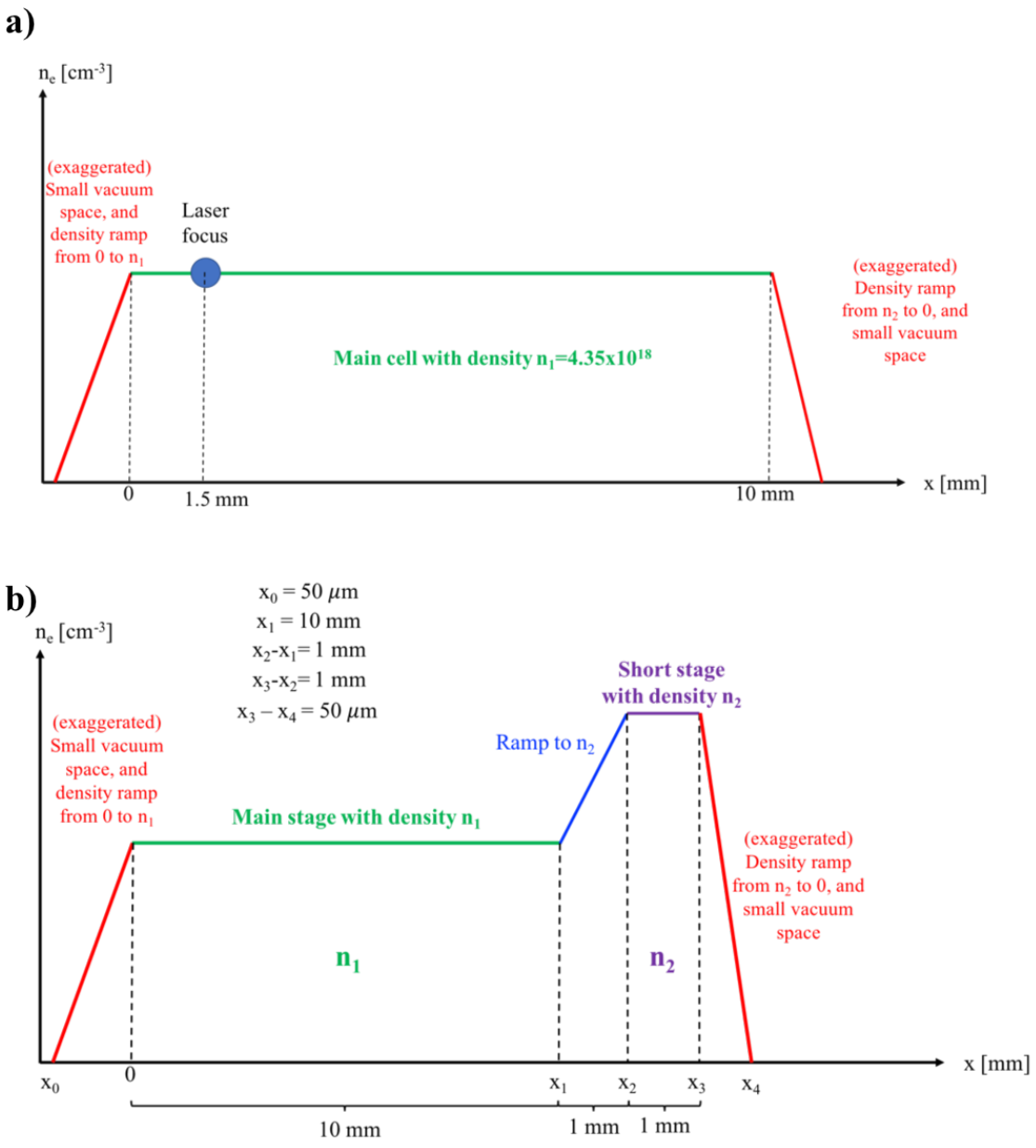

Figure 5.10: **a)**Single stage and **b)** two-stage density profiles implemented in PIC simulations.

an accelerated particle bunch (Figure 5.13a). The result of this interaction is an blueshift and side-scattering of the light, as shown in Figure 5.13b. The particle energy distribution was sampled 200 times during the simulation to give the electron energy distribution as a function of time, as shown in Figure 5.13c.

From the particle energy distribution discrete bunches of accelerated particles

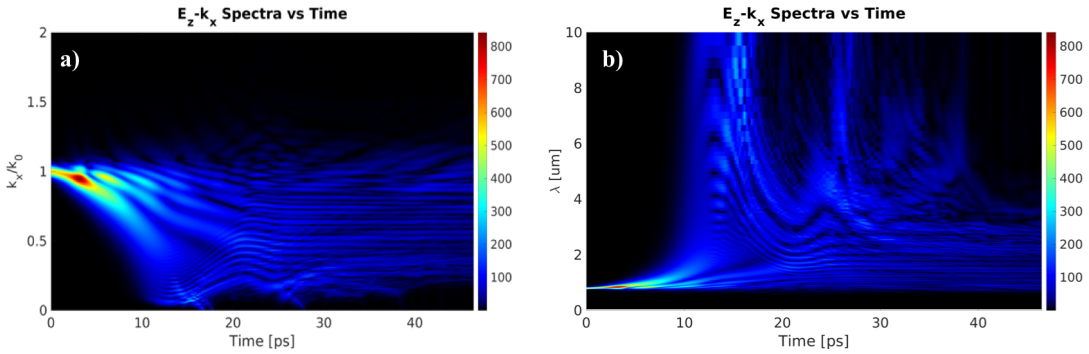

Figure 5.11: 1D Fourier transforms of the laser field (E_z) taken in space along a line-out of the laser axis (y=$L_y/2$=100 μmm) at 200 times during the laser propagation resolve the laser spectrum as a function of time, shown in **a)** wave-number and wavelength (b). Simulations were conducted using an electron density of n_e=4 $\times$ 10^{18} cm^{-3} in the main stage and n_e=(5-8)$\times 10^{18}$ cm^{-3} in the rear stage.

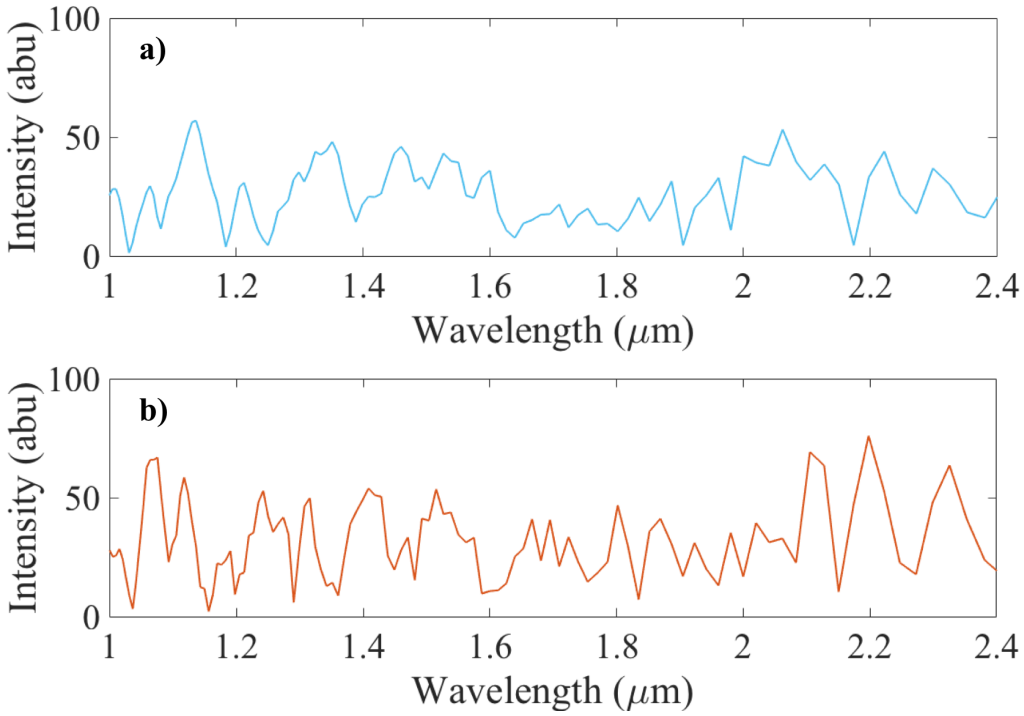

Figure 5.12: Lineouts of 1D Fourier transforms of the laser field (E_z) along the laser axis (y=$L_y/2$=100 μmm) after the light has exited the plasma (t = 45 ps) for single-stage **a)** (n_e = 4.35 $\times$ 10^{18} cm^{-3}) and two-stage **b)** plasma targets (n_1 = 4.00 $\times$ 10^{18} cm^{-3}, n_2 = 8.0 $\times$ 10^{18} cm^{-3}).

can be observed. The bunches will continue to accelerate until they reach dephase from the laser pulse or interact with the lagging long-wavelength light. At 15 ps,

corresponding to the interaction of long-wavelength light with the electron bunch (c.f. Figure 5.13a,b), a rapid drop in electron energy is observed.

At approximately 15 ps, the interaction between the relativistic particle bunch and the slowing light may be modeled as a relativistic mirror. Typically in a relativistic mirror model, the mirror and light are considered to be moving in opposite directions, such that the relativistic mirror upshifts the frequency of the light; however, in this case the light and mirror are moving in the same direction, along the direction of laser propagation. In particular, the high energy particle bunch is moving at nearly the speed of light, with a velocity:

$$\frac{v}{c} = \left[1 - \left(\frac{E_k}{m_e c^1} + 1\right)^{-2}\right]^{1/2} = 0.9999 \tag{5.4}$$

where v is the electron velocity, c is the speed of light in vacuum, $E_k = 300$ MeV is the electron energy and m_e is the electron rest mass.

The red-shifted laser light more slowly than the vacuum speed of light due to the refractive index of the plasma. Laser light at the initial wavelength of 800 nm will move through plasma density of 4.00×10^{18} cm^{-3}, $n_2 = 8.0 \times 10^{18}$ cm^{-3}, at $v_g = 0.9988c$. For 10 μm wavelength light in this plasma, the velocity is reduced to $0.8c$. Therefore, the electron bunch will rapidly outrun long wavelength light. This electron bunch has a high density, exceeding the critical density ($n_e = 2.65n_c$ for 2 μm light and $n_e = 66.5n_c$ for 10 μm light) and therefore acts as a relativistic mirror, blue-shifting and scattering long-wavelength radiation. In this way, the spectrally broadened laser pulse can *decelerate* electrons. The generation of side-scattered long wavelength radiation observed in Figure 5.13b may serve as a diagnostic of electron dynamics and the detrimental interaction of the laser pulse with the accelerated electron bunch, reducing the efficiency of LWFA and maximum electron beam energy.

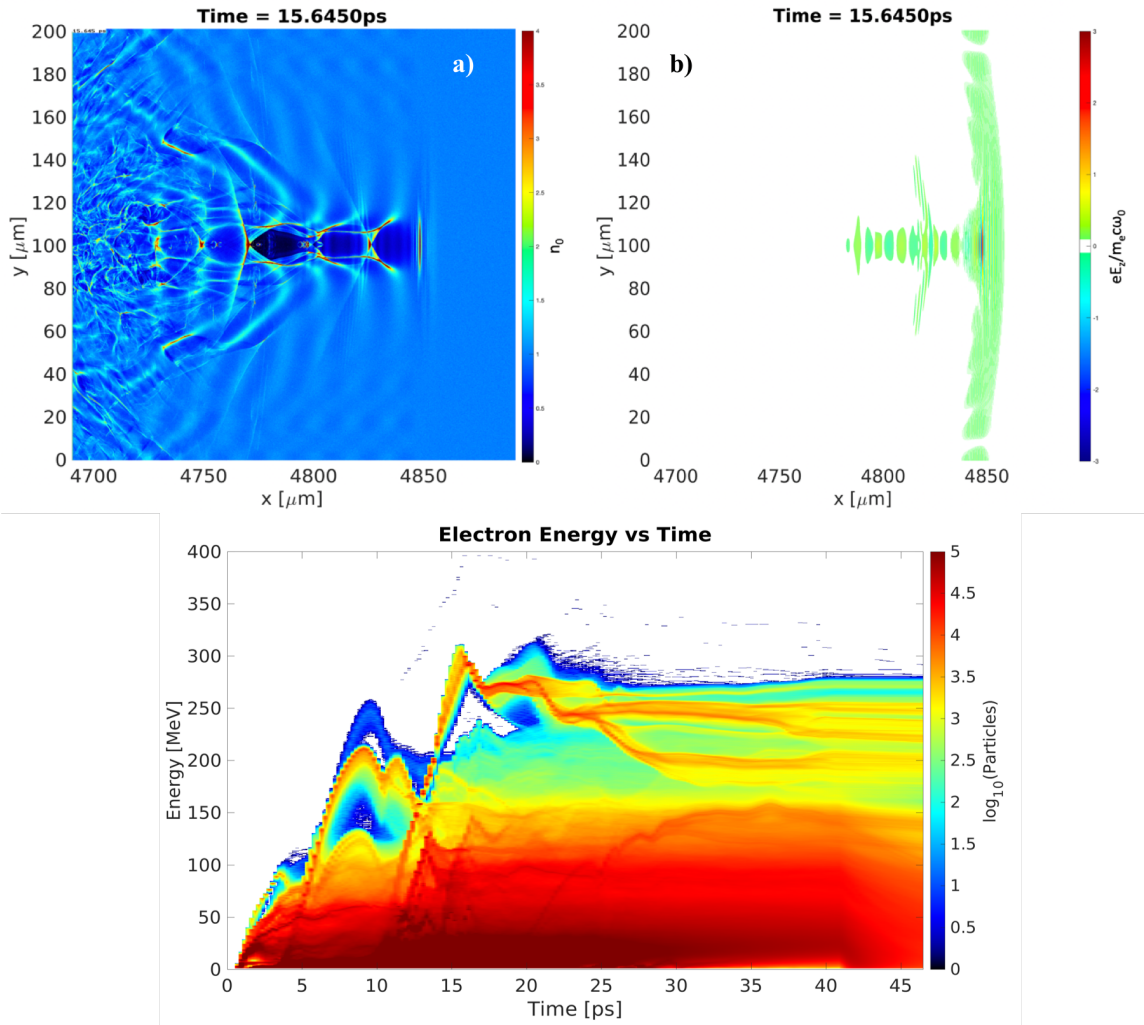

Figure 5.13: **a)** Plasma density at 15.6 ps into the interaction. The accelerated electron bunch sits at approximately 4800 μm. **b** The laser field in time and space, shown at 15.6 ps into the interaction. Simulations were performed with a moving frame, where long wavelength radiation is moving backward with respect to the driving laser field. The formation of long wavelength side-scattering is observed at approximately 4800 μm. **c)** Evolution of the electorn energy as a function of time.

5.6 Conclusions

The generation of long-wavelength radiation extending to 2.5 μm was studied as a function of plasma density, plasma length, laser pulse and chirp, and laser power. The experimental implementation of tailored density targets using two-stage gas cells was found to enhance the production of long-wavelength radiation. Pulses with of 1

- 2.4 μm wavelength were found to contain up to 15 mJ of energy, with high quality beam profiles and the capability to ablate the surface of a copper target. Further, the sensitivity of spectral features to the co-variance of laser power, plasma density and plasma length indicate that the conditions necessary for control and tunability of a long-wavelength source from an LWFA could be achieved by utilizing high-repetition rate laser systems for adaptive control.

Supporting PIC simulations indicate that slow-moving long-wavelength radiation, which slips backward relative to the driving laser pulse, can interact the accelerated electron bunch, decreasing the energy of the electron beam and blue-shifting and scattering long-wavelength radiation. These results suggest that measurements of side-scattered long-wavelength radiation may serve as a diagnostic of electron dynamics and bunch formation.

CHAPTER VI

Backward stimulated Raman scattering from a laser wakefield accelerator

6.1 Introduction

SRS is a three-wave interaction that occurs in plasma at densities less than quarter critical ($n_c/4$), where the critical density is $n_c = m_e\omega_0^2/4\pi e^2$. Raman scattering involves the decay of the incident electromagnetic laser wave, ω_0, into an electrostatic plasma wave, ω_{pe}, and a scattered wave, $\omega_{scatt} = \omega_0 - \omega_{pe}$. For $n_e << n_c$, forward SRS results in the generation of relativistic plasma waves with wavelength $\lambda_p \simeq 2\pi c/\omega_{pe}$,

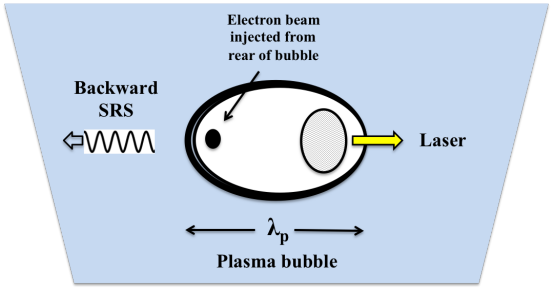

Figure 6.1: A schematic of Stimulated Backward Raman Scattering (SBRS) within a laser wakefield plasma bubble. The relativistic plasma wavelength is given by λ_p. The interference of forward going laser light and backward propagating SRS can give rise to a beat structure on the laser wave packet.

while backwards SRS generates non-relativistic waves with a wavelength $\lambda_p \simeq \lambda_0/2$. Interference between forward going light and backward propagating SRS light gives rise to a beat structure on a wave packet, which drives the plasma wave growth. A schematic of this interaction is given in Fig. 6.1. In the relativistic regime, where the electric field for electron acceleration is on the order of $m_e c^2/\lambda_p$, the laser pulse duration can be comparable to the growth rate of parametric instabilities such as Stimulated Raman Scattering (SRS) [57, 111, 112, 56, 113].

For "long" pulse durations (nanoseconds), backward Stimulated Raman Scatter (BSRS) can lead to the scattering and redistribution of incident laser light as well as plasma heating and hot electron generation by SRS driven plasma waves. Therefore, the presence of BSRS for inertial confinement fusion-related studies has posed a challenge for effective laser-plasma coupling [114, 115]. The spectral signatures of BSRS have been found to depend on laser intensity. At high intensities with picosecond duration pulses, spectra exhibit broadening and modulation of the frequency spectrum, potentially due to "bursting" of the scattered light from the instability (rapid fluctuations in scattering intensity) [57, 116, 112, 111, 113]. The spectra obtained from BSRS can be used as a diagnostic of the physics of high intensity laser plasma interactions [116, 111, 56, 117, 82].

The duration of BSRS light is related to the propagation time of the laser pulse through the plasma, and therefore can be much longer than the incident laser pulse. The growth rate of the SRS instability depends on the strength of the laser electric field, E, which is characterized by the dimensionless normalized vector potential, $a = v_{osc}/c = Ee/m_e\omega_0 c \propto I^{1/2}\lambda$, where v_{osc} is the peak quiver velocity, ω_0 and λ are the laser frequency and wavelength, respectively, and I is the laser intensity. For high-intensity laser pulses ($I > 10^{18}$ W/cm^2), the peak quiver velocity of an electron

in the laser field, can approach the speed of light, resulting in growth rates of the SRS instability that exceed the electron plasma frequency ($\omega_{pe} = 4\pi n_e^2/m_e$). This is known as the *strongly coupled* regime, and is associated with components shifted to multiples of the plasma frequency ω_{pe}, resulting in a highly broadened spectrum that is not clearly connected to the laser spectrum [56].

Strongly coupled SRS measurements from picosecond duration ($\simeq$ 800 fs) pulses have been previously made, with the width of the spectra exceeding the plasma frequency [57]. A transition from classical to anomalous (broadened) BSRS with increasing laser intensity has been observed experimentally from 600 fs laser pulses [112]. Additionally, measurements from 450 fs high-intensity ($I > 10^{18}$ W/cm^2) laser pulses have yielded spectra with large-amplitude modulations [111]. Experimental measurements of BSRS from 120 fs pulses at sub-relativistic intensities have also been reported, where the amount of backscattered light was found to decrease at low pressures due to the ponderomotive expulsion of electrons along the laser axis [118]. BSRS measurements have also been made during LWFA with laser powers up to 8 TW (max intensity of $\simeq 2 \times 10^{19}$ W/cm^2) [119]. Kaganovich et al. observed saturation of BSRS signal due to strong self-focusing at increasing gas pressures (plasma densities). Their experimental results were consistent with BSRS generation in the weakly nonlinear regime, where the growth rate of SRS is positive only in a very narrow spectral region, resulting in a frequency component of the laser pulse with a width less than ω_{pe}.

The observation of these broadened, highly modulated BSRS spectra, which are not predicted by the standard parametric theory of SRS, highlights the role of non-linear dynamics in electron plasma wave generation [120, 59]. For high-intensity, short-pulse interactions, very large amplitude electron plasma waves are produced,

in which the oscillating electrons can have very high velocities. To account for the relativistic correction to electron mass (nonlinear detuning) at these intensities, Kono and Škorić included a nonlinear term in their one-dimensional model of SRS in a weakly-collisional plasma [121]. Their theory predicts a saturation of backscattered light for lower laser pump amplitudes, given by the ratio of the electron quiver velocity in a laser pump field to the speed of light ($eE_0/m_e\omega_0 c$), revealing quasiperiodic structures. However, with increasing pump strength, pronounced spectral broadening and chaotic bursting of back-scattered emission was observed, indicating a transition to chaos and eventual loss of coherent modulation. 1D-PIC simulations of Raman backscattered spectra were found to produce modulated spectra with increasing complexity as a function of pump strength, agreeing with experimental measurements from a 0.8 ps laser pulse by Darrow et al. [57]. Therefore, the extreme broadening of backscattered spectra may indicate scattering from many unstable plasma modes in the strongly coupled regime due to loss of coherence of plasma waves during wave-breaking [57, 56, 58]. Broadening may also be due to spatiotemporal localization (bursting) of the Raman scattered light within the laser pulse from a rapid saturation of the SRS instability [58, 59].

Additionally, electron injection and trapping during LWFA is connected with the wave breaking of electron plasma waves (EPW) having phase velocities approaching the speed of light [58]. Instabilities with a self-modulating laser pump can couple to relativistic plasma waves, creating new sidebands in the forward spectra, and contributing to the growth and ultimate breaking of these EPWs [56, 58]. However, severe side scattered SRS has been found to degrade electron beam quality in LWFA through the seeding of filamentation instabilities in the electron beam, as well as erosion of the incident laser pulse [82].

Backward SRS in the strongly coupled (strongly non-linear) regime during LWFA have not previously been observed experimentally. In the bubble regime of LWFA, the importance of this phenomenon is also unclear, however the backward SRS may generate large amplitude short wavelength plasma waves in a partially "evacuated" plasma bubble, which may affect the dynamics of electron injection and acceleration in this regime. Previous studies motivate measurements of backscattered spectra produced at these ultra-short pulse durations as a diagnostic of the interaction. Of particular interest is the efficiency and control of electron self-injection, which may potentially enable optimization of the LFWA mechanism, and generation of electron beams with higher charge. The utilization of BSRS to generate a counter-propagating photon beam could also be used to produce X-rays by the Compton scattering of photons with energetic electrons accelerated by LWFA [122, 123]. This method of all-optical Compton scattering could produce X-rays with a wide range of energies up to 1 MeV, and could provide a compact alternative to existing linear electron accelerator devices. Photons generated *via* BSRS may provide a more tractable realization of all-optical Compton scattering as compared to the use of two separate ultra-short pulses to generate the energetic electron-photon interaction.

Experiments conducted using the HERCULES laser system at the University of Michigan produced experimental measurements of backward SRS generated during LWFA in the strongly coupled regime. Resultant backscattered spectra were found to be highly modulated and significantly red-shifted beyond 830 nm in cases where electrons were accelerated. A correlation between the total amount of BSRS and charge of the accelerated electron beam was observed for laser powers exceeding 100 TW. The amount of BSRS (characterized by the intensity of the of the measured spectrum beyond 830 nm) was also found to increase as a function of plasma density

at these powers. For laser powers above 100 TW, where the ponderomotive force of the laser is higher, the BSRS signal was significantly less red-shifted, while still correlating with electron beam charge and plasma density. For laser powers below 50 TW, no such correlations were observed. Therefore, it is clear that the red-shift broadening of the backward SRS spectrum is associated with increased electron beam charge in a LWFA. These experiments were complemented by two-dimensional PIC simulations that indicate growth of BSRS until the wakefield bubble is evacuated of electrons due to relativistic self-focusing of the laser. Simulations and experiments indicate that measurement of backward propagating SRS may be used as a diagnostic of bubble formation and trapped electron charge within the bubble. A summary of the experimental setup is given in Section 6.2, PIC simulations are described in Section 6.3, and results and analysis are given in Section 6.4.

6.2 Experimental setup

Experiments were conducted using pulses from the HERCULES Ti:sapphire laser system. Pulses with powers between 20-180 TW (1.3×10^{19} W/cm^2 - 1.1×10^{20} W/cm^2) were focused using an f/10 off-axis parabolic mirror onto a pulsed gas jets generated from gas jet nozzles between 1.55 mm and 5 mm in diameter. A deformable mirror was used to correct the laser wave front and produces a focal spot with a full-width-half-maximum (FWHM) of 10 μm. Gas jet pressures up to 800 psi helium gas were utilized, yielding plasma densities up to 6×10^{19} cm^{-3}. Backscattered light was collected using an aluminum mirror at an angle of 5.5 degrees from the nozzle and collimated onto the entrance slit of an Ocean Optics HR2000 spectrometer (200-1100 nm). The laser spectral bandwidth was measured to be 30 nm; therefore, for backscattering measurements the area under the red-shifted spectrum was considered

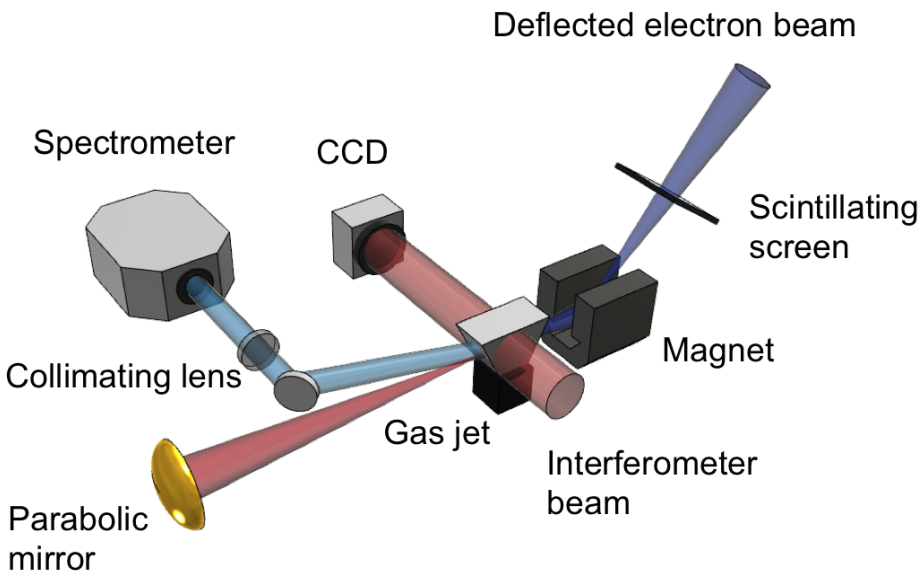

Figure 6.2: Experimental setup for measurements of Backward Stimulated Raman Scatter on the HERCULES laser (800 nm, 30 fs, 30-200 TW, 4" diameter, focused with an f/10 parabola, shown in red). Interferometry measurements of electron density were made using a probe beam from a pellicle in the main interaction beam. An Ocean Optics HR2000 spectrometer resolving 200-1000 nm was used to measure backscatter signal (shown in blue) from the rear of the gas nozzle. Backscattered light was collected using an aluminum mirror and collimated through a 37 cm focal length lens of 125 mm diameter. Electron energies were measured using a 0.8 T magnetic spectrometer, a scintillating LANEX screen and a CCD camera.

for wavelengths beyond 830 nm. This region of the spectrum was chosen for the analysis of backscattered spectrum to avoid errors due to scattered laser light inside the target chamber. An electron spectrometer (using a 0.8 T magnet) with a LANEX phosphor scintillating screen and a charge coupled device camera enabled electron energy detection between 47-800 MeV. Interferometer measurements of the plasma density were obtained using a transverse probe beam. A schematic of the setup is given in Fig. 6.2.

6.3 Particle-in-cell simulation parameters

Two-dimensional simulations of a 30 fs, 800 nm laser pulse at 100 TW and 140 TW in varying plasma densities were performed by Josh Ludwig (University of Alberta) using the relativistic particle-in-cell (PIC) code SCPIC [89], which has previously been used to study electron acceleration in the bubble regime [124]. These simulations provide additional insight on the kinetic processes leading to SRS and particle loading. Simulations used a domain of 400μm $\times$ 200μm with resolution 12,000 $\times$ 6,000 cells (30/μm) and 16 particles per cell. Electron plasma densities of (0.5-2)$\times 10^{19}$ cm^{-3} were simulated, assuming a plasma temperature of 50 eV. Several diagnostic probes were placed on the simulation boundaries to record SRS as the laser propagates in the x-direction through the plasma. A linear density ramp of 100 μm from vacuum to full density was included in the model.

6.4 Results and Analysis

A typical experimental backward SRS spectrum obtained from 30 fs laser pulses at 50 TW and 180 TW is given in Fig. 6.3a. A background backscatter shot without gas is also plotted for comparison. Dramatic broadening and modulation of the BSRS spectrum is observed at all powers with the generation of an electron beam. The laser intensity is centered at 800 nm and a red-shift in the BSRS spectrum was considered as signal extending beyond 830 nm (with 30 nm taken as the nominal spread of the laser wavelength). The integrated area under the red-shifted BSRS spectrum is taken as a Figure of Merit of the total BSRS signal, since the measured spectrum is approximately symmetric.

The spectrum measured without gas in Fig. 6.3a resembles the laser spectrum and results from stray light scatting inside the target chamber. We note here that

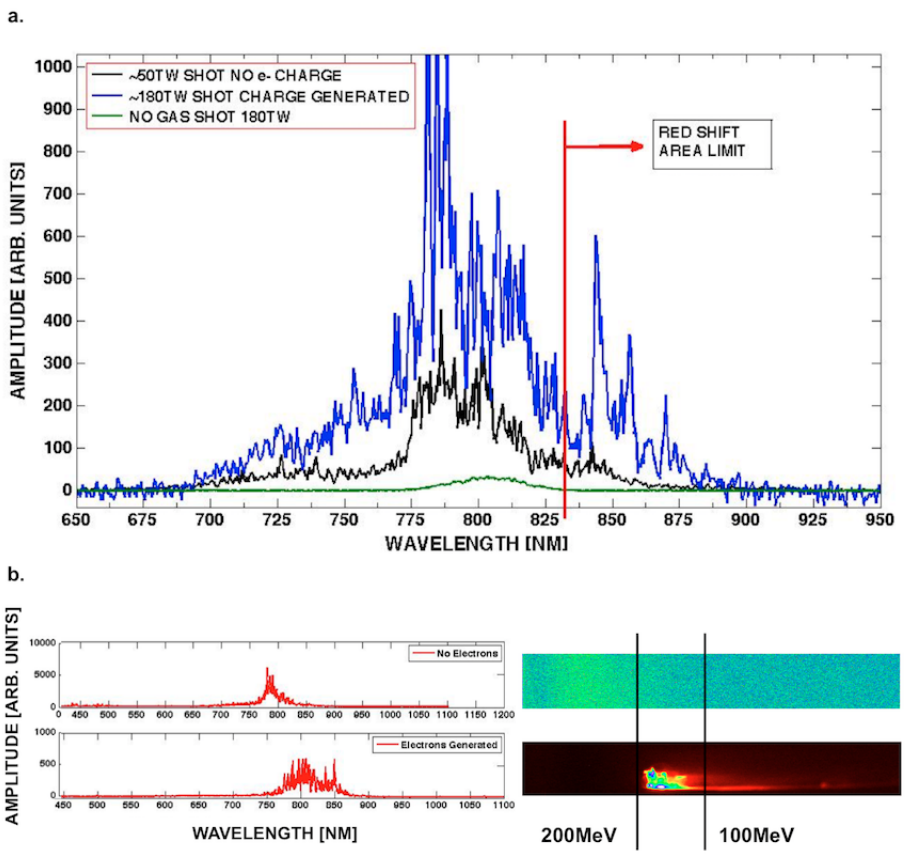

Figure 6.3: **a)** Example of Backward SRS spectrum, from a 180 TW laser shot producing electrons (blue), a 50 TW shot in which electrons were not produced (black), and a 180 TW shot without gas (green). The red-shifted area was considered as signal extending beyond 830 nm. **b)** Measured BSRS spectra and associated electron signal on the scintillating LANEX screen, demonstrating broadening and red-shifting of the BSRS spectrum with electron generation.

the signal level within the incident laser spectrum is negligibly weaker than the shots with gas and the BSRS signal dominates the signal. The observed broadening and modulation of the BSRS spectrum are similar to measurements at longer pulse durations in the strongly coupled regime [57, 112]. However, the modulation of the spectrum is more pronounced than any previously observed.

A comparison between BSRS spectrum with and without electron generation is given in Fig. 6.3b with associated electron signal. These measurements were obtained at a laser power of 30 TW, using a 1.5 mm diameter gas jet nozzle. No specific correlations between the energy spread of the electron beams and the amount of SRS

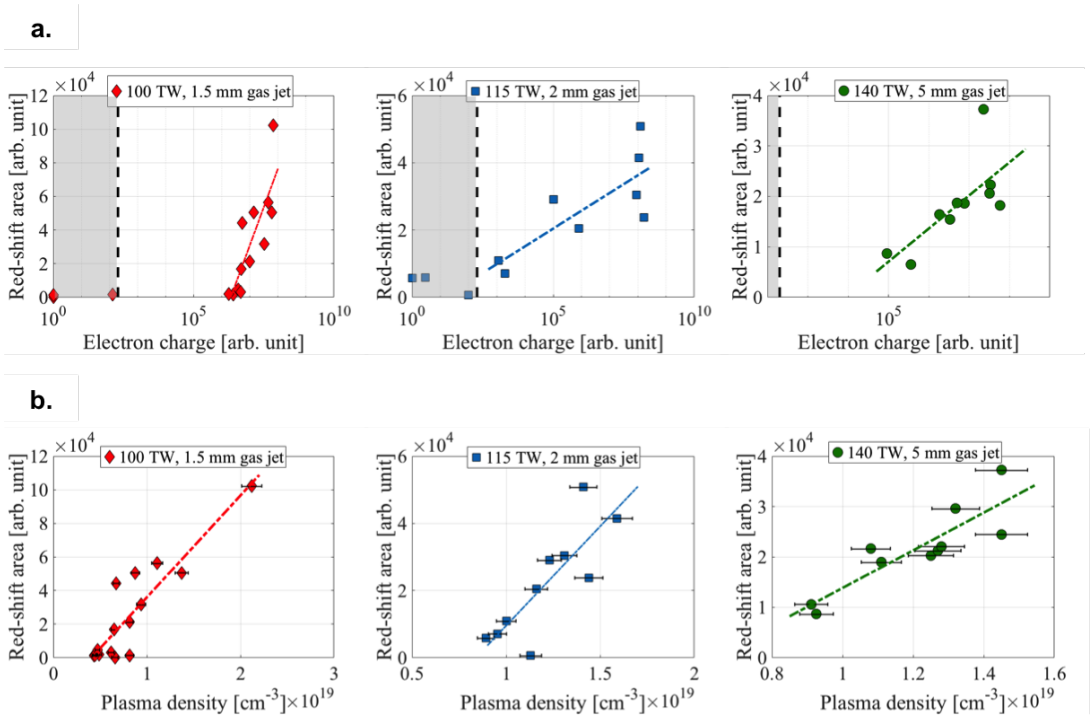

Figure 6.4: Total area under the red-shifted BSRS spectrum (representing the total BSRS signal) for helium gas at 100 TW, 115 TW and 140 TW, for three gas jet nozzles, where the quoted length refers to the nozzle diameter. Error bars for the integrated spectrum are the same size as the plotted points. **a)** The total BSRS signal is plotted as a function of integrated charge, on a semilogarithmic scale. An increase in BSRS signal as a function of charge generation is observed for all powers, and all nozzle diameters. Linear least square fits are shown to demonstrate this trend. Electron signal below 200 counts is considered background, and is represented by a shaded region. Error bars for the integrated charge are negligible relative to the signal and are not plotted. **b)** The total BSRS signal was found to increase as a function of plasma density at each laser power and nozzle diameter. Linear least square fits are shown. At all powers and nozzle densities, the electron charge was found to increase with plasma density.

were observed. Electron measurements shown in this figure correspond to signal on a scintillating LANEX screen. The contrast on each LANEX image is optimized to show variation in the signal above background, therefore these images do not have the same contrast.

BSRS broadening was found to increase with electron beam charge generation and plasma density for laser powers at and above 100 TW. Measurements taken at 100 TW, 115 TW and 140 TW, with 1.5 mm, 2mm and 5 mm diameter gas jet nozzles, respectively, are presented in Fig. 6.4. The integrated signal in the red-shifted BSRS

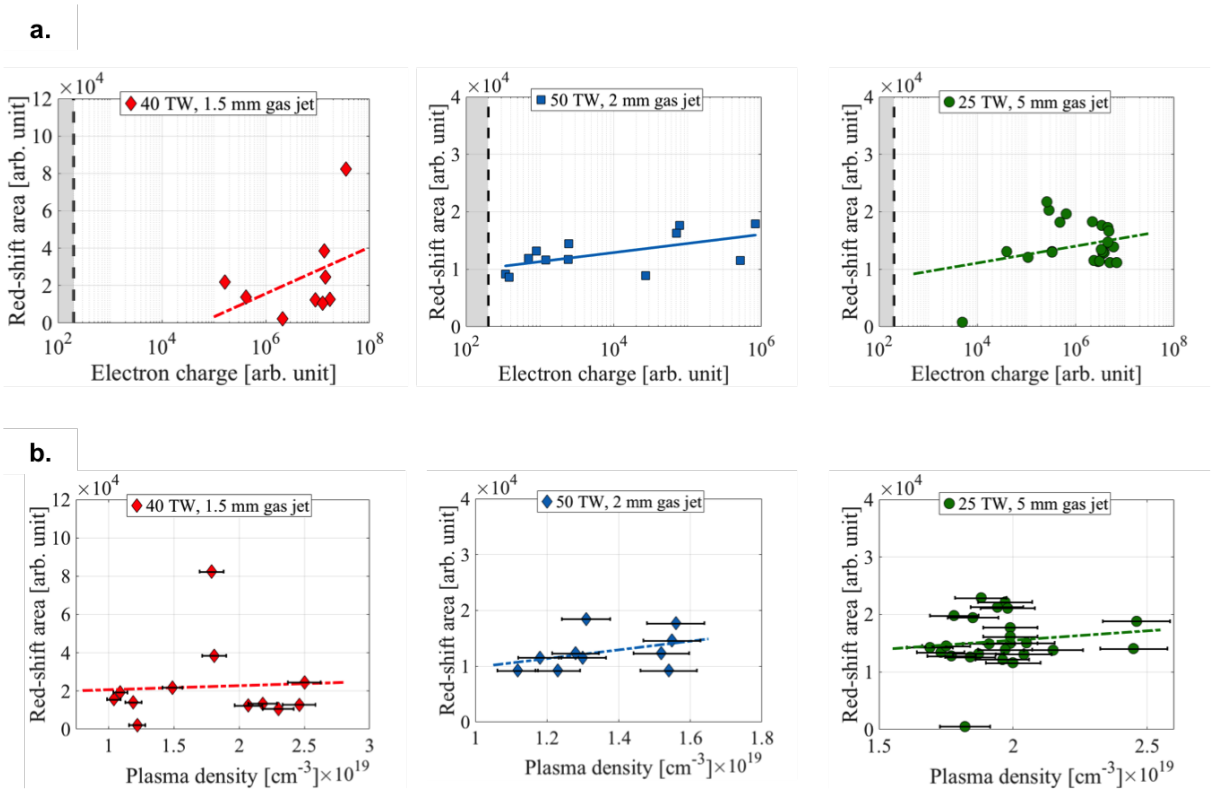

Figure 6.5: Total area under the red-shifted BSRS spectrum (representing the total BSRS signal) for helium gas at 50 TW and below, for three gas jet nozzles, where the quoted length refers to the nozzle diameter. Error bars for the integrated spectrum are the same size as the plotted points. **a)** A clear correlation between BSRS signal and electron charge does not emerge. Linear least square fits are shown. Electron signal below 200 counts is considered background, and is represented by a shaded region. **b)** No clear relationship between plasma density and the total BSRS signal is observed; linear least square fits are shown. Additionally, no relationship between the electron charge and plasma density was found for powers at and below 50 TW.

spectrum as a function of electron charge is plotted on a semilogarithmic scale in Fig. 6.4a, and as a function of plasma density in Fig. 6.4b. Plasma density was determined from interferometry images. Electron charge, presented in arbitrary units, refers to the integrated intensity of electron signal from the electron spectrometer onto the scintillating screen. All signal below 200 counts is considered background, and for all shots with near-zero BSRS there was also near-zero electron charge. For each power and nozzle diameter, each plotted point corresponds to a single laser shot from a single experimental run. The plotted data reflects all points obtained under the same experimental conditions (quoted power and nozzle diameter).

Linear least squares fits are plotted for each power to highlight an increase in BSRS as a function of electron charge on a semilogarithmic scale in Fig. 6.4a, and an increase in BSRS as a function of plasma density on a linear scale in Fig. 6.4b. However, these fits should not be considered as a scaling, as the process is highly non-linear. Note that the y-axis varies for each plot, with the total BSRS signal decreasing with increasing power. The total BSRS signal is greatest at 100 TW. Additionally, at laser powers at and above 100 TW, the integrated electron charge was found to increase with increasing plasma density. Correlations between BSRS signal and electron and plasma density are persistent for all nozzle diameters.

For powers of 50 TW and below, variations in the BSRS signal with electron charge is not as dramatic. This is shown in Fig. 6.5a. For helium gas targets at powers from 25 TW to 50 TW a clear trend is not obvious across all powers and nozzle diameters. Linear least squares fit to the semilogarithmic plot as a function of electron charge are shown for comparison with Fig. 6.4a; the total red-shifted area (and therefore the total BSRS), does not appear to increase with the total charge in the resultant electron beam. Additionally, at these lower powers, no clear correlation

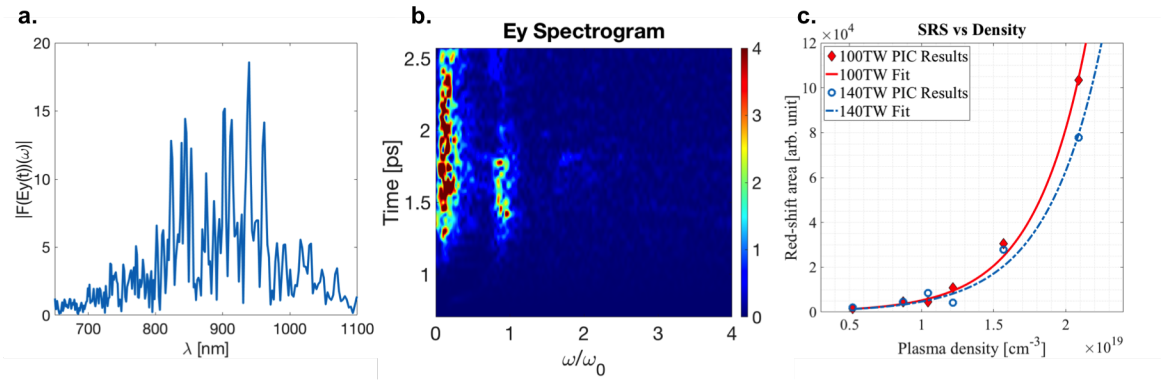

Figure 6.6: PIC simulations reveal a finite duration to the backward traveling SRS signal. **a)** An example BSRS sample from PIC simulations indicating red-shifting and broadening as observed in experimental data. **b)** Time history of backscattered light frequency from PIC simulations at the diagnostic probe from the 100 TW laser in a plasma of density 2.09×10^{19} cm^{-3}. Results show plasma waves at $\omega_{pe} \simeq 0.1\omega_0$ (electrostatic waves that reach the probe) and backward traveling SRS at $\omega_{SRS} \simeq 0.9\omega_0$. **c)** An increase in the total BSRS signal as a function of plasma density is observed, where total signal is represented by the integrated red-shifted area of the simulated BSRS spectrum beyond 830 nm. Exponential fits to the data are shown.

between the total BSRS signal and plasma density is observed. This data is plotted in Fig. 6.5b. Linear least squares fits are also shown for comparison with the high power trends in Fig. 6.4b. No obvious trend between BSRS signal and plasma length can be observed.

The results in Fig. 6.4 and Fig. 6.5 indicate that the intensity and broadening of the BSRS spectrum is most pronounced at powers above 100 TW. Additionally, the total area under the BSRS spectrum at powers below 100 TW was nearly half that observed for higher laser powers. The increased bandwidth and "spikey" structure of BSRS spectrum may indicate very rapid growth rate and saturation of the backward SRS instability at high laser powers.

Two-dimensional PIC simulations enabled a detailed analysis of BSRS production in a LWFA. Backward SRS signal was observed in the SCPIC simulations and the time history was recorded. Typical probe spectra are shown in Fig. 6.6a and Fig. 6.6b. Numerical simulations also reproduce the highly modulated experimental

backscatter spectrum, indicating the applicability of PIC simulations for modeling SRS in LWFA interactions. The production of anomalous spectra may also be influenced by relativistic frequency shifts in plasma waves, as predicted in calculations by Škorić et al. [59], wherein pronounced anomalous spectra, characterized by broadening and chaotic bursting, indicated a loss of coherent modulation for high laser intensities. However, no relativistic plasma waves due to BSRS, as postulated by Škorić et al. [59], were observed.

The BSRS spectrum was recorded from PIC simulation probes for laser powers of 100 and 140 TW. The integrated area under the red-shifted spectrum (beyond 830 nm), representing the total BSRS signal, is plotted as a function of plasma density in Fig. 6.6c. Each point corresponds to a single laser event. An increase in the total BSRS signal as a function of plasma density is observed and exponential fits to the data are shown. As in the experiments, PIC simulations show an increase in the SRS signal with plasma density and confirm that the 100 TW laser pulse typically produces more SRS than the 140 TW laser pulse.

PIC simulation results reveal a finite duration to the BSRS signal, as shown in the backscatter diagnostic probe of Fig. 6.6b. While bubble formation begins almost immediately upon the laser entering the plasma, the bubble is not completely evacuated of electrons until the laser is self-focused to sufficiently high intensity. During the period when there is finite electron plasma density inside the bubble, BSRS is produced from the laser, and once the bubble is evacuated the scattering stops.

A significant BSRS signal is observed only in simulations where the laser intensity is below the critical intensity for complete blowout of electron density in a bubble [125]. For 100 TW laser power, complete blowout occurs at plasma densities be-

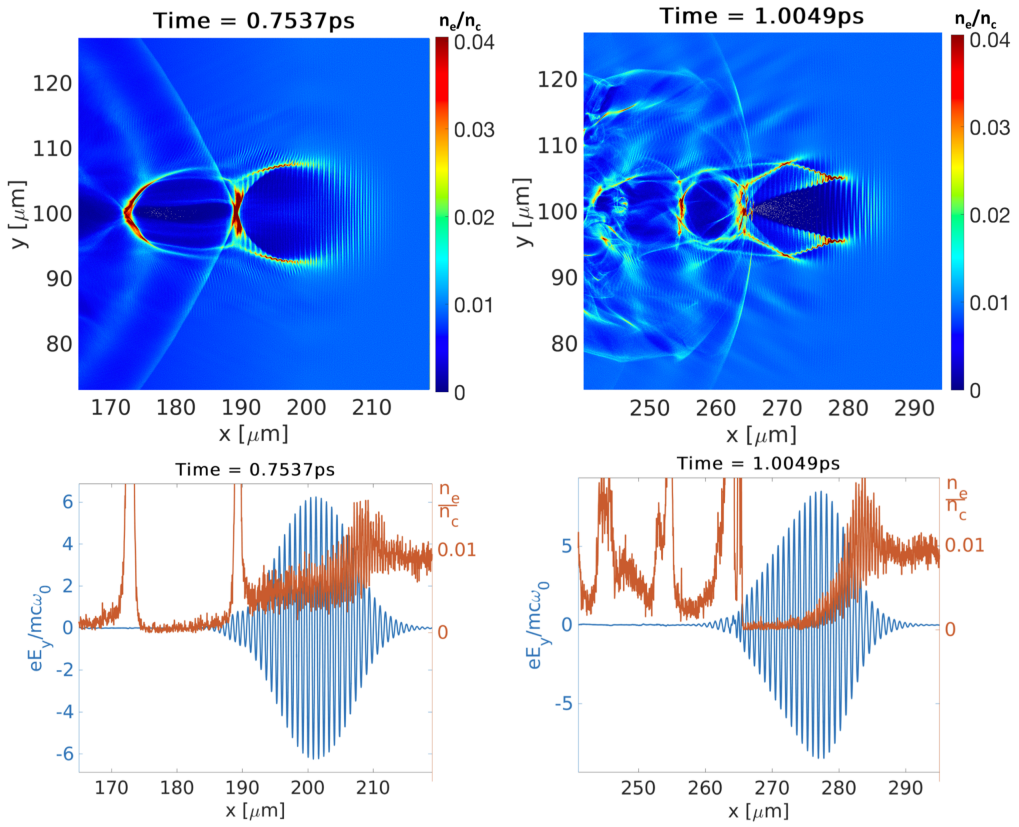

Figure 6.7: 2D PIC simulations of the 100 TW laser in a plasma of density $1.56 \times 10^{19}\text{cm}^{-3}$. **a)** Plasma electron density at t = 0.75 ps, showing finite electron density inside the LWFA bubble resulting in SRS. **b)** Plasma electron density at t = 1.00 ps, showing complete evacuation of electrons from the LWFA bubble due to relativistic self-focusing of the laser. **c)** Laser amplitude and plasma density versus propagation distance 1D cut along x, at $y = L_y/2 = 100\ \mu m$ at t = 0.75 ps and **d)** t = 1.00 ps.

low 1.2×10^{19} cm^{-3} (c.f. Fig. 6.6c). At higher densities, the balance between the ponderomotive force of the laser and the force that arises due to the charge separation may allow for finite electron density inside the bubble.

For all the sub-critical laser intensity simulations, the evacuation of the wakefield bubble and termination of backward SRS occurred at about 700 fs after the laser entered the plasma. Fig. 6.7 shows 2D simulations and line-outs of plasma electron density as a function of time, indicating complete evacuation of electrons due to relativistic self-focusing of the laser after a propagation time of about 1 ps (simulation time).

By using the theory for complete electron blowout given by [125, 7], one can estimate the amplitude of the laser pulse required for complete evacuation of the bubble, for a given plasma density. Laser pulses with initial electric field amplitude below this threshold will first undergo relativistic self-focusing before complete evacuation of the bubble occurs.

Combining the laser amplitude requirements with a theory for relativistic self-focusing [126, 127] results in a critical length parameter that determines the distance the laser pulse must travel in the plasma before its bubble is completely evacuated:

$$z_c = Z_R \sqrt{\left[\frac{a_0}{a_c} - 1\right]\left(1 - \frac{P}{P_c}\right)^{-1}} \tag{6.1}$$

$$a_c = \left[\frac{b^2}{2} + \frac{1}{2}(b^4 + 4b^2)^{1/2}\right]^{-1/2} \tag{6.2}$$

$$b = \Big((k_p r_0)/2\Big)^2 \tag{6.3}$$

where the real component of z_c is defined to be the critical length for blowout (i.e. restricting $a_0 \leq a_c$ and $P > P_c$), Z_R is the laser Rayleigh length, a_0 is the initial normalized amplitude of the laser, a_c is the critical laser amplitude for complete

blowout [125, 7], P/P_c is the ratio of the laser power to the critical power for relativistic self-focusing, $k_p = \omega_{pe}/c$ is the plasma wavenumber, and r_0 is the diffraction limited spot size of the laser.

The amplitude threshold for the blowout increases with density, and the critical power P_c for the relativistic self-focusing decreases with higher plasma densities. This results in a nearly constant critical length z_c (independent of plasma density) for lasers with initial amplitude below the threshold for complete bubble evacuation. The critical length (6.1) $z_c \approx 33$ μm for 100 TW lasers, corresponding to $n_e > 1.2 \times 10^{19}$ cm^{-3}. To estimate z_c from the simulation results, cf. Figs. 6.7c,d, one could evaluate the distance between the beginning of the homogeneous plasma at the end of the density ramp, $x \approx 200\mu m$ in Fig. 6.7c, and the location of the fully evacuated electron density in Fig. 6.7d at $x \approx 270\mu m$. The extent of the critical length, $z_c \approx 70\mu m$, observed in PIC simulations corresponds very well to the region of the strong BSRS signal and corresponding duration of the scattered signal at the probe (see Fig. 6b and note that due to the counter propagation of the laser and its SRS, the duration of the scattered light signal is expected to be $2z_c$/c). Also, $z_c \approx 70\mu m$ remains nearly constant in all runs at different plasma densities. The observed discrepancy between theoretical prediction and PIC results are well within the expected limitation of the scaling argument in Equation (6.1) and rough estimates based on the simulation results in Fig. 6.7.

While finite densities in the bubble (due to sub-critical laser amplitudes for the full electron evacuation) result in the strongest BSRS signals in the short PIC simulations, there is always SRS present due to plasma density at the front of the bubble (see Fig. 7d), which is also lower for higher intensity lasers because of the steeper density gradient. This BSRS produced at the front of the bubble is less prominent

in the short PIC simulations.

PIC simulations indicate that BSRS signal persists until the wakefield bubble is evacuated due to relativistic self-focusing of the laser. Thus, measurement of backward propagating SRS appears to be a result of non-zero electron plasma density within the bubble. One explanation for this correlation is that the BSRS instability may be seeded by noise produced by electron injection into the bubble during self-focusing. Consequently, BSRS signal and time-resolved backscattered spectra may be useful as a diagnostic of bubble formation and trapped electron charge.

6.5 Conclusions

We performed the first experimental measurements of backward strongly coupled SRS in the bubble regime of LWFA. The observed spectra are unlike those observed in previous experiments, and are characterized by a very spikey structure, consistent with 2D PIC simulations, cf. Fig. 6.6a. The observed backward Raman spectrum is correlated with enhanced electron charge in the accelerated beam. For laser powers at and above 100 TW, the integrated BSRS spectrum at wavelengths beyond 830 nm (representing the total BSRS signal) was found to increase with both electron charge and plasma density. For laser powers below 100 TW, no such correlation was observed.

Two-dimensional PIC simulations show a correlation between BSRS signal and plasma electron density within the laser wakefield bubble. For increasing laser intensities, the intensity and duration of the BSRS signal decreases as electron density within the bubble is rapidly depleted. The BSRS signal is enhanced when the electron density in the bubble is nonzero. The broadened, highly modulated spectra obtained from backscattered light are also observed in PIC simulations. They are

results of rapid variations in the background plasma conditions during bubble formation and scattering of backscattered light on the secondary plasma wakes that are formed behind the primary bubble containing the short laser pulse. It has been shown in the past that wake formation contributes to the frequency shifts of the laser pulse [128, 129], and this in turn affects spectrum of the scattered light. These spectra of scattered light are reminiscent of the transition to chaos and eventual loss of coherence due to nonlinear detuning at relativistic laser intensities [121, 59]. However, no such transition has been observed in PIC simulations with varying laser powers. In addition, the low BSRS reflectivity would not be sufficient to produce relativistic Langmuir waves that would be responsible for such frequency shifts.

These results indicate that at highest powers (100 TW and above), the bursting, broadening and modulation of the BSRS frequency spectrum is associated with increased plasma density within the LWFA plasma bubble. The existence of a non-evacuated wakefield bubble, as indicated by backward SRS signal, may be related to enhanced electron injection, resulting in enhanced charge in the accelerated electron beam. The correlation observed between electron beam charge and BSRS is likely due to density fluctuations in the plasma, which may be due to the injection of electrons into a LWFA bubble. These fluctuations can provide a seed for the development of the BSRS instability. Therefore, it is possible that fluctuations due to BSRS can provide feedback for electron injection.

CHAPTER VII

Laser-wakefield accelerators for high-resolution X-ray imaging of complex microstructures

7.1 Introduction

Betatron X-ray beams produced *via* LWFA have been shown to produce stable, bright X-ray beams capable of high resolution tomographic imaging [16, 18, 19, 20, 21, 22, 43]. One exciting application for these novel X-ray sources is as a diagnostic tool for additive manufacturing processes. Laser-aided solidification is an avenue of interest in manufacturing science that requires *in situ* measurements with high spatial and temporal resolution[130, 131]. Such is the case for the solidification of eutectics, in which two (or more) solid phases grow simultaneously from a parent liquid phase[132, 133, 134, 135]. Once solidified, eutectics act as *in situ* composite materials, providing outstanding mechanical and electrical properties that are not afforded by their constituent phases alone. It is for this reason that lightweight Al-Si alloys comprise over 90% of the total Al parts produced by the United States [136]. *Irregular* eutectics such as Al-Si are composed of one faceted phase (Si) and

another non-faceted (Al) phase. Due to the stiffness of the faceted phase, irregular eutectics feature a non-periodic arrangement of lamellae (fine rods or sheets of adjacent material). The interfacial dynamics underlying irregular eutectic solidification (under relatively low cooling rates) has only recently been elucidated through synchrotron-based X-ray microtomography (denoted XRT), using conventional accelerators. [137]. In general, the lamellar spacing (between Al and Si phases) can be as fine as 1 μm, thus requiring experimental probes that are capable of delivering high resolution information.

Synchrotron-based XRT in the micrometer range have been achieved using modern third generation light sources, such as the the beamline for TOmographic Microscopy and Coherent rAdiology experimenTs (TOMCAT) of the Swiss Light Source (SLS) at the Paul Scherrer Institut in Switzerland [138]. The TOMCAT beamline has been employed to produce high-resolution, multimodal X-ray tomographic images using monochromatic sources with energies between 8 and 45 keV, a source size of 127 μm (V) $\times$ 38 μm (H) (FWHM) and a flux of (0.5 - 2)$\times 10^{12}$ photons/sec/mm^2 [139]. However, while conventional synchrotron light sources yield high average brightness, they are prohibitively large and expensive, limiting access to these facilities. The 1000 $\times$ stronger accelerating gradients in a LWFA enable miniaturization of the accelerator to a standard laboratory scale, potentially increasing the accessibility of advanced photon sources. And although compact synchrotron sources have recently been developed [140], laser-driven sources also have the unique capability to be co-timed to other laser-initiated events. In this way, LWFA sources can be used for so called *pump-probe* experiments of laser-irradiated targets [24, 21]. Additionally, while the source size of newest generation conventional beamlines has been reduced to the order of 10 - 20 μm, the resolution limit for X-ray imaging in a parallel beam

geometry on these systems is dependent on the pixel size of the detector and the brightness of the source. Conversely, for a LWFA X-ray source, where the source size has been measured to be on the order of a few micrometers [16, 18, 20, 22], high resolution measurements are obtained using a high geometric magnification, and the resolution requirements of the detector are relaxed.

LWFA experiments conducted using the Gemini laser at RAL investigated the potential of laser-based X-ray sources for the imaging of solid density targets. In this chapter, a comparison between the image sharpness and resolution of raw projection images of Al-Si alloys obtained *via* conventional synchrotron X-ray phase contrast imaging at the Swiss Light Source (SLS) and X-ray projection microscopy *via* a LWFA is presented.

7.2 Experimental methods

7.2.1 Conventional synchrotron X-ray phase contrast imaging

Phase contrast imaging of an Al-Si sample was conducted *ex situ* at the TOMCAT beamline of SLS (Paul Scherrer Institut, Switzerland) [138, 139] in 2012. This data was obtained from Prof. Ashwin Shahani (University of Michigan). In these measurements, the sample was located 20 m from the source and the sample-to-detector distance was set to 11 cm for a monochromatic X-ray energy of 28 keV produced by a broad-band ($\Delta E/E \approx 2\%$) W/Si multilayer monochromator, resulting in virtually no geometric magnification in the X-ray regime, i.e. a value of approximately 1. The X-ray radiographic image, which is produced by the absorption and refraction of the X-ray beam within the sample, was converted to visible light using a 100 μm thick LuAG:Ce scintillator. The corresponding visible light image was then optically magnified by a 10 $\times$ microscope objective onto the imaging chip of a pco.2000 CCD camera with 7.5 μm pixel size, yielding an effective pixel size of 0.75 μm. Individual

images were acquired with a 500 ms exposure time.

7.2.2 LWFA betatron X-ray phase contrast imaging

LWFA experiments were conducted using the Gemini laser at the Science and Technology Facilities Council (STFC), Rutherford Appleton Laboratory (RAL). The 40 fs FWHM laser pulse was focused using an $f/40$ parabolic mirror into a gas cell producing an electron beam. A schematic of the experimental setup at the Gemini laser system is given in Figure 7.1a). 3D printed two-stage gas cells have been shown to improve the stability, divergence and energy spread of LWFA accelerated electron beams [78], therefore a two-stage gas cell with a 3 mm first stage for injection and a 2 - 21 mm variable length second stage was employed in this experiment. Plasma density was controlled by altering the pressure of the gas supply of each individual stage, and density measurements were made using Stimulated Raman Side Scattering measurements. The plasma density corresponding to the optimum betatron spectrum was $n_p = (4.1 \pm 0.45) \times 10^{18}$ cm^{-3} in both stages at a length of 15.5 mm.

For these densities, electron beams with average peak energies of (1000 $\pm$ 150) MeV were produced. Example electron beams are shown in Figure 7.1b), with a superimposed line-out of the spectrum, indicating a quasi-monoenergetic peak and a broad low-energy tail. A 1 T magnet was used to disperse the electron beam onto a scintillating LANEX screen, from which the electron beam was imaged using a CCD camera. Low energy features on the beams are likely untrapped energetic electrons, which have been found to form ring structures [141, 142].

The X-ray beam, which was assumed to be synchrotron-like as shown in Figure 7.1c), contained 1.94 $\pm$ 1.24 $\times 10^8$ photons above 5 keV, and is estimated to have a source size smaller than 3 μm. The X-ray beam was collected by an on-axis X-ray camera (model: Andor iKon-L SY DW936 BR-DD) with a 250 μm beryllium filter,

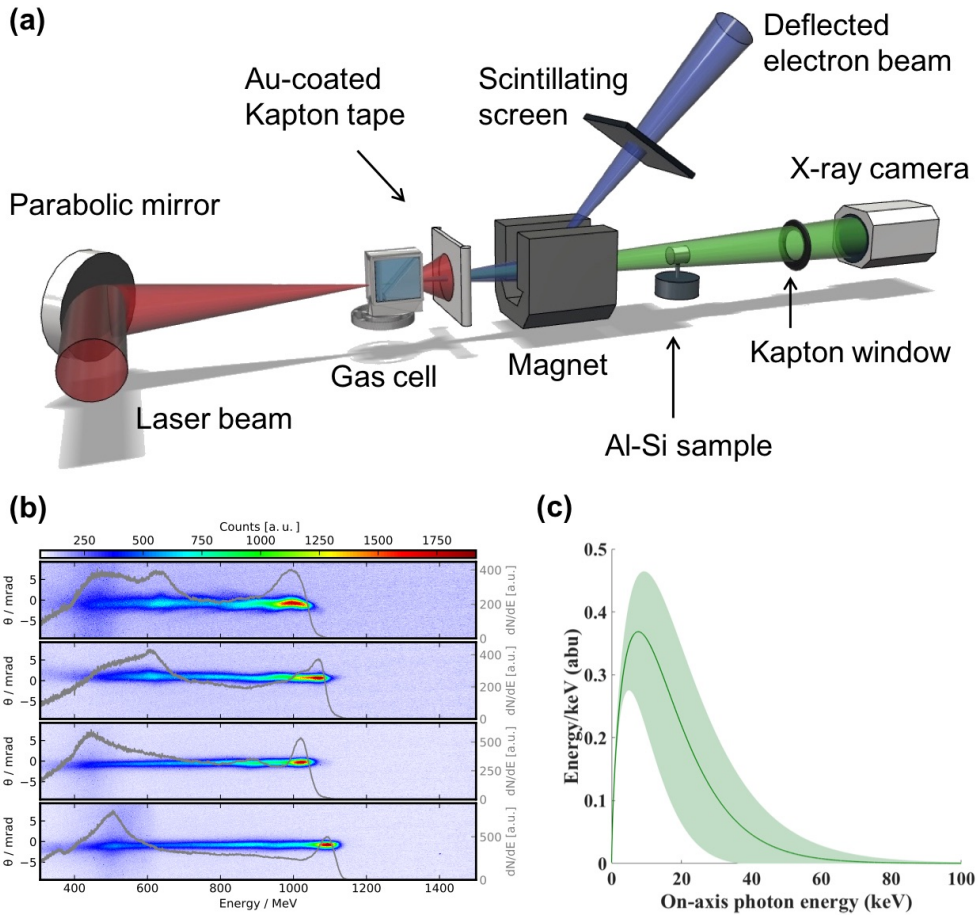

Figure 7.1: Experimental details for X-ray imaging using a laser wakefield accelerator. **a)** Experimental layout. High energy electron and X-ray beams were produced by focusing the beam into a two-stage gas cell. Gold-coated Kapton tape was used to block the laser pulse following the interaction, and was replaced on each shot. A 1 T magnet was used to disperse the electron beam onto a scintillating LANEX screen, from which the electron beam was imaged using a CCD camera. Betatron X-rays passed through the Al-Si sample, which was mounted on a rotation and translation stage at a distance of 19.3 cm from the source. Measurements were made through a Kapton vacuum window onto an Andor iKon 2048 × 2048 pixel CCD camera at a distance of 410 cm from the Al-Si sample. **b)** Samples of typical electron beams with a quasi-monoenergetic peak energy and broad low-energy tails. These measurements were obtained at the same experimental conditions as the phase contrast images and betatron spectrum. Electron beam divergence is plotted on the left axis and a line-out of the electron number density (right axis) is overlaid. **c)** A best-fit to the betatron X-ray spectrum from an Andor iKon X-ray camera was obtained using a 9-element filter array. Shaded error bars reflect the uncertainty in the critical energy over many shots due to shot-to-shot fluctuations in electron energy.

placed 429.3 cm away from the source. In front of the X-ray camera a 9-element filter array composed of various materials with different K-edges was placed to characterize the X-ray spectral distribution [20, 16]. Further discussion of this method is given in Chapter3.4.4. The LWFA X-ray beam has been found in similar experiments to have divergence on the order of a few millirads [23, 20, 22] and femtosecond duration [24, 21].

The electron and X-ray measurements shown in Figure 7.1b) and c) were not obtained simultaneously, but were taken at identical experimental conditions. Simultaneous measurements of the electron beam with phase contrast imaging was not possible in these experiments due to the necessity of an additional "kicker" magnet to protect the sample by further deflecting the electron beam. In all experiments, the Al-Si sample was 19.3 cm away from the betatron source and an X-ray CCD camera with pixel size of 13.5 μm and a 100 ms exposure time was located 410 cm behind the sample. A total of 136 single-shot images were acquired and no reconstructions were applied.

7.2.3 Al-Si samples

Al-Si samples for phase contrast imaging were prepared by the Materials Preparation Center at Ames Laboratory, with a composition of 50 wt% Si for the LWFA experiment and 30 wt% for the SLS experiment. Although the Al-Si sample used in the LWFA experiment had 20% more Si than that used in the SLS experiment, this excess Si is associated not with the Al-Si eutectic but rather the primary (*i.e.*, pro-eutectic) Si phase. The larger mass fraction of this primary Si phase in the Al-Si alloy used in these experiments clouded the field-of-view in the X-ray images, limiting the eutectic — which is last to solidify — to a smaller region of the sample. However, this has little to no bearing on the development of the eutectic microstructure. Both

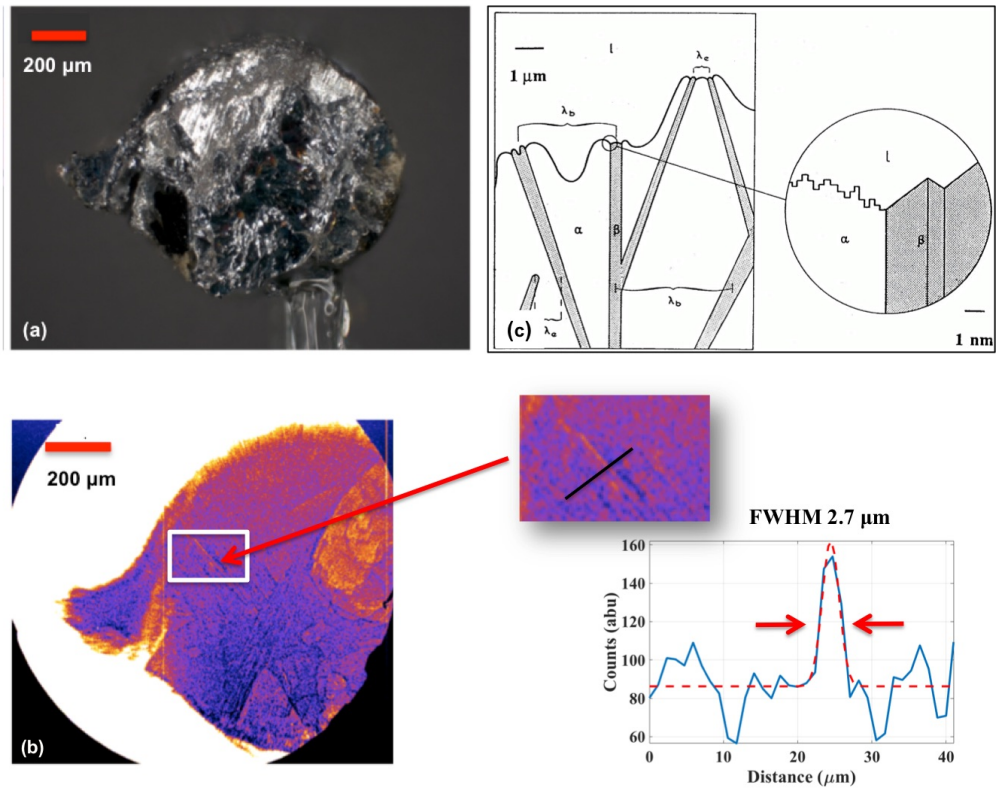

Figure 7.2: Al-Si sample investigated using a LWFA X-ray source. **a)** Optical microscope image of the Al-Si cylindrical sample imaged in LWFA experiments. **b)** X-ray phase contrast image obtained with a LWFA, revealing a lamellar microstructure with an interphase spacing on the order of 1 - 3 μm. A line-out from a region of interest in the phase contrast image is shown, indicating 2.7 $\pm 0.3\mu$m as an upper bound on the resolving power of this method. **c)** A schematic showing growth of irregular eutectics where β represents the faceted phase (e.g., Si), α is the non-faceted, higher volume fraction phase (e.g., Al), and l is the melt ahead of the interface. The microstructure is deemed irregular due to the difficulty or stiffness in changing the growth direction of the faceted phase. The inset shows the atomically diffuse α phase and the defect growth mechanism for the faceted β phase. Retrieved with permission from Ref. FISHER

alloys were cast in the exact same manner, and thus have comparable lamellar spacings [43]. For both experiments, the samples were machined into cylindrical samples of 1 mm thickness.

7.3 Results and Analysis

A microscope image of the 1 mm diameter machined sample is shown in Figure 7.2a) alongside an example image of the Al-Si microstructure obtained using X-rays

from a LWFA in Figure 7.2b). The LWFA projection image was obtained using a nearly 22 $\times$ magnification, and the banded or lamellar structure can be observed in the zoomed-in image, from which a line-out indicates that the LWFA source is successfully resolving features smaller than 3 μm. The resolution of these images is determined by the geometry of the imaging system, as discussed below. The observed microstructure is consistent with that predicted for irregular eutectics, in which the lamellar spacing can be as fine as 1 μm (Figure 7.2c)). In this idealized schematic, the faceted phase β (e.g., Si) and the non-faceted phase α (e.g., Al) are shown, growing in a non-periodic manner into the liquid.

7.3.1 Comparison of image quality

The quality of the SLS and LWFA projection images were compared according to two metrics: image sharpness and resolution. Image sharpness is closely related to the fineness of the resolvable details in an image (X-ray projection microscopic images in this case). This analysis was conducted by Dr. Nancy Senabuyla (University of Michigan).

The SLS projection image was normalized according to the standard procedure for synchrotron experiments using dark images and flat-field corrections as follows:

(7.1)

$$\text{Normalized SLS image} = \frac{((\text{Raw SLS projection image}) - (\text{average of 21 dark shots}))}{((\text{average of 51 flat shots}) - (\text{average of 21 dark shots}))}$$

No such normalizations were applied to LWFA images.

An algorithm developed by Shaked and Tastl [143] was used to determine the overall sharpness of an image. Here, their global single parameter sharpness model is used, implemented as the ratio between the output energy of an ideal high pass

filter and an ideal band pass filter, [143] and described by

$$\text{Sharpness} = \frac{\int_{\bar{\xi}\epsilon H} |M(\bar{\xi})|^2 d\bar{\xi}}{\int_{\bar{\xi}\epsilon B} |M(\bar{\xi})|^2 d\bar{\xi}} \tag{7.2}$$

where the image is indicated by $m(x, y)$ and the Fourier transform of the image by $F(m) = M(\xi_x, \xi_y)$, the Cartesian frequency coordinates are defined as $\bar{\xi} = (\xi_x, \xi_y)$, and H and B are the high and low-band pass frequency ranges, respectively. The images were initially resized to match the dissimilar pixel resolutions (0.74 μm and 0.61 μm for SLS and LWFA experiments, respectively), and the intensity histogram in each image was scaled to lie within the same intensity range. Subsequently, a 2D high pass filter and 2D band pass filter were applied to the 2D Fourier transform of each image matrix and the image sharpness was calculated according to equation (7.2).

A Fourier-based spatial resolution criterion[144] was used to compare the sharpness of projection images obtained *via* a laser-wakefield accelerator system and the TOMCAT beamline at the Swiss Light Source. The power spectral density (PSD) profiles of lines arbitrarily drawn within the projection image at angles ranging from 0° to 90° with the horizon are computed. This was done to ensure that the power spectral density over all pixel directions in the projection images were statistically represented. The PSD values was then projected onto polar plots to reveal the power spectral distribution at varying angular positions within the image. The PSD converges to a value defined as the "noise baseline" obtained in our calculations by taking the mean of the last fifty (50) power spectral density elements in the array of PSDs. According to the criterion put forward by Ref [144], spatial resolution is computed by taking twice the value of the PSD at the noise baseline, and matching this value to the corresponding maximum spatial frequency, k_{res} [144]. The spatial

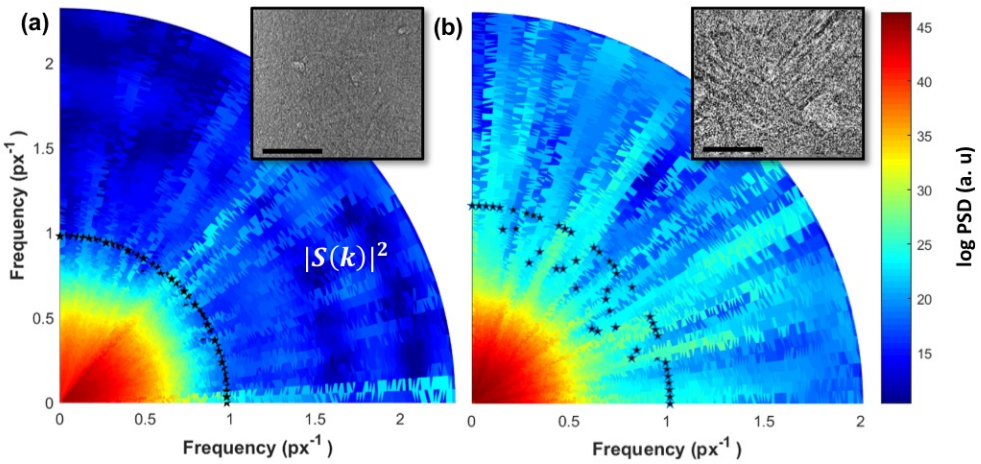

Figure 7.3: Measurement of the spatial resolution criterion for line profiles oriented from 0° to 90°. The spatial resolution criterion is projected onto polar plots in **a)** SLS and **b)** LWFA projection images. Projection images are shown as insets. $|S(k)|^2$ is the spectral power of the detected signal. Raw images were resized to match the dissimilar pixel resolutions for SLS and LWFA images, and PSD analysis was performed on projection images with equalized intensity histograms. For both cases, spatial frequencies are given in units of inverse pixels. The LWFA projection image has a spatial resolution that is comparable to the spatial resolution in the SLS projection image, as evidenced by the close to equal k_{res} values of 1.017 ± 0.01 px^{-1} and 0.98 ± 0.01 px^{-1} in the LWFA and SLS images, respectively. Stars represent the k_{res} spatial frequency value obtained along an arbitrary line in the projection image. Scale bar measures 70 μm.

resolution x_{res} is related to the wave-number k_{res} by:

$$x_{res} = \frac{2\pi}{k_{res}} \tag{7.3}$$

In this analysis, image quality was computed for the interior regions of phase contrast images to compare areas of highest resolution.

Normalized sharpness estimates given in arbitrary units (1 ± 0.05 a.u. and 0.62 ± 0.05 a.u. for LWFA and SLS projection images, respectively) show that the LWFA projection images are comparable to the sharpness of projection images obtained at SLS. In addition, Figure 7.3 shows the calculation of the spatial resolution, where $|S(k)|^2$ is the spectral power of the detected signal and k_{res} is the maximum spatial frequency when the spectral power is twice the noise level. The power spectral density (PSD) conveys the strength of the intensity variation in the image pixels as a function

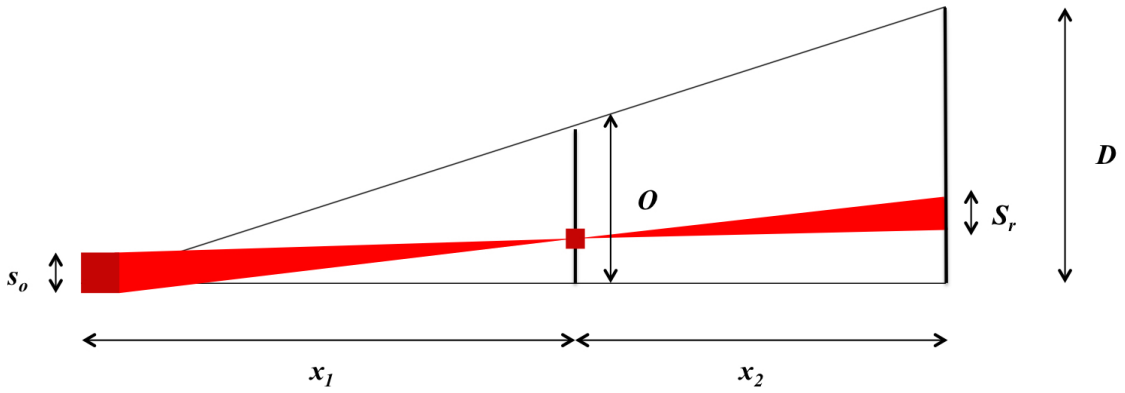

Figure 7.4: Geometric layout of an X-ray illumination setup without optics. The distance from the source, s_o to the object, O, is x_1, and the distance from the object to the detector, D, is x_2.

of frequency; it indicates the frequencies at which intensity variations are strong and those at which the variations are weak. In other words, the high frequency wavenumber for the PSD in the LWFA image is related to sharper variations in intensity values of the pixels in the image domain. Such variations occur in pixels near to an object edge, e.g., between different lamellae in the Al-Si eutectic.

The PSD shown in Figure 7.3a) and Figure 7.3b) have been calculated for line profiles in the images taken using the TOMCAT beamline and *via* LWFA, respectively. It can be observed that the LWFA image has a spatial resolution x_{res} comparable to the spatial resolution in the SLS image. Figure 7.3b) shows a slightly higher autocorrelation at long wavelengths as evidenced by a higher k_{res} (1.017 ± 0.01) px^{-1} value compared to 0.98 ± 0.01 px^{-1} for the SLS image, where LWFA images have been rescaled to the effective pixel value for proper comparison. Errors in the measurement of image resolution arise from the absence of normalization by white- and dark-field images for the LWFA projections (Figure 7.3b)), which ultimately lead to intensity inhomogeneities on the detector plane.

7.3.2 Geometric resolution limits

The resolution limits of phase-contrast X-ray imaging experiments are set by the source size and the imaging geometry, which determines the magnification of the system, and the detector pixel size. For synchrotron beamlines, such as TOMCAT, the source size is much bigger than the desired resolution, but the distance from the source to the sample is typically much larger than the distance from the sample to the detector, effectively resulting in a large demagnification factor of the source size. Therefore, the effective pixel size of the detector (which includes the optical magnification provided by the visible light microscope coupling the scintillator to the detector's imaging chip) is the limiting factor for high-resolution imaging, and needs to be minimized for the highest possible resolution. Conversely, for LWFA sources, where the source size is much smaller than the pixel size of the detector, the high magnification in the X-ray imaging geometry reduces the resolution requirements of the detector.

The resolution in a lens-less X-ray image setup is determined by the imaging geometry and the detector, as shown in Figure 7.4. For a source of size s_o at a distance of x_1 from an object, O, an image is formed at the detector, D. The distance from the object to the detector is x_2. In this configuration there are two limitations on the resolution dictated by source size and the detector resolution, both of which depend on the magnification of the system.

The geometric magnification of the system is related to the distances between the source and the object and the object and the detector using similar right angle triangles: $M = D/O = (x_1 + x_2)/x_1$. The transverse projection of a point in the object onto the detector determines the source-size limited resolution, $S_r = s_o x_2/x_1$. At the object plane, the resolution limit of the source is given by $S_r/M = s_o x_2/(x_1 +$

x_2). The resolution limit of the detector is set by the pixel size, p, and therefore the lower bound on detector resolution is $D_r = p/M = px_1/(x_1 + x_2)$. The total resolution, r, can be considered as the 2-norm of these limits [145]:

$$r = \left(\left(\frac{s_o x_2}{x_1 + x_2} \right)^2 + \left(\frac{p x_1}{x_1 + x_2} \right)^2 \right)^{1/2} \tag{7.4}$$

For high resolution phase contrast imaging, the conditions for detection of bright and dark phase contrast fringes are set by the detector resolution, and the bandwidth and size of the source [146]. The X-ray detector must have sufficient resolution to resolve separate fringes, where the fringe spacing is given by $z \simeq \sqrt{x_2 \lambda}$ where λ is taken to be the wavelength of the critical energy of the source, given in Table 7.1. Using the values in Table 7.1, it is clear that this condition is satisfied in both the SLS and LWFA experiments. The condition on the longitudinal coherence of the source is given by $\Delta\lambda/\lambda \ll 2$. These conditions are rather weak and therefore can be assumed to be automatically satisfied for both sources [146].

The final condition on the resolution of phase-contrast imaging is set by the lateral coherence of the source, or the source size. A finite source size can be considered as a pair of point sources, separated by a finite distance, y. These two sources will each produce fringes at the detector. The shift between these fringes can result in blurring and decreased resolution. The limit on the source size for resolving individual fringes is given by $y \ll x_1\sqrt{\lambda/x_2}$. The parameters above are tabulated for the SLS and the LWFA generated X-ray source in Table 7.1. From the limits on phase-contrast imaging an upper bound of 1 μm on the source size is obtained.

7.3.3 Image blurring due to betatron emission length

Beyond sharpness and resolution, another consideration in the practical application of LWFA for X-ray imaging is blurring due to the non-zero emission length of

	SLS	LWFA
Source size, FWHM (s_0):	127 μm (H) $\times$ 38 μm (V)	$<$ 2.7 μm (1 μm assumed)
Detector pixel size (p):	0.75 μm	13.5 μm
Source to sample (x_1):	2000 cm	19.3 cm
Sample to detector (x_2):	11 cm	410 cm
Magnification (M):	$\simeq$ 1.01	22.2
Source size limited resolution (S_r/M):	0.69 μm $\times$ 0.21 μm	0.96 μm
Detector resolution limit (p/M):	0.74 μm	0.61 μm
Total geometric resolution (r):	1.0 μm $\times$ 0.76 μm	1.1 μm
Phase contrast detector limit (z):	2.2 μm	21 μm
Critical energy (E_c):	28 keV	11.2 keV
Wavelength (λ):	4.4×10^{-11} m	1.1×10^{-10} m
Phase contrast source size limit (y):	$\ll$400 μm	$\ll$1 μm

Table 7.1: Comparison of resolution limits in X-ray imaging between the Swiss Light Source (SLS) and LWFA X-ray sources generated using the Gemini Laser at the Rutherford Appleton Lab (RAL). Errors on all measurements are approximately 10%.

the betatron source [147]. Betatron emission is highest at the location of high energy electrons, yielding a very small source size on the order of a few μm[16]. However, the emission length of a betatron source has been found to extend a few millimeters along the axis of laser propagation, resulting in blurring in X-ray images and decreased resolution [147, 148]. This blurring can be observed in Figure 7.5, where the image resolution is highest near the central axis of the X-ray beam (circled) and begins to blur towards the edges of the sample. It has also been found that the betatron emission length tends to increase with increasing plasma length [148], therefore longer plasma lengths are associated with lower resolution away from the central axis of the laser beam. Additionally, instability in beam pointing can result in variation of the location of highest resolution. For a plasma cell of length 15.5 mm, as employed in these experiments, the emission length of the betatron source was found to be on the order of 5 mm. Image blurring is also a challenge with conventional synchrotron sources, where the emission length can be much longer ($\sim$m), versus $\sim$mm for a LWFA source. However, the large divergence of the LWFA source makes this a concern when the full beam size is used for imaging. It is also important to note that

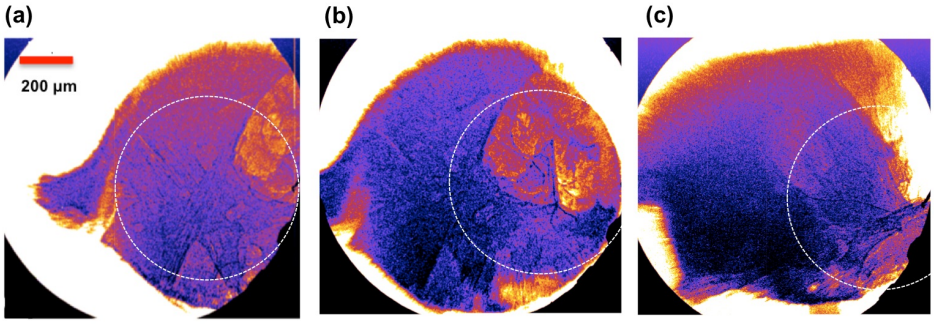

Figure 7.5: Blurring of LWFA X-ray images due to finite betatron emission length. Three LWFA phase contrast images of the Al-Si sample are shown. In **a)** and **b)** the sample is at the same orientation perpendicular to the laser axis. In image **b)** the sample has been translated horizontally by approximately 30 μm. In **c)** the sample has been rotated by 90 degrees about the vertical axis. Regions of sharpest resolution are circled with a dotted line, with a radius of approximately 600 μm at highest focus. In all images, blurring can be observed on the order of a millimeter away from the central point due to the emission length of the betatron source. Highest resolution imaging is obtained along the axis of the electron beam; only this section of the image is used for resolution analysis. Blurring due to the emission length of the X-ray source is not unique to betatron sources, also occurring with conventional synchrotron beams, but is exacerbated by high magnification in cases where the full beam is used for imaging.

blurring due to the emission length is exacerbated by high magnification. Therefore, the relationship between plasma length and emission can inform optimization of the LWFA X-ray source for high resolution imaging.

7.3.4 Critical energy of the betatron source

For high contrast imaging of features in dense materials the critical energy of the X-ray beam must be on the order of several keV. In this experiment, the critical energy of the resultant X-ray beam is determined by comparing the transmission through an array of different elemental filters. The critical energy as a function of plasma density was found to increase with increasing plasma density, as shown in Figure 7.6a), reaching a maximum critical energy of nearly 10 keV. These results indicate that LWFA X-ray sources can provide a tunable X-ray source for phase contrast imaging.

The critical photon energy of a LWFA source is related to the maximum energy of the electron beam, γ, and the plasma density, n_p, by [63, 149, 77]:

$$E_c = \frac{3}{2}\hbar\omega_\beta K\gamma^2 = \frac{3}{4}\hbar\frac{e^2}{\epsilon_0 m_e c}\frac{\sigma}{2}n_p\gamma^2 \tag{7.5}$$

where $\sigma = 2r_\beta$ is the approximate betatron source size and r_β is the amplitude of betatron oscillations. From equation (7.5), one can see that the electron energy can be retrieved from the measured critical photon energy, the plasma density n_p and an assumed source size σ using $\gamma \propto \sqrt{2E_c/n_p\sigma}$. Figure 7.6b) shows the retrieved electron energies with measured plasma densities and fitted source size σ of (0.2 - 1 μm). A plot of the experimentally measured peak electron energy is superimposed on retrieved electron energies, showing best agreement between theory and experimental data for betatron source size on the order of (0.4 - 1.0) μm.

For comparison with experimental results it is important to note that the critical photon energy in equation (7.5) is mainly determined by the maximum electron energy achieved during acceleration because of the γ^2 scaling. Therefore, the retrieved electron energies represent the maximum electron energies during the acceleration, which are not necessarily the same as those measured from the experiment. This is because for high plasma density (here, $n_p > 1.2 \times 10^{18}\text{cm}^{-3}$) the dephasing length is shorter than the gas cell length and electron beams will experience dephasing. Currently, information about electron dephasing cannot be captured experimentally in a single shot, however novel techniques employing a transverse density gradient may provide single-shot diagnostic information of the temporal evolution of the betatron X-ray spectrum and electron acceleration [150].

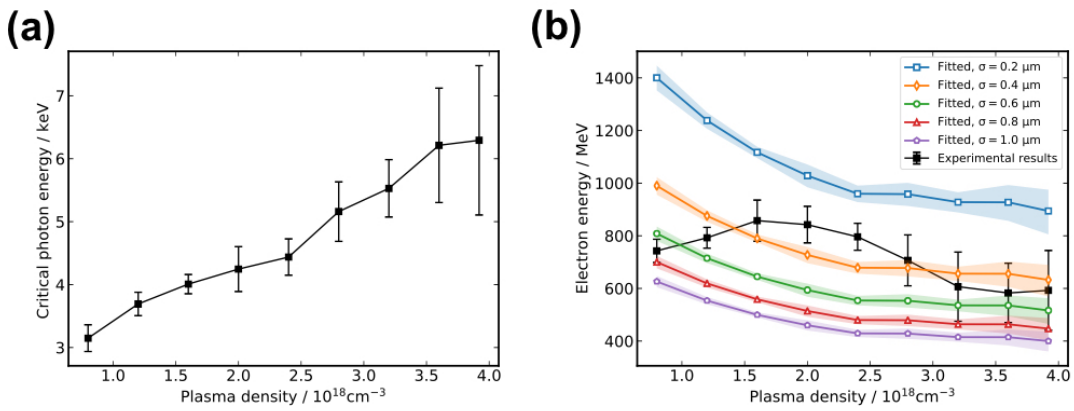

Figure 7.6: Critical energy of the LWFA betatron source. **a)** Experimentally measured critical energy of the LWFA X-ray beam as a function of plasma density. **b)** Theoretical predictions of the maximum electron energy corresponding to experimentally measured critical energy, shown for betatron source sizes of (0.2 - 1.0) μm along with experimentally measured maximum electron energies in the resultant LWFA beam (black).

7.4 Discussion and conclusions

Thus far, Al-Si eutectics have only been investigated *via* conventional synchrotron-based phase contrast tomography (PCT)[151, 152, 153]. PCT enables the study of weakly absorbing samples, as well as materials systems consisting of elements with similar atomic numbers. This is because variations in the real valued refractive index are several orders of magnitude larger than the imaginary component [154, 146]. In order to recover the microstructure from projection images obtained *via* PCT, phase-retrieval algorithms are first applied to the projection images [155, 156]. Subsequently, a projection algorithm (*e.g., filtered back projection[157]*) is used to reconstruct a three-dimensional (3D) map of the refractive index decrement (i.e., the difference between the sample's index of refraction and that of air). Image segmentation of the PCT reconstructions is crucial for quantitative analysis of interfacial properties, *e.g.*, orientations, velocities, curvatures, and n-point statistics [158, 159]. However, sharp images taken at high resolution with sufficient contrast, such as

those obtained with a LWFA source, can mitigate the challenges associated with low pass characteristics in projection images and in turn ease the data analysis process down-stream [160, 161, 151].

From the projection images obtained in the LWFA experiment the microstructural details can be measured straightaway and throughout the sample volume owing to the fact that the projection images were reasonably sharp. In particular, the spacing between neighboring Si lamellae was measured to be between 10 and 90 μm. Using the Jackson-Hunt relationships modified for irregular eutectics [132, 162, 163, 134], the average lamellar spacing was correlated with an average growth rate and undercooling, estimated to be 0.35 $\pm$ 0.3 μm/s and 0.13 $\pm$ 0.03 K, respectively [43].

A comparison of experimental parameters used in the SLS and LWFA experiments presented here indicates that these sources have comparable geometric resolution limits, and both satisfy the criteria for fringe detection. However, our analysis of the projection images shown in Figure 7.3 indicates that the LWFA source has slightly greater sharpness and spatial resolution for these conditions and is able to resolve micrometer-scale lamellar features. The reason for resolution loss in the SLS projection image is likely due to vibrations in the experimental setup. At the time of the experiments, the relative sample to detector position could vibrate at an amplitude of up to 0.5 - 1 μm consequently resulting in a blurring of the projection images over the 500 milliseconds exposure time. Conversely, although LWFA experiments are prone to similar instabilities, the femtosecond timescale of the betatron source enables ultra-fast imaging. Therefore, single-shot LWFA images are not subject to motion blur. In this way, the visibility of small-scale features such as lamellae is enhanced. It is also worth noting that the conditions for detecting phase contrast fringes for the LWFA experiments set an upper bound of 1 μm on the source size (see

Table 7.1), indicating that betatron sources may be much smaller than previously noted.

These results indicate that betatron X-rays from LWFA can be competitive with conventional synchrotron sources for the characterization of eutectic alloys and solid density materials. This opens the door to high-resolution materials diagnostics using laser-based sources, without needing to visit a synchrotron facility. Indeed, projection images of the Al-Si sample obtained using LWFA betatron X-rays were of comparable sharpness and spatial resolution to projection images obtained at SLS. Fine details of the lamellar microstructure were clearly resolved in LWFA projection images (Figure 3b) inset), indicating an upper bound of 2.7 μm on the resolving power of this method. Furthermore, the phase contrast spatial resolution criteria indicate that the LWFA source size may be much smaller than a micrometer, which is corroborated by the theoretical scaling of the betatron energy with plasma density in Figure 7.6b) in which the retrieved electron energy was most closely fit assuming betatron source sizes on the order of (0.4 - 1) μm. However, it is important to note that the enhanced spatial resolution reported here is specific to the experimental conditions of these experiments, and that neither of the two experiments was optimized to obtain the ultimate spatial resolution. The ultra-short exposure time of betatron sources may also provide improved spatial resolution by enabling imaging on a timescale shorter than the frequency of vibrations in experimental setups.

CHAPTER VIII

Conclusions and future work

8.1 Summary

In this dissertation, four experiments are presented on electron acceleration and radiation production using relativistic intensity laser pulses. This work explores optimization of DLA, as well as the role of bubble formation in infrared radiation and the diagnosis of bubble dynamics using stimulated Raman backscattering. The first comparison between betatron radiation from an LWFA and synchrotron radiation from a conventional acceleration is also presented.

The experiments presented in Chapter IV demonstrate an optimal plasma density for DLA, resulting in electron beams with energies up to 600 MeV. There beams were also found to be of high charge (10s of nC), but of reasonably high divergence (65 mrad). Experimental measurements were in good agreement with PIC simulations. Additionally, the existence of a threshold density for a fixed a_0 was in good agreement theoretical predictions. PIC simulation work designed to match the parameters of the OMEGA EP laser reveals that stable channel formation results from a balance

between self-focusing and filamentation. At low densities, surface wave production was reduced, which may prevent pre-acceleration and injection of plasma electrons. Tracking of individual electrons confirmed DLA as the dominant acceleration mechanism and revealed regular betatron oscillations of the highest energy electrons at the highest density. These oscillations indicate that high-energy X-ray sources may also be produced during DLA. Further investigations into the role of pulse duration on DLA using 2D PIC simulations indicate the total charge of DLA electron beams of energetic electrons can be significantly enhanced by using longer pulses.

In Chapter V, infrared radiation produced by spectral broadening of the laser pulse in an LWFA was shown to be highly dependent on laser and plasma conditions. The use of a tailored density plasma target, consisting of a long low density stage followed up a high density step, was found to increase spectral broading, shifting the laser frequency to longer wavelengths. Increased plasma density in the short, high-density cell was associated with enhanced broadening, however the intensity of the infrared pulse dropped significantly when the density was high enough to induce bubble collapse. Measurements of the total energy in the infrared beam exceeded 10 mJ, and measurements of the beam profile indicate at high plasma density spatially uniform infrared beams can be produced. Under certain conditions, infrared spectra centered on a specific wavelength could be produced, however it was not clear which combination of laser and plasma parameters enabled control of spectral features. A sensitivity analysis using co-variance matrices and applying the Pearson Correlation Coefficient indicated that laser power, plasma length and the density of the plasma step played the greatest role in generating wavelengths between 2 - 2.4 μm. 2D PIC simulations indicate that the interaction between long wavelengths, which lag being the driving laser pulse, and accelerated electron beams can result in scattering

and further up-shifting of the laser pulse. An increase in spectral broadening was associated with a decrease in electron energy.

In Chapter VI, the first experimental measurements of backward strongly coupled SRS in the bubble regime of LWFA were presented. In these experiments, the spectra of backscattered light was dramatically broadened and highly modulated. For laser powers at and above 100 TW, the BSRS signal was found to increase with both electron charge and plasma density, although no such correlation were observed at lower powers. Experimentally observed spectral characteristics were reproduced in 2D PIC simulations. Additionally, a correlation between BSRS signal and plasma electron density within the laser wakefield bubble was observed in simulations. As the laser intensity was increased, the intensity and duration of the BSRS signal decreased until the electron bubble was fully evacuated. These results indicate that at highest powers (100 TW and above), the bursting, broadening and modulation of the BSRS frequency spectrum is associated with increased plasma density within the LWFA plasma bubble. Charge can become trapped in the plasma bubble through electron injection, therefore the observed correlation is likely due to density fluctuations in the plasma, associated with this phenomena and seeding the BSRS instability. Therefore, it is possible that fluctuations due to BSRS can provide feedback for electron injection.

Finally, in Chapter VII, the spatial resolution and sharpness of X-ray images obtained using LWFA and conventional accelerator sources were compared. These results indicate that betatron X-rays from LWFA can provide an alternative to conventional synchrotron sources for high resolution imaging of eutectics and, more broadly, complex microstructures. An upper bound on the resolving power of 2.7 $\pm$ 0.3 μm of the LWFA betatron source was determined.

8.2 Future work

In Chapter IV, the considerable acceleration and deceleration of DLA electrons observed in 2D PIC simmulations indicates that this process can be an efficient X-ray source. In fact, previous work has indicated that the betatron oscillations of DLA electrons are of higher amplitude than in the wakefield regime, which could result in higher energy X-ray sources. The characterization of this radiation is an important step in the development of hard, pulsed X-ray sources for advanced imaging of dense plasma relevant to inertial confinement fusion and high-energy-density physics. Additionally, the OMEGA EP laser beam was found to refract away from the plasma target, due to density gradients in the plasma. This resulted in the electron beam moving off of the laser axis, and therefore no longer being centered on the magnetic spectrometer. Therefore, it is unlikely that the highest energy electrons were measured on the electron spectrometer. This deflection of the laser beam might be minimized by using plasma targets with more shallow density gradients, such as those produced using a gas jet. Electron acceleration could also be enhanced using a chromatic focusing system to produce a co-propagating or "flying focus" [164]. Finally, although good qualitative agreement between experimental results and 2D PIC simulations was obtained, important physics of the DLA process, such as self-focusing and parametric amplification of electron energy through transverse oscillations, are not properly captured in this space. While 3D simulations would be ideal, quasi-3D simulations, which capture many dominant 3D phenomena through the inclusion of azimuthal harmonics, could be performed to elucidate the impact of this physics on electron acceleration and channel formation.

The infrared spectra measured in from an LWFA in Chapter V were found to be

highly dependent on laser power, plasma length and plasma density. While density tailoring enhanced spectral broadening, the generation of quasi-monochromatic infrared pulses was not found to depend on a single parameter. The sensitivity analysis performed on this data indicates that further study on the role of laser and plasma conditions on plasma wave formation and morphology, and associated changes to the refractive index, is required. These studies are best suited to high-repetition rate laser systems, where the tunability of these sources could be investigated using adaptive control algorithms. Additionally, while the infrared radiation was only measured along the axis of laser propagation in these experiments, 2D simulations suggest that long wavelength radiation measured at different angles may serve as a diagnostic of the interaction between long-wavelength laser light and the accelerated electron beam.

In Chapter VI, BSRS radiation was found to be broader and more pronounced than any previously observed in the cases where a high charge electron beam was accelerated using laser powers higher than 100 TW. The temporal nature of this radiation, ceasing with evacuation of charge in the plasma bubble, indicates that BSRS may serve as a diagnostic of bubble formation, but also that BSRS can be enhanced or turned off. Significant enhancement of backward scattered photons could be used to generate MeV level X-ray sources through inverse-Compton scattering. The ability to diagnose the formation of an empty bubble cavity could also be used to optimized infrared radiation (where spectral broadening was found to decrease in the blow-out regime).

The realization of high-repetition rate laser drivers for LWFA [165, 166, 167], combined with the micrometer-scale spatial resolution demonstrated in Chapter VII, could enable dynamic measurements on an ultra-short timescale. These sources

would have myriad of applications, from in vivo imaging of physiological processes, to probing of phase changes in materials under extreme conditions.

BIBLIOGRAPHY

[1] JD Cockcroft and ETS Walton. Artificial Production of Fast Protons. *Nature*, 129(3250):242–242, 1932.

[2] G Ising. Prinzip einer Methode zur Herstellung von Kanalstrahlen hoher Voltzahl. *Prinzip einer Methode zur Herstellung von Kanalstrahlen hoher Voltzahl*, 30(18):1–4, 1924.

[3] PJ Bryant. A Brief history and review of accelerators, 1992.

[4] D Strickland and G Mourou. Compression of amplified chirped optical pulses. *Optics Communications*, 55(6):447–449, 1985.

[5] V Yanovsky, V Chvykov, G Kalinchenko, P Rousseau, T Planchon, T Matsuoka, A Maksimchuk, J Nees, G Cheriaux, G Mourou, and K Krushelnick. Ultra-high intensity-300-tw laser at 0.1 hz repetition rate. *Optics Express*, 16(3):2109–2114, 2008.

[6] T Tajima and JM Dawson. Laser Electron Accelerator. *Physical Review Letters*, 43(4):267–270, 1979.

[7] E Esarey, CB Schroeder, and WP Leemans. Physics of laser-driven plasma-based electron accelerators. *Reviews of Modern Physics*, 81(1229):1229–1285, 2009.

[8] WP Leemans, B Nagler, AJ Gonsalves, Cs Tóth, K Nakamura, CGR Geddes, E Esarey, CB Schroeder, and SM Hooker. Gev electron beams froma centimetre-scale accelerator. *Nature Physics*, 2:696–699, 2006.

[9] Wang X, R Zgadzaj, N Fazel, Z Li, SA Yi, X Zhang, W Henderson, YY Change, R Korzekwa, CH Pai, H Quevedo, G Dyer, E Gaul, M Martinez, AC Bernstein, T Borger, M Spinks, M Donovan, V Khudik, G Shevts, T Ditmire, and MC Downer. Quasi-monoenergetic laser-plasma acceleration of electrons to 2 gev. *Nature Communications*, 4(1988), 2013.

[10] AJ Gonsalves, K Nakamura, J Daniels, C Benedetti, C Pieronek, TCH de Raadt, S Steinke, JH Bin, SS Bulanov, J van Tilborg, CGR Geddes, CB Schroeder, Cs Toth, E Esarey, K Swanson, L Fan-Chiang, G Bagdasarov, N Bobrova, V Gasilov, G Korn, P Sasorov, and WP Leemans. Petawatt laser guiding and electron beam acceleration to 8 gev in a laser-heated capillary discharge waveguide. *Physical Review Letters*, 122(8):084801, 2019.

[11] F Albert, AGR Thomas, SPD Mangles, S Banerjee, S Corde, A Flacco, M Litos, D Neely, J Vieira, Z Najmudin, R Bingham, C Joshi, and T Katsouleas. Laser wakefield accelerator based light sources: potential applications and requirements. *Plasma Physics and Controlled Fusion*, 56(8):084015, 2014.

[12] SPD Mangles, CD Murpher, Z Najmudin, AGR Thomas, JL Collier, AE Dangor, EJ Divall, PS Foster, JG Gallacher, CJ Hooker, DA Jaroszynski, AJ Langley, WB Mori, PA Norreys, FS Tsung, R Viskup, BR Walton, and K Krushelnick. Monoenergetic beams of relativistic electrons from intense laser-plasma interactions. *Nature*, 431:535–538, 2004.

[13] J. Faure, Y. Glinec, A. Pukhov, S. Kiselev, S. Gordienko, E. Lefebvre, J.-P. Rousseau, F. Burgy, and V. Malka. A laser-plasma accelerator producing monoenergic electron beams. *Nature*, 431:541–544, 2004.

[14] CGR Geddes, CS Toth, J van Tilborg, E Esarey, CB Schoreder, D Bruhwiler, C Nieter, J Cary, and WP Leemans. High-quality electron beams from a laser wakefield accelerator using plasma-channel guiding. *Nature*, 431:538–541, 2004.

[15] A Rousse, K Ta Phuoc, R Shah, A Pukhov, E Lefebvre, V Malka, S Kiselev, F Burgy, J-P Rousseau, D Umstadter, and file = :Users/amina/Dropbox/Mendeley/Mendeley Desktop/Rouse_SynchrotronLWFA_PRL_2004.pdf:pdf issn = 0031-9007 journal = Physical Review Letters month = number = 13 pages = 135005 publisher = American Physical Society title = Production of a keV X-Ray beam from synchrotron radiation in relativistic laser-plasma interaction volume = 93 year = 2004 Hulin, D.

[16] S Kneip, C Mcguffey, J L Martins, S F Martins, C Bellei, V Chvykov, F Dollar, R Fonseca, C Huntington, G Kalintchenko, A Maksimchuk, S P D Mangles, T Matsuoka, S R Nagel, C A J Palmer, J Schreiber, K Ta Phuoc, A G R Thomas, V Yanovsky, L O Silva, K Krushelnick, and Z Najmudin. Bright spatially coherent synchrotron X-rays from a table-top source. *Nature Physics*, 6(12):980–983, 2010.

[17] F Albert and AGR Thomas. Applications of laser wakefield accelerator-based light sources. *Plasma Phys. Control. Fusion*, 58(103001), 2016.

[18] S Fourmaux, S Corde, K Ta Phuoc, P Lassonde, G Lebrun, S Payeur, Frédérique Martin, Stéphane Sebban, Victor Malka, Antoine Rousse, and JC Kieffer. Single shot phase contrast imaging using laser-produced betatron x-ray beams. *Optics Letters*, 36(13):2426–2428, 2011.

[19] J Wenz, S Schleede, K Khrennikov, M Bech, P Thibault, M Heigoldt, F Pfeiffer, and S Karsch. Quantitative x-ray phase-contrast microtomography from a compact laser-driven betatron source. *Nature Communications*, 6:7568, 2015.

[20] JM Cole, JC Wood, NC Lopes, K Poder, RL Abel, S Alatabi, JSJ Bryant, A Jin, S Kneip, K Mecseki, DR Symes, SPD Mangles, and Z Najmudin. Laser-wakefield accelerators as hard x-ray sources for 3D medical imaging of human bone. *Scientific Reports*, 5, 2015.

[21] JC Wood, DJ Chapman, K Poder, NC Lopes, ME Rutherford, TG White, F Albert, KT Behm, N Booth, JSJ Bryant, PS Foster, S Glener, E Hill, K Krushelnick, Z Najmudin, BB Pollock, S Rose, W Schumaker, RHH Scott, M Sherlock, AGR Thomas, Z Zhao, DE Eakins, and SPD Mangles. Ultrafast imaging of laser driven shock waves using betatron x-rays from a laser wakefield accelerator. *Scientific Reports*, 8(1):11010, 2018.

[22] JM Cole, DR Symes, NC Lopes, JC Wood, K Poder, S Alatabi, SW Botchway, PS Foster, S Gratton, S Johnson, C Kamperidis, O Kononenko, M De Lazzari, CAJ Palmer, D Rusby, J Sanderson, M Sandholzer, G Sarri, Z Szoke-Kovacs, L Teboul, JM Thompson, JR Warwick, H Westerberg, MA Hill, DP Norris, SPD Mangles, and Z Najmudin. High-resolution μCT of a mouse embryo using a compact laser-driven X-ray betatron source. *Proceedings of the National Academy of Sciences*, page 201802314, 2018.

[23] F Albert, BB Pollock, JL Shaw, KA Marsh, JE Ralph, Y-H Chen, D Alessi, A Pak, CE Clayton, SH Glenzer, and C Joshi. Angular dependence of betatron x-ray spectra from a laser-wakefield accelerator. *Physical Review Letters*, 111(23):235004, 2013.

[24] B Mahieu, N Jourdain, K Ta Phuoc, F Dorchies, J-P Goddet, A Lifschitz, P Renaudin, and L Lecherbourg. Probing warm dense matter using femtosecond x-ray absorption spectroscopy with a laser-produced betatron source. *Nature Communications*, 9(1):3276, 2018.

[25] A Modena, Z Najmudin, AE Dangor, CE Clayton, KA Marsh, C Joshi, Victor Malka, CB Darrow, C Danson, D Neely, and FN Walsh. Electron acceleration from the breaking of relativistic plasma waves. *Nature*, 377(6550):606, 1995.

[26] Z Najmudin, K Krushelnick, EL Clark, SPD Mangles, B Walton, AE Dangor, S Fritzler, Victor Malka, E Lefebvre, D Gordon, FS Tsung, and C Joshi. Self-modulated wakefield and forced laser wakefield acceleration of electrons. *Physics of Plasmas*, 10(5):2071–2077, 2003.

[27] F Albert, N Lemos, JL Shaw, BB Pollock, C Goyon, W Schumaker, AM Saunders, KA Marsh, A Pak, JE Ralph, JL Martins, LD Amorim, RW Falcone, SH Glenzer, JD Moody, and C Joshi. Observation of betatron x-ray radiation in a self-modulated laser wakefield accelerator driven with picosecond laser pulses. *Physical review letters*, 118(13):134801, 2017.

[28] P Mora and TM Antonsen Jr. Electron cavitation and acceleration in the wake of an ultraintense, self-focused laser pulse. *Physical Review E*, 53(3):R2068, 1996.

[29] MIK Santala, Z Najmudin, EL Clark, M Tatarakis, K Krushelnick, AE Dangor, Victor Malka, Jérôme Faure, R Allott, and RJ Clarke. Observation of a hot high-current electron beam from a self-modulated laser wakefield accelerator. *Physical review letters*, 86(7):1227, 2001.

[30] CE Clayton, KC Tzeng, D Gordon, P Muggli, WB Mori, C Joshi, V Malka, Z Najmudin, A Modena, and AE Dangor. Plasma wave generation in a self-focused channel of a relativistically intense laser pulse. *Physical Review Letters*, 81:100, 1998.

[31] JE Ralph, CE Clayton, F Albert, BB Pollock, SF Martins, AE Pak, KA Marsh, JL Shaw, A Till, JP Palastro, W Lu, SH Glenzer, LO Silva, WB Mori, C Joshi, and DH Froula. Laser wakefield acceleration at reduced density in the self-guided regime. *Physics of Plasmas*, 17(5):056709, 2010.

[32] N Lemos, F Albert, JL Shaw, D Papp, R Polanek, P King, AL Milder, KA Marsh, A Pak, BB Pollock, BM Hegelich, JD Moody, R Tommasini, GJ Williams, H Chen, and C Joshi. Bremsstrahlung hard x-ray source driven by an electron beam from a self-modulated laser wakefield accelerator. *Plasma Physics and Controlled Fusion*, 60(5):054008, 2018.

[33] SM Hooker. Developments in laser-driven plasma accelerators. *Nature Photonics*, 7(10):775, 2013.

[34] A Pukhov and J Meyer-ter Vehn. Relativistic laser-plasma interaction by multi-dimensional particle-in-cell simulations. *Physics of Plasmas*, 5(5):1880–1886, 1998.

[35] A Pukhov, Z-M Sheng, and J Meyer-ter Vehn. Particle acceleration in relativistic laser channels. *Physics of Plasmas*, 6(7):2847–2854, 1999.

[36] C Gahn, GD Tsakiris, A Pukhov, J Meyer-ter Vehn, G Pretzler, P Thirolf, D Habs, and KJ Witte. Multi-mev electron beam generation by direct laser acceleration in high-density plasma channels. *Physical Review Letters*, 83(23):4772, 1999.

[37] S. P.D. Mangles, B. R. Walton, M. Tzoufras, Z. Najmudin, R. J. Clarke, A. E. Dangor, R. G. Evans, S. Fritzler, A. Gopal, C. Hernandez-Gomez, W. B. Mori, W. Rozmus, M. Tatarakis, A. G.R. Thomas, F. S. Tsung, M. S. Wei, and K. Krushelnick. Electron acceleration in cavitated channels formed by a petawatt laser in low-density plasma. *Physical Review Letters*, 94(24):245001, jun 2005.

[38] L Willingale, AGR Thomas, PM Nilson, H Chen, J Cobble, RS Craxton, A Maksimchuk, PA Norreys, TC Sangster, RHH Scott, C Stoeckl, C Zulick, and K Krushelnick. Surface waves and electron acceleration from high-power, kilojoule-class laser interactions with underdense plasma. *New Journal of Physics*, 15(2):025023, 2013.

[39] S Kneip, SR Nagel, C Bellei, N Bourgeois, AE Dangor, A Gopal, R Heathcote, SPD Mangles, JR Marques, A Maksimchuk, PM Nilson, K Ta Phuoc, S Reed, M Tzoufras, FS Tsung, L Willingale, WB Mori, A Rousse, K Krushelnick, and Z Najmudin. Observation of synchrotron radiation from electrons accelerated in a petawatt-laser-generated plasma cavity. *Physical Review Letters*, 100(10):105006, 2008.

[40] H Chen, SC Wilks, JD Bonlie, EP Liang, J Myatt, DF Price, DD Meyerhofer, and P Beiersdorfer. Relativistic positron creation using ultraintense short pulse lasers. *Physical review letters*, 102(10):105001, 2009.

[41] M Vranic, RA Fonseca, and LO Silva. Extremely intense laser-based electron acceleration in a plasma channel. *Plasma Physics and Controlled Fusion*, 60(3):034002, 2018.

[42] OJ Pike, F Mackenroth, EG Hill, and SJ Rose. A photon–photon collider in a vacuum hohlraum. *Nature Photonics*, 8(6):434, 2014.

[43] AE Hussein, N Senabulya, Y Ma, MJV Streeter, B Kettle, SJD Dann, F Albert, N Bourgeois, S Cipiccia, JM Cole, O Finlay, E Gerstmayr, I Gallardo Gonzalez, A Higginbotham, DA Jaroszynski, K Falk, K Krushelnick, N Lemos, NC Lopes, C Lumsdon, O Lundh, SPD Mangles, Z Najmudin, PP Rajeev, CM Schleputz, M Shahzad, M Smid, R Spesyvtsev, DR Symes, G Vieux, L Willingale, JC Wood, AJ Shahani, and AGR Thoams. Laser-wakefield accelerators for high-resolution x-ray imaging of complex microstructures. *Scientific reports*, 9(1):3249, 2019.

[44] F Albert and AGR Thomas. Applications of laser wakefield accelerator-based light sources. *Plasma Physics and Controlled Fusion*, 58(10):103001, 2016.

[45] S Chen, ND Powers, I Ghebregziabher, CM Maharjan, C Liu, G Golovin, S Banerjee, J Zhang, N Cunningham, A Moorti, S Clarke, S Pozzi, and DP Umstadter. Mev-energy x rays from inverse compton scattering with laser-wakefield accelerated electrons. *Physical review letters*, 110(15):155003, 2013.

[46] FS Tsung, C Ren, LO Silva, WB Mori, and T Katsouleas. Generation of ultra-intense single-cycle laser pulses by using photon deceleration. *Proceedings of the National Academy of Sciences of the United States of America*, 99(1):29–32, 2002.

[47] E Esarey, A Ting, and P Sprangle. Frequency shifts induced in laser pulses by plasma waves. *Physical Review A*, 42(6):3526, 1990.

[48] D Umstadter. Relativistic laser–plasma interactions. *Journal of Physics D: Applied Physics*, 36(8):R151, 2003.

[49] W Kruer. *The physics of laser plasma interactions*. CRC Press, 1986.

[50] E Esarey, P Sprangle, J Krall, and A Ting. Self-focusing and guiding of short laser pulses in ionizing gases and plasmas. *IEEE Journal of Quantum Electronics*, 33(11):1879–1914, 1997.

[51] SC Wilks, JM Dawson, WB Mori, T Katsouleas, and ME Jones. Photon accelerator. *Physical Review Letters*, 62(22):2600, 1989.

[52] CD Murphy, RMGM Trines, J Vieira, AJW Reitsma, R Bingham, JL Collier, EJ Divall, PS Foster, CJ Hooker, AJ Langley, PA Norreys, RA Fonseca, F Fiuza, LO Silva, JT Mendoca, WB Mori, JG Gallacher, R Viskup, DA Jaroszynski, SPD Mangles, Krushelnick K Thomas, AGR, and Z Najmudin. Evidence of photon acceleration by laser wake fields. *Physics of Plasmas*, 13(3):033108, 2006.

[53] RL Savage Jr, C Joshi, and WB Mori. Frequency upconversion of electromagnetic radiation upon transmission into an ionization front. *Physical Review Letters*, 68(7):946, 1992.

[54] WM Wood, CW Siders, and MC Downer. Measurement of femtosecond ionization dynamics of atmospheric density gases by spectral blueshifting. *Physical Review Letters*, 67(25):3523, 1991.

[55] JM Dias, L Oliveira e Silva, and JT Mendonça. Photon acceleration versus frequency-domain interferometry for laser wakefield diagnostics. *Physical Review Special Topics-Accelerators and Beams*, 1(3):031301, 1998.

[56] NE Andreev and SY Kalmykov. Backward stimulated raman scattering of a modulated laser pulse in plasmas. *Physics Letters A*, 227:110–116, 1997.

[57] CB Darrow, C Coverdale, MD Perry, WB Mori, C Layton, K Marsh, and C Joshi. Strongly coupled stimualted raman backscatter from subpicosecond laser-plasma interactions. *Physical Review Letters*, 69(3), 1992.

[58] B.R. Walton, S.P.D. Mangles, Z. Najmudin, M. Tatarakis, M.S. Wei, A. Gopal, C. Marle, A.E. Dangor, K. Krushelnick, S. Fritzler, V. Malka, R.J. Clarke, and C. Hernandez-Gomez. Measurements of forward scattered laser radiation from intense sub-ps laser interactions with underdense plasmas. *Physics of Plasmas*, 13(113103), 2006.

[59] M.M. Škorić, L. Nikolić, and S. Ishiguro. Self-organiation and control in stimulated raman backscattering. *Journal of Plasma Physics*, 79(6):1003–1006, 2013.

[60] G Berden, Steven P Jamison, Allan M MacLeod, W Allan Gillespie, B Redlich, and AFG Van der Meer. Electro-optic technique with improved time resolution for real-time, nondestructive, single-shot measurements of femtosecond electron bunch profiles. *Physical Review Letters*, 93(11):114802, 2004.

[61] J Van Tilborg, CB Schroeder, CV Filip, Cs Tóth, CGR Geddes, G Fubiani, Rupert Huber, RA Kaindl, E Esarey, and WP Leemans. Temporal characterization of femtosecond laser-plasma-accelerated electron bunches using terahertz radiation. *Physical Review Letters*, 96(1):014801, 2006.

[62] O Lundh, J Lim, C Rechatin, L Ammoura, A Ben-Ismaïl, X Davoine, G Gallot, J-P Goddet, E Lefebvre, V Malka, and J Faure. Few femtosecond, few kiloampere electron bunch produced by a laser–plasma accelerator. *Nature Physics*, 7(3):219, 2011.

[63] S Corde, K Ta Phuoc, G Lambert, R Fitour, V Malka, A Rousse, A Beck, and E Lefebvre. Femtosecond x rays from laser-plasma accelerators. *Reviews of Modern Physics*, 85(1):1, 2013.

[64] CB Schroeder, Eric Esarey, BA Shadwick, and WP Leemans. Trapping, dark current, and wave breaking in nonlinear plasma waves. *Physics of Plasmas*, 13(3):033103, 2006.

[65] S Yu Kalmykov, Leonid M Gorbunov, Patrick Mora, and Gennady Shvets. Injection, trapping, and acceleration of electrons in a three-dimensional nonlinear laser wakefield. *Physics of plasmas*, 13(11):113102, 2006.

[66] JL Shaw, Nuno Lemos, Ligia Diana Amorim, Navid Vafaei-Najafabadi, KA Marsh, FS Tsung, WB Mori, and C Joshi. Role of direct laser acceleration of electrons in a laser wakefield accelerator with ionization injection. *Physical review letters*, 118(6):064801, 2017.

[67] APL Robinson, AV Arefiev, and D Neely. Generating superponderomotive electrons due to a non-wake-field interaction between a laser pulse and a longitudinal electric field. *Physical review letters*, 111(6):065002, 2013.

[68] AV Arefiev, APL Robinson, and VN Khudik. Novel aspects of direct laser acceleration of relativistic electrons. *Journal of Plasma Physics*, 81(4), 2015.

[69] L Willingale, PM Nilson, AGR Thomas, SS Bulanov, A Maksimchuk, W Nazarov, TC Sangster, C Stoeckl, and K Krushelnick. High-power, kilojoule laser interactions with near-critical density plasma. *Physics of Plasmas*, 18(5):056706, 2011.

[70] AV Arefiev, BN Breizman, M Schollmeier, and VN Khudik. Parametric amplification of laser-driven electron acceleration in underdense plasma. *Physical review letters*, 108(14):145004, 2012.

[71] AV Arefiev, VN Khudik, and M Schollmeier. Enhancement of laser-driven electron acceleration in an ion channel. *Physics of Plasmas*, 21(3):033104, 2014.

[72] VN Khudik, X Zhang, T Wang, and G Shvets. Far-field constant-gradient laser accelerator of electrons in an ion channel. *Physics of Plasmas*, 25(8):083101, 2018.

[73] AV Arefiev, VN Khudik, APL Robinson, G Shvets, L Willingale, and M Schollmeier. Beyond the ponderomotive limit: Direct laser acceleration of relativistic electrons in sub-critical plasmas. *Physics of Plasmas*, 23(5):056704, 2016.

[74] APL Robinson, AV Arefiev, and VN Khudik. The effect of superluminal phase velocity on electron acceleration in a powerful electromagnetic wave. *Physics of Plasmas*, 22(8):083114, 2015.

[75] J Meyer-ter Vehn and Zh M Sheng. On electron acceleration by intense laser pulses in the presence of a stochastic field. *Physics of Plasmas*, 6(3):641–644, 1999.

[76] JD Jackson. *Classical electrodynamics*. AAPT, 1999.

[77] E Esarey, BA Shadwick, P Catravas, and WP Leemans. Synchrotron radiation from electron beams in plasma-focusing channels. *Physical Review E*, 65(5):056505, 2002.

[78] M Vargas, W Schumaker, ZH He, Z Zhao, K Behm, V Chvykov, B Hou, K Krushelnick, A Maksimchuk, V Yanovsky, and AGR Thomas. Improvements to laser wakefield accelerated electron beam stability, divergence, and energy spread using three-dimensional printed two-stage gas cell targets. *Applied Physics Letters*, 104(17), 2014.

[79] J Osterhoff, A Popp, Z Major, B Marx, TP Rowlands-Rees, M Fuchs, M Geissler, R Hörlein, B Hidding, S Becker, EA Peralta, U Schramm, F Gruner, D Habs, F Krausz, SM Hooker, and S Karsch. Generation of stable, low-divergence electron beams by laser-wakefield acceleration in a steady-state-flow gas cell. *Physical Review Letters*, 101(8):085002, 2008.

[80] DJ Spence and Simon Mark Hooker. Investigation of a hydrogen plasma waveguide. *Physical Review E*, 63(1):015401, 2000.

[81] SM Saltiel, SD Savov, and IV Tomov. A simple technique for real time pulsewidth measurements of single ultrashort laser pulses. *Optical and Quantum Electronics*, 14(5):391–394, 1982.

[82] T Matsuoka, C McGuffey, PG Cummings, Y Horovitz, F Dollar, V Chvykov, G Kalintchenko, P Rousseau, V Yanovsky, SS Bulanov, AGR Thomas, A Maksimchuk, and K Krushelnick. Stimulated raman side scattering in laser wakefield acceleration. *Physical Review Letters*, 105(034801):, 2010.

[83] A Buck, K Zeil, A Popp, K Schmid, A Jochmann, SD Kraft, B Hidding, T Kudyakov, CMS Sears, L Veisz, S Karsch, J Pawelke, R Sauerbrey, T Cowan, F Krausz, and U Schramm. Absolute charge calibration of scintillating screens for relativistic electron detection. *Review of Scientific Instruments*, 81(3):033301, 2010.

[84] J Wood. *Betatron Radiation from Laser Wakefield Accelerators and its Applications*. PhD thesis, Imperial College London, 2016.

[85] AV Arefiev, GE Cochran, DW Schumacher, APL Robinson, and G Chen. Criterion for correctly simulating relativistic electron motion in a high-intensity laser field. In *AIP Conference Proceedings*, volume 1777, page 050001. AIP Publishing, 2016.

[86] TD Arber, K Bennett, CS Brady, A Lawrence-Douglas, MG Ramsay, NJ Sircombe, P Gillies, RG Evans, H Schmitz, AR Bell, and CP Ridgers. Contemporary particle-in-cell approach to laser-plasma modelling. *Plasma Physics and Controlled Fusion*, 57(11):113001, 2015.

[87] RA Fonseca, LO Silva, FS Tsung, VK Decyk, W Lu, C Ren, WB Mori, S Deng, S Lee, T Katsouleas, and JC Adam. Osiris: A three-dimensional, fully relativistic particle in cell code for modeling plasma based accelerators. In *International Conference on Computational Science*, pages 342–351. Springer, 2002.

[88] RA Fonseca, SF Martins, LO Silva, JW Tonge, FS Tsung, and WB Mori. One-to-one direct modeling of experiments and astrophysical scenarios: pushing the envelope on kinetic plasma simulations. *Plasma Physics and Controlled Fusion*, 50(12):124034, 2008.

[89] KI Popov, W Rozmus, VY Bychenkov, N Naseri, CE Capjack, and AV Brantov. Ion response to relativistic electron bunches in the blowout regime of laser-plasma accelerators. *Physical Review Letters*, 105(195002), 2010.

[90] CK Birdsall. Particle-in-cell charged-particle simulations, plus monte carlo collisions with neutral atoms, pic-mcc. *IEEE Transactions on Plasma Science*, 19(2):65–85, 1991.

[91] Y Ma, J Zhao, Y Li, D Li, L Chen, J Liu, SJD Dann, Y Ma, X Yang, Z Ge, Z Sheng, and J Zhang. Ultrahigh-charge electron beams from laser-irradiated solid surface. *Proceedings of the National Academy of Sciences*, page 201800668, 2018.

[92] D Haberberger, S Ivancic, SX Hu, R Boni, M Barczys, RS Craxton, and DH Froula. Measurements of electron density profiles using an angular filter refractometer. *Physics of Plasmas*, 21(5):056304, 2014.

[93] RS Craxton and RL McCrory. Hydrodynamics of thermal self-focusing in laser plasmas. *Journal of Applied Physics*, 56(1):108–117, 1984.

[94] T Arber. Epoch: Extendable pic open collaboration, 2014.

[95] J L Shaw, F S Tsung, N Vafaei-Najafabadi, K A Marsh, N Lemos, W B Mori, and C Joshi. Role of direct laser acceleration in energy gained by electrons in a laser wakefield accelerator with ionization injection. *Plasma Physics and Controlled Fusion*, 56(8):084006, 2014.

[96] PM Nilson, SPD Mangles, L Willingale, MC Kaluza, AGR Thomas, M Tatarakis, RJ Clarke, KL Lancaster, Stefan Karsch, Jörg Schreiber, Z Najmudin, AE Dangor, and K Krushelnick. Plasma cavitation in ultraintense laser interactions with underdense helium plasmas. *New Journal of Physics*, 12(4):045014, 2010.

[97] N Naseri, D Pesme, W Rozmus, and K Popov. Channeling of relativistic laser pulses, surface waves, and electron acceleration. *Physical review letters*, 108(10):105001, 2012.

[98] N Naseri, D Pesme, and W Rozmus. Electron acceleration in cavitated laser produced ion channels. *Physics of Plasmas*, 20(10):103121, 2013.

[99] P Kordell, Zulick C, AE Hussein, AV Arefiev, T Batson, J Cobble, V Glebov, D Haberberger, C Stoeckl, PM Nilson, K Krushelnick, and Willingale L. Quasi-monoenergetic ion acceleration and neutron generation from laser-driven transverse collisionless shocks. *Physical Review Letters*, Submitted, 2019.

[100] S Kar, M Borghesi, CA Cecchetti, L Romagnani, F Ceccherini, TV Liseykina, A Macchi, R Jung, J Osterholz, O Willi, LA Gizzi, A Schiavi, M Galimberti, and R Heathcote. Dynamics of charge-displacement channeling in intense laser–plasma interactions. *New Journal of Physics*, 9(11):402, 2007.

[101] RM Hochstrasser. Two-dimensional spectroscopy at infrared and optical frequencies. *Proceedings of the National Academy of Sciences*, 104(36):14190–14196, 2007.

[102] D Jung, S Bank, M L Lee, and D Wasserman. *Next-generation mid-infrared sources*, volume 19. IOP Publishing Ltd., 2017.

[103] N Bloembergen, AH Zewail, and A Amos. Energy Redistribution in Isolated Molecules and the Question of Mode-Selective Laser Chemistry Revisited. *J. Phys. Chem*, 88:5459–5465, 1984.

[104] T Popmintchev, M-C Chen, A Bahabad, M Gerrity, P Sidorenko, O Cohen, IP Christov, MM Murnane, and HC Kapteyn. Phase matching of high harmonic generation in the soft and hard x-ray regions of the spectrum. *Proceedings of the National Academy of Sciences*, 106(26):10516–10521, 2009.

[105] D Woodbury, L Feder, V Shumakova, C Gollner, R Schwartz, B Miao, F Salehi, A Korolov, A Pugžlys, A Baltuška, and HM Milchberg. Laser wakefield acceleration with mid-ir laser pulses. *Optics letters*, 43(5):1131–1134, 2018.

[106] J Lin, Y Ma, R Schwartz, D Woodbury, JA Nees, M Mathis, AGR Thomas, K Krushelnick, and H Milchberg. Adaptive control of laser-wakefield accelerators driven by mid-ir laser pulses. *Optics Express*, 27(8):10912–10923, 2019.

[107] CH Pai, YY Chang, LC Ha, ZH Xie, MW Lin, JM Lin, YM Chen, G Tsaur, HH Chu, SH Chen, JY Lin, J Wang, and SY Chen. Generation of intense ultrashort midinfrared pulses by laser-plasma interaction in the bubble regime. *Physical Review A*, 82(6):063804, 2010.

[108] Z Nie, C-H Pai, J Hua, C Zhang, Y Wu, Y Wan, F Li, J Zhang, Z Cheng, Q Su, S Liu, Y Ma, X Ning, Y He, W Lu, H-H Chu, J Wang, WB Mori, and C Joshi. Relativistic single-cycle tunable infrared pulses generated from a tailored plasma density structure. *Nature Photonics*, 12(8):489, 2018.

[109] A Hoffman. Extending opportunities. *Nature Photonics*, 6(7):407, 2012.

[110] W Zhu, JP Palastro, and TM Antonsen. Pulsed mid-infrared radiation from spectral broadening in laser wakefield simulations. *Physics of Plasmas*, 20(7):073103, 2013.

[111] A Ting, K Krushelnick, HR Burris, C Manka, E Esarey, P Sprangle, R Hubbard, HR Burris, R Fischer, and M Baine. Backscattered supercontiuum emission from high-intensity laser-plasma interactions. *Optics Letters*, 21(15), 1996.

[112] C.A. Coverdale, C.B. Darrow, C.D. Decker, , N.M. Naumova, T. Zh. Esirkepov, A.S. Sakharov, S.V. Bulanov, W.B. Mori, and K.C. Tzeng. Properties of the spectra of relativistically strong laser pulses in an underdense plasma. *Plasma Physics Reports*, 22(8), 1996.

[113] S. Miyamoto, K. Mima, M. M. Škorić, and M.S. Jovanovic. Simulations of anomalous stimulated raman backscattering in a bound plasma. *Journal of the Physics Society of Japan*, 67(4), 1998.

[114] S.C. Wilks, W.L. Kruer, E.A. Williams, P. Amendt, and D.C. Eder. *Physics of Plasmas*, 2(274), 1995.

[115] DE Hinkel, MD Rosen, EA Williams, AB Langdon, CH Still, DA Callahan, JD Moody, PA Michel, RPJ Town, RA London, and SH Langer. *Physics of Plasmas*, 18(056312), 2011.

[116] K Krushelnick, A Ting, HR Burris, A Fisher, C Manka, and E Esarey. Second harmonic generation of stimulated raman scattered light in underdense plasmas. *Physical Review Letters*, 75(20), 1995.

[117] T.G. Jones, K. Krushelnick, A. Ting, D. Kaganovich, C.I. Moore, and A. Morozov. Temporally resolved raman backscattering diagnostic of high intensity laser channeling. *Review of Scientific Instruments*, 73(6):, 2002.

[118] V. Malka, E. De Wispelaere, and J. R. Marques. *Physics of Plasmas*, 3(1682), 1996.

[119] D. Kaganovich, B. Hafizi, J.P. Palastro, A. Ting, M.H. Helle, Y.-H. Chen, T.G. Jones, and D.F. Gordon. *Physics of Plasmas*, 23(123104), 2016.

[120] M. M. Škorić, M. S. Jovanović, and M.R. Rajković. *AIP Conference Proceedings*, 1188(15), 1996.

[121] M. Kono and M.M. Škorić. *Nonlinear Physics of Plasmas*, volume 62 of *Springer Series on Atomic, Optical, and Plasma Physics*. Springer Science and Business Media, 2010.

[122] J.P. Palastro, D. Kaganovich, D. Gordon, B. Hafizi, M. Helle, J. Penano, and A. Ting. A nonlinear plasma retroreflector for single pulse compton backscattering. *New Journal of Physics*, 17(023072), 2015.

[123] D. Kaganovich, A. C. Ting, Michael H. Helle, D. F. Gordon, B. Hafizi, and J. Palastro. Compact, all-optical generation of coherent x-rays. *United States Patent Application Publication*, (0014874 A1):, 2016.

[124] P.E. Masson-Laborde, M. Z. Mo, A. Ali, S. Fourmaux, P. Lassonde, J.C. Kieffer, W. Rozmus, D. Teychenne, and R. Fedosejevs. *Physics of Plasmas*, 21(12), 2014.

[125] W. Lu, C. Huang, M. Zhou, M. Tzoufras, F.S. Tsung, W.B. Mori, and T. Katsouleas. *Physics of Plasmas*, 13(056709), 2006.

[126] P Sprangle, E Esarey, and A Ting. Nonlinear theory of intense laser-plasma interactions. *Physical review letters*, 64(17):2011, 1990.

[127] P Sprangle, E Esarey, J Krall, and G Joyce. Propagation and guiding of intense laser pulses in plasmas. *Physical review letters*, 69(15):2200, 1992.

[128] BA Shadwick, CB Schroeder, and E Esarey. Nonlinear laser energy depletion in laser-plasma accelerators. *Physics of Plasmas*, 16(5):056704, 2009.

[129] JD Ludwig, P-E Masson-Laborde, S Hüller, W Rozmus, and SC Wilks. Enhancement and control of laser wakefields via a backward raman amplifier. *Physics of Plasmas*, 25(5):053108, 2018.

[130] Cang Zhao, Kamel Fezzaa, Ross W Cunningham, Haidan Wen, Francesco De Carlo, Lianyi Chen, Anthony D Rollett, and Tao Sun. Real-time monitoring of laser powder bed fusion process using high-speed X-ray imaging and diffraction. *Scientific Reports*, 7(1):3602, 2017.

[131] CLA Leung, S Marussi, RC Atwood, M Towrie, PJ Withers, and PD Lee. In situ X-ray imaging of defect and molten pool dynamics in laser additive manufacturing. *Nature Communications*, 9(1):1–9, 2018.

[132] K.A. Jackson and J. D. Hunt. Lamellae and rod eutectic growth. *Trans. Met. Soc. AIME*, 236:1129–1142, 1966.

[133] K.A. Jackson and J.D. Hunt. Lamellar and Rod Eutectic Growth. In *Dynamics of Curved Fronts*, volume 236, pages 363–376. 1988.

[134] P Magnin and R Trivedi. Eutectic growth: a modification of the Jackson-Hunt theory. *Acta Metallurgica*, 39:453, 1991.

[135] J. L. Kang, W. Xu, X. X. Wei, M. Ferry, and J. F. Li. Solidification behavior of Co-Sn eutectic alloy with Nb addition. *Journal of Alloys and Compounds*, 695:1498–1504, 2017.

[136] J. R. Davis. *Aluminum and aluminum alloys*. ASM international, 1993.

[137] AJ Shahani, X Xiao, and PW Voorhees. The mechanism of eutectic growth in highly anisotropic materials. *Nature Communications*, 7:1–7, 2016.

[138] M Stampanoni, A Groso, A Isenegger, G Mikuljan, Q Chen, A Betrand, S Henein, U Frommherz, P Bohler, D Meister, M Lange, and R Abela. Trends in synchrotron-based tomographic imaging: the sls experience. *Proc. of SPIE*, 6318(63180M-1), 2006.

[139] M Stampanoni, F Marone, G Mikuljan, K Jefimovs, P Trtik, J Vila-Comamala, C David, and R Abela. Hierarchical, multimodal tomographic X-ray imaging at a superbend. *Developments in X-Ray Tomography Vi*, 7078(September 2018):1–11, 2008.

[140] E Eggl, M Dierolf, K Achterhold, C Jud, B Günther, E Braig, B Gleich, and F Pfeiffer. The munich compact light source: initial performance measures. *Journal of Synchrotron Radiation*, 23(5):1137–1142, 2016.

[141] TZ Zhao, K Behm, CF Dong, X Davoine, Serge Y Kalmykov, V Petrov, V Chvykov, P Cummings, B Hou, A Maksimchuk, JA Nees, V Yanovsky, AGR Thomas, and K Krushelnick. High-flux femtosecond x-ray emission from controlled generation of annular electron beams in a laser wakefield accelerator. *Physical Review Letters*, 117(9):094801, 2016.

[142] BB Pollock, FS Tsung, F Albert, JL Shaw, CE Clayton, A Davidson, N Lemos, KA Marsh, A Pak, JE Ralph, WB Mori, and C Joshi. Formation of ultrarelativistic electron rings from a laser-wakefield accelerator. *Physical Review Letters*, 115(5):055004, 2015.

[143] Doron Shaked and Ingeborg Tastl. Sharpness measure: Towards automatic image enhancement. *Proceedings - International Conference on Image Processing, ICIP*, 1(1):937–940, 2005.

[144] P Modregger, D Lübbert, P Schäfer, and R Köhler. Spatial resolution in Bragg-magnified X-ray images as determined by Fourier analysis. *Physica Status Solidi (A) Applications and Materials Science*, 204(8):2746–2752, 2007.

[145] J Cole. *Diagnosis and Application of Laser Wakefield Accelerators*. PhD thesis, Imperial College London, 2016.

[146] G Margoritondo. *Elements of Synchrotron Light: for Biology, Chemistry, and Medical Research*. Oxford University Press, 2002.

[147] S Corde, C Thaury, K Ta Phuoc, A Lifschitz, G Lambert, J Faure, O Lundh, E Benveniste, A Ben-Ismail, L Arantchuk, A Marciniak, A Stordeur, P Brijesh, A Rousse, A Specka, and V Malka. Mapping the x-ray emission region in a laser-plasma accelerator. *Physical Review Letters*, 107(21):215004, 2011.

[148] NC Lopes, JM Cole, K Poder, DJ Chapman, JC Wood, S Alatabi, ME Rutherford, D Eakins, DR Symes, SPD Mangles, and Z Najmudin. Measurement of the lwfa betatron source length by cross-correlations over images of granular random targets. *Science and Technology Facilities Council - Central Laser Facility, Annual Report*, 2015-2016.

[149] AGR Thomas. Scalings for radiation from plasma bubbles. *Physics of Plasmas*, 17(5):056708, 2010.

[150] Y Ma, D Seipt, SJD Dann, MJV Streeter, CAJ Palmer, L Willingale, and AGR Thomas. Angular streaking of betatron x-rays in a transverse density gradient laser-wakefield accelerator. *Physics of Plasmas*, 25(11):113105, 2018.

[151] AJ Shahani, E Begum Gulsoy, JW Gibbs, JL Fife, and PW Voorhees. Integrated approach to the data processing of four-dimensional datasets from phase-contrast x-ray tomography. *Optics Express*, 22(20):24606, 2014.

[152] AJ Shahani, EB Gulsoy, VJ Roussochatzakis, JW Gibbs, JL Fife, and PW Voorhees. The dynamics of coarsening in highly anisotropic systems: Si particles in Al-Si liquids. *Acta Materialia*, 97:325–337, 2015.

[153] AJ Shahani, E Gulsoy, SO Poulsen, X Xiao, and PW Voorhees. Twin-mediated crystal growth: an enigma resolved. *Scientific Reports*, 6:28651, 2016.

[154] P Cloetens, R Barrett, J Baruchel, JP Guigay, and M Schlenker. Phase objects in synchrotron radiation hard x-ray imaging. *J. Phys. D Appl. Phys.*, 29:133146, 1996.

[155] D. Paganin, S. C. Mayo, T. E. Gureyev, P. R. Miller, and S. W. Wilkins. Simultaneous phase and amplitude extraction from a single defocused image of a homogeneous object. *J. Microsc.*, 206:3340, 2002.

[156] X Wu, H Lu, and A Yan. Phase-contrast x-ray tomography: Contrast mechanism and roles of phase retrieval. *Eur. J. Radiol.*, 68S:S8S12, 2008.

[157] AC Kak and M Slaney. *Principles of Computerized Tomographic Imaging*. IEEE, 1988.

[158] D. J. Rowenhorst and P. W. Voorhees. Measurement of interfacial evolution in three dimensions. *Ann. Rev. Mater. Res.*, 42:105124, 2012.

[159] Y Sun, A Cecen, JW Gibbs, SR Kalidindi, and PW Voorhees. Analytics on large microstructure datasets using two-point spatial correlations: Coarsening of dendritic structures. *Acta Materialia*, 132:374–388, 2017.

[160] SC Irvine, DM Paganin, S Dubsky, RA Lewis, and A Fouras. Phase retrieval for improved three-dimensional velocimetry of dynamic x-ray blood speckle. *Appl. Phys. Lett.*, 93:9194, 2008.

[161] D Paganin, TE Gureyev, KM Pavlov, RA Lewis, and M Kitchen. Phase retrieval using coherent imaging systems with linear transfer functions. *Opt. Commun.*, 234:87105, 2004.

[162] R Trivedi and W Kurz. Microstructure selection in eutectic alloy systems. *Solidification Processing of Eutectic Alloys*, pages 3–34, 1988.

[163] H Jones and W Kurz. Relation of interphase spacing and growth temperature to growth velocity in fe-c and fe-fe3c eutectic alloys. *Zeitschrift fur Metallkunde*, 72(11):792–797, 1981.

[164] DH Froula, D Turnbull, AS Davies, TJ Kessler, D Haberberger, JP Palastro, S-W Bahk, IA Begishev, R Boni, S Bucht, J Katz, and JL Shaw. Spatiotemporal control of laser intensity. *Nature Photonics*, 12(5):262, 2018.

[165] SM Hooker, R Bartolini, SPD Mangles, A Tünnermann, L Corner, J Limpert, A Seryi, and R Walczak. Multi-pulse laser wakefield acceleration: a new route to efficient, high-repetition-rate plasma accelerators and high flux radiation sources. *Journal of Physics B: Atomic, Molecular and Optical Physics*, 47(23):234003, 2014.

[166] J Cowley, C Thornton, C Arran, RJ Shalloo, L Corner, G Cheung, CD Gregory, SPD Mangles, NH Matlis, DR Symes, R Walczak, and SM Hooker. Excitation and control of plasma wakefields by multiple laser pulses. *Physical Review Letters*, 119(4):044802, 2017.

[167] D Gustas, D Guénot, A Vernier, S Dutt, F Böhle, R Lopez-Martens, A Lifschitz, and J Faure. High-charge relativistic electron bunches from a khz laser-plasma accelerator. *Physical Review Accelerators and Beams*, 21(1):013401, 2018.